

SMARTPHONE-BASED OPTICAL DETECTION OF DIAGNOSTIC BIOSENSORS ON
MICROFLUIDIC PLATFORMS

by

Soohee Cho

Copyright © Soohee Cho 2017

A Dissertation Submitted to the Faculty of the

DEPARTMENT OF AGRICULTURAL AND BIOSYSTEMS ENGINEERING

In Partial Fulfillment of the Requirements

For the Degree of

DOCTOR OF PHILOSOPHY

In the Graduate College

THE UNIVERSITY OF ARIZONA

2017

THE UNIVERSITY OF ARIZONA

GRADUATE COLLEGE

As members of the Dissertation Committee, we certify that we have read the dissertation prepared by Soohye Cho, titled *Smartphone-based Optical Detection of Diagnostic Biosensors on Microfluidic Platforms* and recommend that it be accepted as fulfilling the dissertation requirement for the Degree of Doctor of Philosophy.

Jeong-Yeol Yoon Date: (07/21/2017)

Donald Uhlmann Date: (07/21/2017)

Donald Slack Date: (07/21/2017)

Lingling An Date: (07/21/2017)

Final approval and acceptance of this dissertation is contingent upon the candidate's submission of the final copies of the dissertation to the Graduate College.

I hereby certify that I have read this dissertation prepared under my direction and recommend that it be accepted as fulfilling the dissertation requirement.

Dissertation Director: Jeong-Yeol Yoon Date: (07/21/2017)

STATEMENT BY AUTHOR

This dissertation has been submitted in partial fulfillment of the requirements for an advanced degree at the University of Arizona and is deposited in the University Library to be made available to borrowers under rules of the Library.

Brief quotations from this dissertation are allowable without special permission, provided that an accurate acknowledgement of the source is made. Requests for permission for extended quotation from or reproduction of this manuscript in whole or in part may be granted by the head of the major department or the Dean of the Graduate College when in his or her judgment the proposed use of the material is in the interests of scholarship. In all other instances, however, permission must be obtained from the author.

SIGNED: Soohee Cho

Acknowledgements

I am highly appreciative and thankful for my mentor and principle investigator, Dr. Jeong-Yeol Yoon, for his inspiration, guidance, and encouragement. He is the reason why I pursued a PhD. I also appreciate my Dissertation Committee: Dr. Donald Slack, Dr. Donald Uhlmann, and Dr. Lingling An, for their support and valuable time. I thank all of my Biosensors lab mates, past and present: Tusan Park, Pei-Shih Liang, Scott Angus, Dustin Harshman, Chris Fronczek, Tigran Nahapetian, Ari Nicolini, Cayla Baynes, Katie McCracken, Robin Sweeney, Soo Chung, Kattika Kaarj, Tiffany Ulep, and Matt Bills. Lastly, thank you to my family who have always been my support and motivation.

Table of Contents

List of Figures	9
List of Tables	11
Abstract	12
1. Introduction	13
1.1 Diagnostic Biosensors	13
1.2 Conventional Diagnostic Techniques.....	13
1.3 Smartphone-based Biosensing	14
1.4 Modalities of Optical Detection	15
1.5 Particle Immunoassay	16
1.6 Microfluidic Platforms	16
1.6.1 Droplet Microfluidics	17
1.6.2 OOC Technologies	18
1.6.3 μ PADs	20
2. Conclusions	22
3. References	26
Appendix A	29
Abstract	30
1. Introduction	31
2. Materials and Method	35
2.1. Device.....	35
2.2. Bacteria Culture.....	37
2.3. PCR Reagents.....	37
2.4. Conventional PCR Thermocycling	38
2.5. Contact Angle Analysis.....	38
2.6. Arduino Programming.....	38
2.7. Droplet Thermocycling	39
2.8. Gel Electrophoresis	40
2.9. End-Point Detection Using Smartphone-Based Fluorescence Microscope	40
2.10. Impact and Vibration Tests	41
3. Results and Discussion.....	42
3.1. Contact Angle Analysis.....	42

3.2. Surface-Heated Droplet PCR Detection of <i>E. coli</i> K12	42
3.3. End-Point Detection with Smartphone Microscope	43
3.4. Portability: Vibration and Impact Shock Tests and Coconut Oil	44
4. Conclusion	46
5. Acknowledgements	47
6. References	47
7. Figures	51
Appendix B	58
Abstract	59
1. Introduction	61
2. Materials and Method	65
2.1. Urine Samples with <i>Escherichia coli</i> and <i>Neisseria gonorrhoeae</i>	65
2.2. Fabrication of Paper Microfluidic Chips	67
2.3. Antibody Conjugation to Particles	67
2.4. Assay Procedure	68
2.5. Smartphone-Based Detection and Data Analysis	69
2.6. μ PAD Filtration of Proteins from Urine	71
2.7. μ PAD Filtration of Urobilin from Urine	72
2.8. Assays with Commercial Strips	73
2.9. Statistical Analysis	73
3. Results	73
3.1. Optimization of Particle Loading to Paper Chips	73
3.2. <i>E. coli</i> Detection	76
3.3. <i>N. gonorrhoeae</i> Detection	76
3.4. μ PAD Filtration of Proteins from Urine	77
3.5. μ PAD Filtration of Urobilin from Urine	78
3.6. Commercial Test Strips	78
4. Discussion	79
5. Acknowledgements	84
6. References	84
7. Figures and Table	87
Appendix C	96
Abstract	97
1. Introduction	98
2. Materials and Method	102
2.1 OOC Fabrication	102

2.2 Antibody Conjugation to Particles	102
2.3 Cell Culture and Seeding on OOC	103
2.4 Static Assays	104
2.5 Immunoagglutination Assay of the Outflow Solutions from the OOC.....	104
2.6 OOC Immunoagglutination Assay with and without Toxicant.....	105
2.7 Fabrication of Smartphone-based Fluorescence Microscope.....	106
2.8 Smartphone-based <i>In Situ</i> Monitoring of On-Chip Expression	107
2.9 Statistical Analysis	107
3. Results	108
3.1 Static Immunoagglutination Assays of 786-O Lysates	108
3.2 OOC Assays in the Absence of Toxicant.....	109
3.3 Chemical-Induced Cytotoxicity Assays in OOC	110
3.4 <i>In Situ</i> Monitoring with Smartphone-based Fluorescence Microscopy	110
4. Discussion	112
5. Conclusion	114
6. Acknowledgements	116
7. References	117
8. Figures.....	120
Appendix D.....	128
Abstract	129
1. Introduction.....	130
2. Materials and Method	132
3. Results and Discussion.....	134
3.1 Smartphone Camera’s Response to UV LED Irradiation	134
3.2 Mie Scatter Simulation.....	135
3.3 <i>E. coli</i> Assay.....	135
3.4 <i>E. coli</i> Assay with 10% human whole blood	136
3.5 Macroscopic and SEM images of particle immunoagglutination on paper	137
4. Conclusion	137
5. Acknowledgements	138
6. Declaration of Conflicting Interests	138
7. Funding	138
8. References	139
9. Figures.....	142
Appendix E.....	148
Abstract	149
1. Introduction.....	150

2. Materials and Method	153
2.1 Fabrication of Paper Microfluidic Chips.....	153
2.2 Conjugation of Anti-NoV to Latex Particles.....	153
2.3 Sample Preparation	154
2.4 Smartphone-based Immunoassay Procedure.....	154
2.5 Data Normalization	155
2.6 Construction of Standard Curve through Data Interpolation	156
3. Results and Discussion.....	156
4. Conclusion	158
5. Acknowledgements	159
6. Declaration of Conflicting Interests.....	159
7. Funding	159
8. References	159
9. Figures and Table.....	163
Appendix F	168
Abstract	169
1. Introduction.....	170
2. Materials and Method	172
2.1 Papers and Coatings Tested.....	172
2.2 Paper Microfluidic Chip Fabrication.....	173
2.3 Cell Culture	174
2.4 Induction of Biochemical Cues	174
2.5 Immunofluorescence Microscopy	174
3. Results and Discussion.....	175
4. Conclusion	176
5. References	178
6. Figures.....	180

List of Figures

Figure 1	17
Figure 2	19
Figure 3	21
Figure A - 1	51
Figure A - 2	52
Figure A - 3	53
Figure A - 4	54
Figure A - 5	55
Figure A - 6	56
Supplementary Video A - 1	57
Operation of video can be found at https://doi.org/10.1016/j.bios.2015.06.026 .	
Figure B - 1	88
Figure B - 2	89
Figure B - 3	90
Figure B - 4	91
Figure B - 5	92
Supplementary Material B - 1	93
Supplementary Material B - 2	93
Supplementary Material B - 3	94
Figure C - 1	120
Figure C - 2	121
Figure C - 3	121
Figure C - 4	122
Figure C - 5	123
Figure C - 6	124
Supplementary Material C - 1	125
Supplementary Material C - 2	125
Supplementary Video C - S 1	126
Supplementary Video C - S 2	127
Operation of both videos can be found at https://doi.org/10.1016/j.bios.2016.07.015 .	
Figure D - 1	142
Figure D - 2	143
Figure D - 3	144
Figure D - 4	145
Figure D - 5	146
Figure D - 6	147

Figure E - 1	164
Figure E - 2	165
Figure E - 3	166
Figure E - 4	167
Figure F - 1	180
Figure F - 2	181
Figure F - 3	182
Supplementary Figure F - 1	183

List of Tables

Table B - 1.....	88
Table E - 1.....	163

Abstract

Diagnostic biosensors are on the rise in the global market due to the increasing prevalence of diseases. Specifically, the point-of-care segment has made great strides due to the improvement of biosensors' user-friendliness, simplicity, and clinical capabilities in the comfort of one's home. Although there are conventional diagnostic techniques, they are mutually time-consuming, costly, and labor-intensive. Not to mention, they are primarily dependent on bench-top or large immovable equipment. The widespread availability of smartphones has potentiated optical biosensors towards delivery of rapid and point-of-care diagnostic biosensors. Due to the affordability and user-friendliness of smartphones, smartphone-based biosensors may become ubiquitously available. Additionally, microfluidic platforms possess small footprints and portability towards development of true point-of-care and real-time diagnostic biosensors.

In this dissertation, development of multiple diagnostic biosensors on microfluidic platforms is discussed. Diagnostic biosensors equipped with a smartphone-based optical detection show great promise of bringing clinical and bench-top laboratory capabilities for the convenience of the user, with reduced time, costs, and labor requirements. The widespread availability of point-of-care and real-time diagnostic biosensors may show promise in securing global health.

1. Introduction

1.1 Diagnostic Biosensors

Biosensors are defined as analytical devices that utilize a physical transducer to recognize a biological target, which will generate a measurable signal associated with the target concentration (Liang, Jia, Hou, & Y., 2011; Kissinger, 2005). The market for biosensors is projected to reach a valuation of \$21.6 billion dollars by 2020 (Transparency Market Research, 2014). The remarkable growth of biosensors is driven by progressive research in response to the increasing prevalence of diseases.

Diagnostic biosensors are aimed to detect disease-related biomarkers or pathogens to give insight on the cause of illness. Although there are conventional analytical techniques to test for biomarkers and pathogens, there are numerous shortcomings that render the methods inaccessible or impractical. An alternative solution is the development of cost-efficient and user-friendly diagnostic biomarkers that provide the sensitivity and specificity of clinical laboratory capabilities to the user.

1.2 Conventional Diagnostic Techniques

The conventional diagnostic techniques that are available for the detection of biomarkers and pathogens include polymerase chain reaction (PCR), immunological methods, and cell culture. All three techniques exhibit limitations that prevent real-time detection and are both time-consuming and labor-intensive in nature.

With detection of pathogens, the US Centers for Disease Control and Prevention (CDC) recommends culture as the diagnostic standard (CDC, 2012). Unfortunately, culturing takes a minimum of overnight incubation and certain growth conditions, which inhibits real-time

monitoring for potential contamination or diagnosis. Not to mention, the culture of viral pathogens requires hazardous risks that call for resourceful facilities and equipment that are often inconvenient. Moreover, PCR has become the gold standard for identification and detection of specific genomic material from various biological agents (Murphy & Bustin, 2009). PCR utilizes enzymatic amplification to specifically and sensitively detect target sequences. In reality, PCR is exclusively a bench-top technique and has several shortcomings regarding translation into field settings. The protocol itself and subsequent analysis of amplicons is time-consuming, laborious, and requires expensive equipment and reagents. Although immunological methods, including enzyme-linked immunosorbent assay (ELISA), are inferior to PCR in their sensitivity largely due to their antibody titer, they are able to provide rapid results for biomarker and pathogen detection. Thus, ELISA is useful as a preliminary screening method, but could be enhanced with improved sensitivity. In addition to ELISA, immunofluorescence microscopy and detection is a traditional and widely utilized method for biomarker detection by easily labelling with fluorescently-tagged antibodies to quantify target antigens in samples (Nimse, Sonawane, Song, & Kim, 2016). In order to perform fluorescence microscopy and analyses, these methods are not *in situ* and require substantial time, resources, and costs after the assay.

1.3 Smartphone-based Biosensing

In lieu of the traditional analyses techniques for detection of biomarkers and pathogens, biosensors serve as point-of-care diagnostic tools that bring the capabilities of the conventional methods to the user. In fact, the point-of-care testing segment of the global biosensor market accounted for the largest share due to improved quality service, reduced waiting time, and enhanced patient satisfaction (Transparency Market Research, 2014). A pivotal force that

potentiated the development of point-of-care and real-time diagnostic biosensors is the increasing availability of mobile phones. Studies showed that the fast growing mobile phone market in the developing world enabled the use of camera phones as a promising platform for delivery of rapid diagnostics (Yetisen, Akram, & Lowe, 2013). With the widespread availability of mobile phones, the associated real-time capabilities of point-of-care can be a reality. Furthermore, the ever-advancing features of smartphones enable data storage, processing, and detection. The subsequent incorporation to biosensors enhances sensor portability and simplicity. Towards this end, the use of smartphones as the primary interface for biosensors potentiates point-of-care and real-time diagnostics with ease of use, which is demonstrated in all five appendices.

1.4 Modalities of Optical Detection

Optical biosensors are typically based on measurements of luminescent, fluorescent, or colorimetric produced by the interaction between transducer and the target analyte. Specifically, appendices A and C utilize a smartphone for image acquisition to measure fluorescence intensities. Appendices B, D, and E utilize particle immunoagglutination of which subsequent Mie scatter intensities are captured by smartphone detection. In particular, appendix D investigates the use of UV LED to enhance the Mie scatter intensity and to nullify the environmental conditions that may be present in field settings to render a field-deployable optical biosensor.

1.5 Particle Immunoassay

Particle immunoagglutination assays entail detection of target antigen by using antibody-conjugated latex particles. Target-specific antibodies enable specific detection of targets and thus, the specificity of the assay. As the extent of immunoagglutination increases due to antibody-antigen interaction, subsequent Mie scatter can be measured. Mie scatter is an elastic scattering of light that is particle size dependent. As a result, the Mie scatter measurement is correlated to the presence and size of immunoagglutinated particles, which is representative of target presence and concentration. The smartphone is able to detect changes in Mie scatter intensity which are not obvious to the naked eye.

1.6 Microfluidic Platforms

Originating in the 1980s, microfluidics concerns the precise control and manipulation of fluids constrained to micrometer channels. The field of microfluidics has made great strides from focusing on basic systems concerning turbulent and laminar flow and micromechanical valves and pumps (Graesen, 1993) to lab-on-a-chip (LOC) technologies (Vanapalli, Duits, & Mugele, 2009). LOC advantages include low fluid volume and consumption (less waste, costs and sample volume for diagnostics), and faster analysis and response time due to short diffusion distance. In summary, microfluidics requires lower fabrication costs, possesses mass production capabilities, and are compact in size for portability (Ghallab & Badawy, 2004). LOC development has included the integration of advanced 3D tissue engineered constructs for organ-mimic modeling, commonly referred as organ-on-a-chip (OOC; Bhise, et al., 2014). In addition, LOC research has also included the development of microfluidic paper analytical devices (μ PADs). There are three different microfluidic formats utilized in this work: droplet, OOC, μ PADs.

1.6.1 Droplet Microfluidics

In appendix A, a droplet microfluidic-sized sample was effectively amplified in a surface-heated PCR system (fig. 1). The droplet sample was stable and maintained in an oil emulsion, with a thermocouple loop guiding its amplification while providing real-time temperature feedback simultaneously. The high surface to volume ratio of the droplet enabled convective heat transfer and ultimately shortened assay time to minutes compared to hours for conventional PCR. Again, small sample volume and miniaturized PCR system yielded a cost-efficient and portable system for pathogen detection.

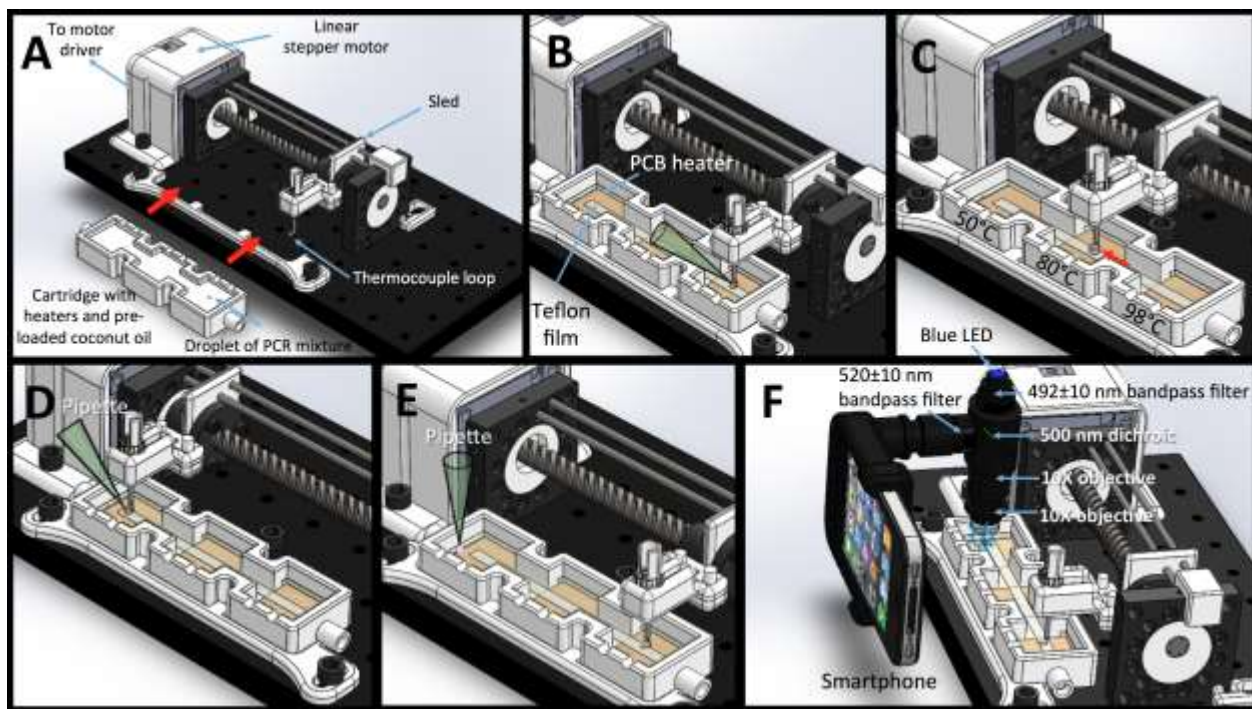


Figure 1

Schematic illustrations for the device layout and its operation. (A) All the major components of the device, less the circuit. A disposable cartridge, pre-loaded with solid coconut oil at room

temperature and a droplet of PCR mixture (within the oil), is connected to the device. (B) The oil melts upon initial heating and the thermocouple loop picks up the droplet (PCR mixture + sample target). The sample solution is added to the PCR mixture droplet using a pipette. (C) In one complete thermal cycle, the droplet moves from the denaturation chamber (98°C), to the annealing chamber (50°C), and then to the extension chamber (80°C). The droplet returns back to the denaturation chamber to commence another cycle. The droplet is guided across the chambers by a thermocouple loop, and it contacts on the Teflon-coated heater surfaces. A PCB heater and a surface-mounted thermocouple control the oil temperature in each chamber. The droplet stays in each chamber until the thermocouple loop detects that it has reached the desired temperature (95°C, 56°C, and 72°C, respectively). (D) A pipette dislodges the droplet upon completion of PCR thermocycling. (E) The thermocouple loop and the metal guide are moved to the extension chamber to secure room for a smartphone microscope. 1 μ L of 20X SYBR Green I dye solution is added to the droplet. (F) A smartphone-based fluorescence microscope measures fluorescence.

1.6.2 OOC Technologies

Organ-on-a-chip (OOC) technologies contain advanced 3D tissue engineered constructs and cultured human cells to replicate a human organ of interest (Bhise, et al., 2014). Microfluidic channel networks are designed and fabricated to mimic the organ structure (e.g., liver sinusoid, nephron in a kidney, etc.; fig. 2). The channel surfaces are usually modified with the layers mimicking the ECM, allowing the human cells to adhere, spread, and proliferate within the channels (thus requiring tissue engineering technologies). Once OOCs are constructed, fluid flow

is applied to generate mechanical forces that recapitulate the *in vivo* microenvironment experienced by cells (Bhise, et al., 2014; Inamdar & Borenstein, 2011). Specifically, organ-specific fluid flow enables gradient formations of molecular compounds and maintenance of cell-cell interactions (Inamdar & Borenstein, 2011; Huh, et al., 2010; Kim, Huh, Hamilton, & Ingber, 2012), which are vital to emulating human physiological responses. Previous research has demonstrated that incorporated ECM networks yielded *in vivo*-like behaviors such as apical-basal polarization (Schoenenberger, Zuk, Zinkl, Kendall, & Matiln, 1994), lumen formation (Debnath & Muthuswamy, 2003), increased differentiation (Weaver, et al., 1997), and appropriate protein expression (Lin & Bissell, 1993). Finally, OOCs are significantly affordable and mass-producible, with low reagent consumption and waste production and tunable properties when compared to the conventional 2D assays (Nieskens & Wilmer, 2016).

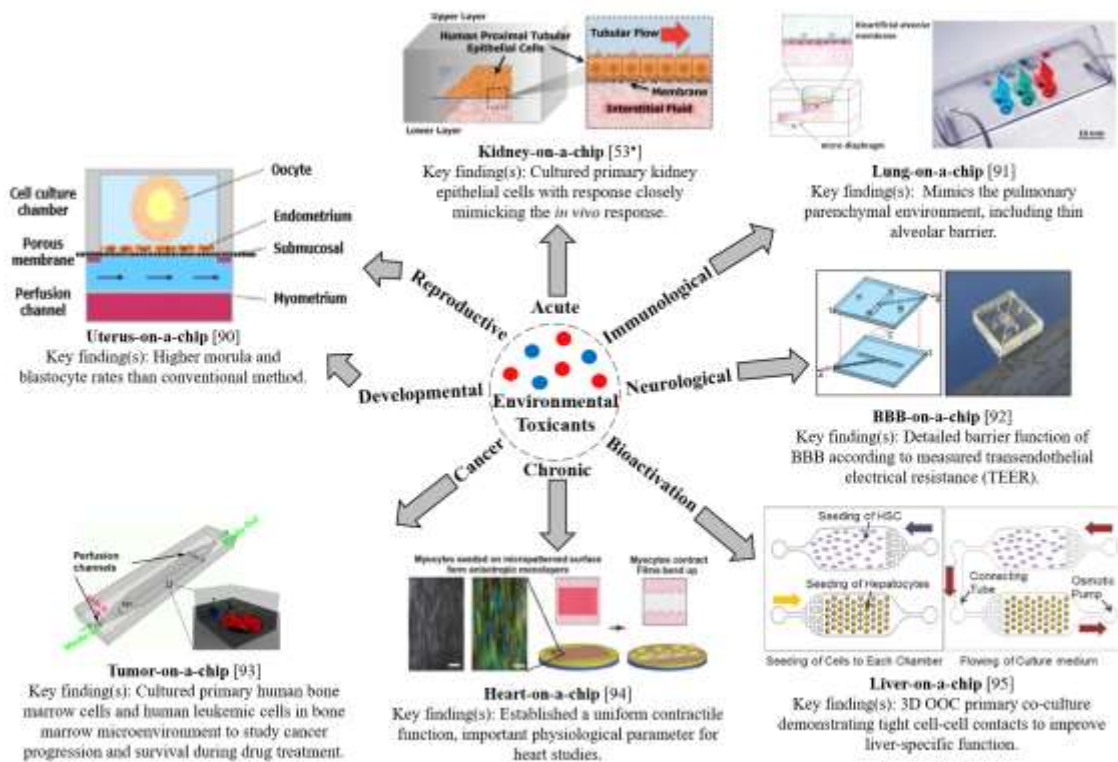


Figure 2

Summary of existing OOC technologies. Figure reproduced with permission from Elsevier (Cho & Yoon, 2017).

1.6.3 μ PADs

μ PADs have gained momentum as an advantageous LOC platform due to numerous factors, such as portability, disposability, cost-effectiveness, and operability without extensive technical training (Martinez, et al., 2008; Park, Li, McCracken, & Yoon, 2013). As a result, μ PADs have become attractive for diagnostic purposes in remote locations and the developing world (Sechi, Greer, Johnson, & Hashemi, 2013). By coupling μ PADs with particle immunoassay, subsequent extent of immunoagglutination can be detected by a smartphone (figure 3). In addition, μ PADs are perfect candidates for detection from complex matrices due to the fibers' filtration capabilities. Our group has previously demonstrated that the innate filtration of paper fibers decreased the presence of water contaminants (Park & Yoon, 2015). Not to mention, paper microfluidics has become a popular sensor platform due to its simplified patterning protocol via use of wax printers (figure 3a). By use of computer-aided design (CAD), multiple patterns can be prototyped and wax printed within a matter of minutes. As a result, the hydrophobic wax defines the channels of the μ PAD. Future research and development of paper-based microfluidic systems have included cell culture to investigate its potential as a platform for cell-based assays.

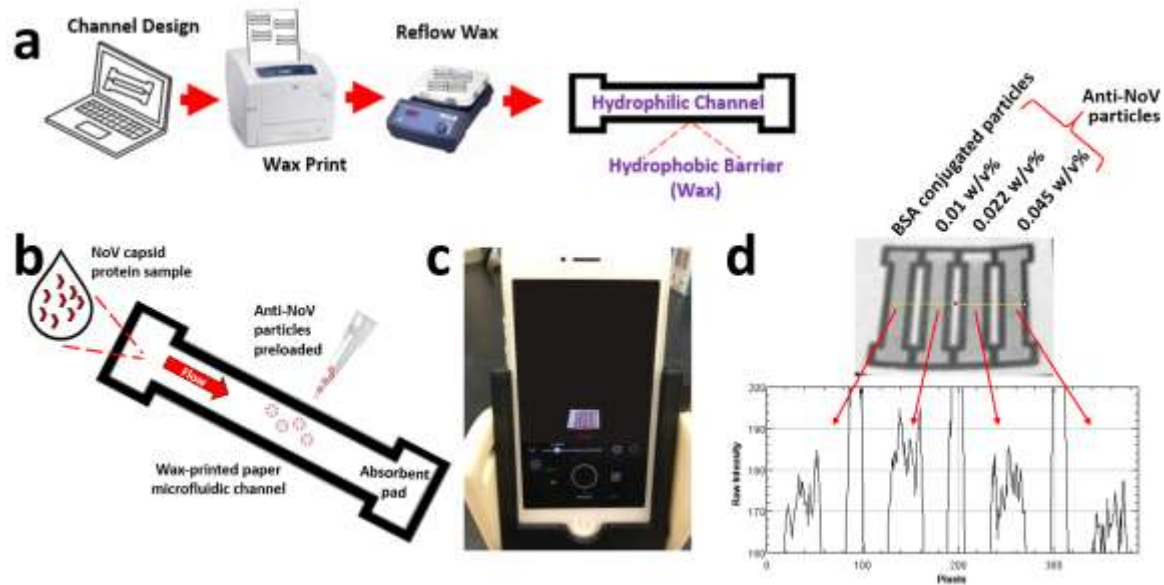


Figure 3

Assay procedure. **a)** Microchannel layouts were designed in SolidWorks and printed to chromatographic paper using a wax printer. The printed chips were placed on a hot plate to melt the wax, filling the entire depth of paper, creating hydrophobic wax barriers around the microfluidic channel. **b)** Anti-NoV conjugated particles were preloaded and dried at the center of microfluidic channel. Sample solution containing NoV capsid proteins was loaded to the inlet of the microfluidic channel.

2. Conclusions

Appendices A-F illustrate six diagnostic biosensors on microfluidic platforms developed with the incorporation of smartphone-based optical detection.

Appendix A includes the development of a surface-heated, droplet PCR system that is portable, resistant to multiple stresses, and utilizes droplet microfluidics. The device offers a rapid detection due to the fast PCR time compared to conventional PCR that takes hours largely due to its miniaturization and droplet sample volume. End-point fluorescence quantification of *Escherichia coli* (*E. coli*) genomic DNA was conducted with a smartphone-based fluorescence microscope. The use of coconut oil provided additional portability and ease of transportation by maintaining a solid profile at room temperature until heated, which supported field-deployment purposes. Assay time consisted of 15 minutes for a 30-cycle amplification with a detection limit of 10^3 genome copies per sample.

Appendix B illustrates the design and use of μ PADs for evaluating urinary tract infection (UTI) and sexually transmitted disease (STD) by using particle immunoagglutination assay. Pathogens *E. coli* (responsible for UTI) and *Neisseria gonorrhoeae* (*N. gonorrhoeae*), the cause of the STD gonorrhea, were detected from human urine without pretreatment or purification steps. Our μ PADs filtered urobilin from urine, the responsible yellow pigment of urine, which was discovered to exhibit green fluorescence emission to ultimately minimize false-positive signals from immunoagglutinated particles. By optimizing the antibody-conjugated particle concentration used, a linear range of assay up to 10^7 CFU/mL was accomplished. Total μ PAD assay time was less than 30 s with detection limit of 10 colony forming unit (CFU)/mL for both

E. coli and *N. gonorrhoeae*, while a commercially available gonorrhea rapid kit and nitrite assay test strip (indirect test for *E. coli*) had a detection limit of 10^6 CFU/mL. This μ PAD system and smartphone-based detection may serve as a low-cost, point-of-care, sensitive urinalysis biosensor to monitor UTI and gonorrhea from human urine.

Appendix C demonstrates the use of a hand-held, smartphone-based fluorescence microscope that enables dual-mode, *in situ* monitoring of an OOC, specifically a kidney-on-a-chip. This addresses the issue of traditional immunofluorescence microscopy techniques that require invasive collection of samples within the OOC. A fluorescent particle immunoassay for γ -glutamyl transpeptidase (GGT), a biomarker on the apical brush border membrane of kidney cells, was incorporated into the kidney-on-a-chip. In response to a toxicant, the brush border membrane frequently sheds, thus releasing GGT into the tubular lumen, and often serves as a target for cytotoxicity detection. A simple kidney-on-a-chip was fabricated using 3D printing of master molds and a common house-use cutter machine. The cutter machine was used to modify the surface topography of glass for improving cell adherence; whereas, 3D printed templates for conventional soft lithography was used to yield polydimethyl siloxane (PDMS)-based OOC. GGT-specific antibody-conjugated fluorescent particles bound to GGT was quantified both internally (via immunoagglutination onto biomarkers on cell membranes) and externally (immunocaptured of increased biomarker presence in outflow of the chip) in response to a known toxicant. This such non-invasive monitoring tool proved to be easy to use, affordable, and applicable to any existing OOCs to facilitate their subsequent analyses.

Appendix D involves the investigation of the smartphone camera, specifically the complementary metal oxide semiconductor or CMOS array, response to UV LED (UVA). Particle immunoassay for *E. coli* detection on μ PADs was demonstrated while using UVA as a light source to enhance the optical signal intensities. This work was in consideration of truly assimilating smartphone-based biosensors to field deployable and point-of-care applications that require reduction of independent environmental factors. With the use of UVA, the Mie scatter intensity increased up to 50% for the *E. coli* sample detection, with a detection limit of 10 CFU/mL, in reference to the negative signal in both water and human whole blood.

Appendix E concerns the development of a multi-normalization and interpolation protocol to improve immunoassays utilizing antibodies with weak antibody titer. Such is the case when detecting norovirus (NoV), one of the leading causes of acute gastroenteritis. A rapid and field-deployable diagnostic biosensor is desired for screening water for potential NoV contamination. Typically enzyme immunoassays can be used for such detection, but the low antibody titer renders the inferior sensitivity. In this work, smartphone-based Mie scatter detection of NoV was performed with immunoagglutinated particles on μ PADs. To combat the poor antibody titer, multiple normalization steps and interpolation procedure were developed to estimate the optimum amount of antibody-conjugated particles required for specific NoV concentration detection. Using only three different concentrations of anti-NoV conjugated particles, a singlet standard curve covering seven orders of magnitude of NoV concentration was accomplished.

Appendix F concerns a preliminary study on the validity of paper-based microfluidic models for use of investigating angiogenesis. Collagen-coated nitrocellulose is used to induce angiogenic sprouting with biochemical induction utilizing vascular endothelial growth factor (VEGF) and sphingosine-1-phosphate (S1P). Furthermore, the influence of varying flow stress is investigated.

3. References

- Bhise, N., Ribas, J., Manoharan, V., Zhang, Y., Polini, A., Massa, S., . . . Khademhosseini, A. (2014). Organ-on-a-chip platforms for studying drug delivery systems. *J. Control Release*, 190, 82-93.
- Cho, S. Y.-Y. (2017). Organ-on-a-chip for assessing environmental toxicants. *Curr Opin Biotechnol*, 45, 34-42.
- Debnath, J., & Muthuswamy, S. B. (2003). Morphogenesis and oncogenesis of MCF-10A mammary epithelial acini grown in three-dimensional basement membrane cultures. *Methods*, 30, 256-268.
- Ghallab, Y., & Badawy, W. (2004). Sensing methods for dielectrophoresis phenomenon: from bulky instruments to lab-on-a-chip. *IEEE Circuits and Systems Magazine*, 4(3), 5-15.
- Graesen, P. (1993). Microfluidics-a review. *J. Micromech. Microeng.*, 3, 168-182.
- Gruhl, F., Rapp, B., & Lange, K. (2013). Biosensors for Diagnostic Applications. In *Adv Biochem Eng Biotechnol* (pp. 115-148). Springer-Verlag Berlin Heidelberg.
- Huh, D., Matthews, B., Mammoto, A., M., M.-Z., Hsin, H., & Ingber, D. (2010). Reconstituting organ-level lung functions on a chip. *Science*, 328, 1662-1668.
- Inamdar, N., & Borenstein, J. (2011). Microfluidic cell culture models for tissue engineering. *Curr Opin Biotechnol*, 22, 681-689.
- Kim, H., Huh, D., Hamilton, G., & Ingber, D. (2012). Human gut-on-a-chip inhabited by microbial flora that experiences intestinal peristalsis-like motions and flow. *Lab Chip*, 12, 2165-2174.
- Kissinger, P. (2005). Biosensors - a perspective. *Biosensors and Bioelectronics*, 20, 2512-2516.

- Liang, S., Jia, W., Hou, C., & Y., L. (2011). Microbial biosensors: a review. *Biosensors and Bioelectronics*, 26, 1788-1799.
- Lin, C., & Bissell, M. (1993). Multi-faceted regulation of cell differentiation by extracellular matrix. *FASEB J*, 7, 737-743.
- Martinez, A., Phillips, S., Carrilho, E., Thomas, S., Sindi, H., & Whitesides, G. (2008). Simple telemedicine for developing regions: camera phones and paper-based microfluidic devices for real-time, off-site diagnosis. *Anal Chem*, 80(10), 3699-3707.
- Murphy, J., & Bustin, S. (2009). Reliability of real-time reverse-transcription PCR in clinical diagnostics: gold standard or substandard? *Expert Review of Molecular Diagnostics*, 9(2), 187-197.
- Nieskens, T., & Wilmer, M. (2016). Kidney-on-a-chip technology for renal proximal tubule tissue reconstruction. *Eur J Pharmacol*, 790, 46-56.
- Nimse, S., Sonawane, M., Song, K.-S., & Kim, T. (2016). Biomarker detection technologies and future directions. *Analyst*, 740-755.
- Park, T., & Yoon, J.-Y. (2015). Smartphone Detection of Escherichia coli from Field Water Samples on Paper Microfluidics. *IEEE Sensors J*, 1902-1907.
- Park, T., Li, W., McCracken, K., & Yoon, J.-Y. (2013). Smartphone quantifies Salmonella from paper microfluidics. *Lab Chip*, 13, 4832-4840.
- Prevention), C. (. (2012). *Guidance for Public Health Laboratories on the Isolation and Characterization of Shiga Toxin-Producing Escherichia coli (STEC) from Clinical Specimens*. Retrieved from <http://www.cdc.gov/ecoli/clinicians.html>

- Research, T. M. (2014). *Biosensors Market - Global Industry Analysis, Size, Share, Growth, Trends and Forecast, 2014-2020*. Retrieved from <http://www.transparencymarketresearch.com/biosensors-market.html>
- Schoenenberger, C., Zuk, A., Zinkl, G., Kendall, D., & Matiln, K. (1994). Integrin expression and localization in normal MDCK cells and transformed MDCK cells lacking apical polarity. *J Cell Sci*, 107, 527-541.
- Sechi, D., Greer, B., Johnson, J., & Hashemi, N. (2013). Three-dimensional paper-based microfluidic device for assays of protein and glucose in urine. *Anal Chem*, 85(22), 10733-10737.
- Vanapalli, S., Duits, M., & Mugele, F. (2009). Microfluidics as a functional tool for cell mechanics. *Biomicrofluidics*, 3(1), 12006.
- Weaver, V., Petersen, O., Wang, F., Larabell, C., Briand, P., Damsky, C., & Bissell, M. (1997). Reversion of the malignant phenotype of human breast cells in three-dimensional culture and in vivo by integrin blocking. *Antibodies*, 137, 231-245.
- Yetisen, A., Akram, M., & Lowe, C. (2013). Paper-based microfluidic point-of-care diagnostic devices. *Lab on a Chip*, 13, 2210-2251.

Appendix A

A Portable, Shock-Proof, Surface-Heated Droplet PCR System for *Escherichia coli* Detection

Scott V. Angus^{a,†}, Soohye Cho^{a,†}, Dustin K. Harshman^b, Jae-Young Song^c, Jeong-Yeol Yoon^{a,b,*}

^aDepartment of Agricultural and Biosystems Engineering and ^bBiomedical Engineering Graduate Interdisciplinary Program, The University of Arizona, Tucson, AZ 85721, USA, and ^cViral Disease Division, Animal and Plant Quarantine Agency, Anyang-si, Gyeonggi-do 430-757, Republic of Korea

[†]These authors contributed equally to this work.

*Corresponding author at Department of Agricultural and Biosystems Engineering, The University of Arizona, Tucson, AZ 85721-0038, USA. Tel.: +1-520-621-3587; Fax: +1-520-621-3963; URL: <http://biosensors.abe.arizona.edu>. E-mail address: jyoon@email.arizona.edu (J.-Y. Yoon).

Received 12 May 2015; accepted 12 June 2015; available online 29 August 2015.

Biosensors & Bioelectronics **74**, 360-368 (2015)

© 2015 Elsevier B.V. – All rights reserved.

Abstract

A novel polymerase chain reaction (PCR) device was developed that uses wire-guided droplet manipulation (WDM) to guide a droplet over three different heating chambers. After PCR amplification, end-point detection is achieved using a smartphone-based fluorescence microscope. The device was tested for identification of the 16S rRNA gene V3 hypervariable region from *Escherichia coli* genomic DNA. The lower limit of detection was 10^3 genome copies per sample. The device is portable with smartphone-based end-point detection and provides the assay results quickly (15 min for a 30-cycle amplification) and accurately. The system is also shock and vibration resistant, due to the multiple points of contact between the droplet and the thermocouple and the Teflon film on the heater surfaces. The thermocouple also provides real-time droplet temperature feedback to ensure it reaches the set temperature before moving to the next chamber/step in PCR. The device is equipped to use either silicone oil or coconut oil. Coconut oil provides additional portability and ease of transportation by eliminating spilling because its high melting temperature means it is solid at room temperature.

Keywords: 16S rRNA, contact angle, polymerase chain reaction, smartphone, coconut oil

1. Introduction

Current methods for detecting *Escherichia coli* (*E. coli*) in samples include culture kits such as Colilert® (Idexx Laboratories, 2014), mass spectrometry (Sauer and Kliem, 2010), agar plate culture, and polymerase chain reaction (PCR) (Shannon *et al.*, 2007). *E. coli* is a common foodborne and waterborne pathogen that may produce Shiga toxin (Griffin and Tauxe, 1991) and thus can be highly pathogenic. *E. coli* O157:H7 is the classic pathogenic strain of the bacterial species (Griffin and Tauxe, 1991). It was first suggested to be used as an indicator bacterium in the 1890's, and it has become one of the most commonly used indicator bacteria for fecal contamination of water supplies (Prescott and Winslow, 1931). There have been various criteria proposed to qualify a good indicator bacterium (Myers *et al.*, 2014). Currently, no organism meets all criteria perfectly. *E. coli* is the ideal indicator because it can be detected by tests that are sensitive, specific, simple, and inexpensive, and it survives long enough to be detected (Edberg *et al.*, 2000).

With many samples, the US Centers for Disease Control and Prevention (CDC) recommends culture as the best practice (CDC, 2012), which takes 18-24 h, depending on species, growth conditions, and sample quality. Contaminated food and water samples could be consumed within this 18–24 hour time period, so culture assay times are not fast enough to prevent illness. Unfortunately, the food and water safety industry is unable to monitor for potential contamination in real-time. While alternative methods, such as immunoassay-based microfluidics, have been suggested (Fronczek *et al.*, 2013; Heinze *et al.*, 2010; Han *et al.*, 2008; Kwon *et al.*, 2010; Angus *et al.*, 2012), they are not yet scalable or sufficiently specific to identify different bacterial strains or pathogenicity.

A better alternative is to use PCR, which was invented in 1983 (Bartlett and Stirling, 2003) and has become the gold standard for identification and detection of specific DNA and RNA sequences from many biological agents (Murphy and Bustin, 2009). PCR can be used to detect the presence of a pathogen and to identify different strains, mutants, and pathogenic phenotypes (Beutin *et al.*, 2002; Welsh *et al.*, 1991; Welsh and McClelland, 1990; Punia *et al.*, 2004). The need for biological amplification (growth in culture) is eliminated by PCR, which uses enzymatic amplification to enable detection more quickly. PCR is sensitive to low copy numbers because it exponentially amplifies a specific target sequence (Mullis *et al.*, 1986). The speed, sensitivity, and specificity of PCR enable urgent detection of pathogens found in food and water samples.

In theory, PCR can be used to detect a single bacterium, virus, or fungal spore. In practice however, this is not the case, because detection by gel electrophoresis requires 0.5–5 ng of DNA per band (Life Technologies, 2014) and detection by fluorescence requires 10^{11} amplicons/ μL (Zhu *et al.*, 2012). To achieve detectable levels of amplification, greater than 30 thermal cycles are required, and it is well established that non-specific product formation can sabotage PCR specificity at high cycle numbers. Additionally, DNA extraction inefficiencies and the presence of PCR inhibitors in sample matrices make single-cell level detection difficult. Single-cell level identification by PCR requires sophisticated equipment and careful sample preparation under sterile conditions, which are difficult to obtain outside of a laboratory setting.

While PCR protocols for detection of Shiga toxin genes and other *E. coli* genes are available, the real-world use of PCR has several limitations. Laboratory equipment, including a centrifuge, thermocycler, gel electrophoresis chamber and power supply, and UV gel imaging station, is required that is not necessary for simple culture based assays. Additionally, sample

preparation can take more than 60 min. Conventional, conduction-based PCR thermocycling can take 45–180 min, depending on the thermocycling efficiency and number of thermal cycles. Moreover, if the instrument is not equipped to perform quantitative PCR (qPCR), the process time is further increased by 40–120 min because of the necessity to perform agarose gel electrophoresis.

The use of a simple, rapid PCR assay would allow these limitations to be overcome. There have been numerous attempts to decrease PCR assay times. One approach is to reduce the reaction volume to the nanoliter or picoliter scale. This volume is substantially smaller than is used for conventional PCR (typically in the microliter scale), and enables faster heat transfer thus leading to faster assays (Yoon and Kim, 2012; Lee *et al.*, 2006; Cheong *et al.*, 2008). Direct laser irradiation of nanoliter droplets of PCR solution has been used to further increase heating rates (Kim *et al.*, 2009). Numerous commercial nanoliter or picoliter PCR instruments have been developed and are currently being marketed (Baker, 2012). The major disadvantage of using this approach for pathogen detection is that the small sample volume leads to a poor limit of detection. For example, if the limit of detection of an *E. coli* PCR assay were 10 CFU/mL, one would need at least 10^8 CFU/mL to have at least 1 CFU of *E. coli* per 0.1 nL volume. At this concentration, amplification may not be necessary, and a simple lateral flow assay may be used. Therefore, various capture and concentration methods have been added to increase the target concentration prior to amplification (Lee *et al.*, 2006; Cheong *et al.*, 2008), which introduces more complication. Additional problems may arise in gene sequencing due to smaller volume and low product yield.

Another approach is the use of microliter-sized droplets in oil immersion, where the droplets are moved within a microfluidic channel (Li *et al.*, 2011; Delibato *et al.*, 2009), or on a

flat, patterned substrate (Chang *et al.*, 2006; Ohashi *et al.*, 2007; You and Yoon, 2012) over three different temperature regions (for denaturation, annealing, and extension). (In conventional PCR systems, there is a heating block with tubes containing the sample, where conductive heating and cooling are repeated for multiple cycles.) For droplets on a patterned substrate, various droplet actuation methods have been demonstrated, including electrowetting-on-dielectric (EWOD) (Cho *et al.*, 2003), surface acoustic wave (SAW) (Rocha-Gaso *et al.*, 2009), and magnetofluidics (Egatz-Gómez *et al.*, 2006), to move a droplet from one temperature area to the other. In this manner, the time required for heating and cooling can be significantly reduced (Yoon and Kim, 2012). However, in both formats, heat transfer to the droplet is difficult to control because the temperature regions in a small device are in close proximity and heat is dissipated between the components. Since the droplets are continuously moving across different regions, temperature feedback from the droplet itself becomes critical, and most of the above attempts have not demonstrated such feedback.

For both nano- or picoliter PCR and microliter droplet PCR, real-time detection is essential in order to achieve rapid detection by PCR (gel electrophoresis requires additional 40–120 min). Real-time detection is commonly accomplished by measuring fluorescence from an intercalating dye such as SYBR Green I. Several techniques have also been developed to determine fragment size by electrophoretic separation of the fluorescently stained products (Easley *et al.*, 2006; Huang *et al.*, 2006).

In this paper, we present a rapid, easy-to-use, portable PCR device, capable of detecting the 16S rRNA gene found in bacteria. Our device uses wire-guided droplet manipulation (WDM) to move droplets between three different heating surfaces with oil immersion. PCR by WDM has been shown to provide enhanced convective heat transfer for decreased assay times and detection

from complicated sample matrices (You and Yoon, 2012; Harshman *et al.*, 2014). In our approach, we use 10 μL droplets, eliminating the need for highly concentrated samples or additional concentration steps.

In this work, we present the following improvements to PCR by WDM: 1) linear configuration of heating chambers for an even smaller device, 2) physical contact of the droplet to the heater surface to ensure shock and vibration resistance, while minimizing the surface contact area by increasing the contact angle, 3) use of a thermocouple as a wire-guide to collect droplet temperature feedback and to guarantee correct thermocycling temperatures, 4) use of a smartphone-based fluorescence microscope to perform end-point detection, and 5) use of coconut oil as the surrounding medium to provide additional portability.

2. Materials and Method

2.1. Device

The device chamber and sled were designed using SolidWorks software (Dassault Systèmes, SolidWorks Corporation, Waltham, MA, USA) and fabricated using a Dimension uPrint Rapid Prototyping Device (Stratasys, Inc., Eden Prairie, MN, USA) with acrylonitrile butadiene styrene (ABS) material. This is illustrated in **Error! Reference source not found.** This linear layout made the device smaller ($1.3 \text{ L} = 20.3 \text{ cm} \times 10.2 \text{ cm} \times 6.4 \text{ cm}$) than our previous design ($13.3 \text{ L} = 22.6 \text{ cm} \times 15.2 \text{ cm} \times 38.7 \text{ cm}$; Harshman *et al.*, 2014). It also simplified the motor control and positioning by using a sled (Fig. 1A) without the need for correcting its position during thermocycling. The position of the droplet was controlled by a custom ordered linear actuator (part number: 21F4U-2.5; Haydon Kerk Motion Solutions, Inc., Waterbury, CT, USA). The linear actuator was driven by an EasyDriver motor driver (Sparkfun

Electronics, Boulder, CO, USA), which was controlled by an Arduino Uno microcontroller. This Arduino Uno microcontroller also received feedback from a type-K thermocouple (Sparkfun Electronics), predominately composed of nickel that has been proven to be corrosion-resistant. The temperature sensitive junction of the thermocouple was physically immersed in the droplet. All programming was done in the Arduino software provided at Arduino.cc. Heater pads were designed using PCB Artist (Advanced Circuits, Aurora, CO, USA) and were ordered from Advanced Circuits. Surface-mounted type-K thermocouples (part number: SA1-K, Omega Engineering, Inc., Stamford, CT, USA) were additionally used to monitor the temperatures on the heater surfaces and provide feedback for a proportional-integral-derivative (PID) controller programmed into a secondary Arduino Uno microcontroller. Measurements from the surface-mounted and droplet immersed thermocouples were output to separate liquid crystal display screens (Sparkfun Electronics). Silicone oil was the primary immersive liquid (catalog number: 181838-1L; Sigma-Aldrich Co., St. Louis, MO, USA), but coconut oil (Spectrum Organic Products, Hain Celestial Group, Inc., Melville, NY, USA) was also used. The droplet was separated from the heaters using a hydrophobic Teflon film with a self-adhesive backing (product number: 2208T61; McMaster-Carr, Elmhurst, IL, USA) (Fig. 1B). All electronics, except the heaters, were powered by the Arduino's 5 V or 3.3 V outputs. Heaters were each powered by a 3.3 V power supply with 2 A maximum current (item number 9902 PS; Marlin P. Jones & Associates, Inc., Lake Park, FL, USA). The two Arduinos, one for heater surface temperature control and the other for motor control and droplet temperature measurements, were powered by a similar power supply at 9 V and shared a common ground.

2.2. Bacteria Culture

E. coli K12 was purchased from Sigma-Aldrich (catalog number: EC1-5G; Sigma-Aldrich). It was cultured overnight in Lysogeny broth (LB; catalog no: L2542-500ML; Sigma-Aldrich). Culture was counted using LB agar (BioExpress, Kaysvilo, UT, USA) grown overnight at 37°C.

2.3. PCR Reagents

PCR reaction mixtures consisted of the following in a 5:1:1:1:2 ratio: Promega GoTaq® Green Master Mix (catalog number: M7122; Promega Corporation, Madison, WI, USA); 10 µM forward and reverse primers with sequences AAACTCAAAGKAATTGACGG and TTACTCACCCGTICGCCRCT, respectively; *E. coli* K12 genomic DNA; and nuclease free water. These primers are designed to amplify the V3 hypervariable region of 16S rRNA gene, with the expected product at 196 bp. Genomic DNA was extracted using a QIAamp® DNA Micro Kit (catalog number 56304; Qiagen, Venlo, Limburg, Netherlands) as per the manufacturer's instructions. Genomic DNA was quantified using a Qubit 2.0 Fluorometer (catalog number: Q32871; Life Technologies) as per the manufacturer's instructions. A total of 10 µL was used for each assay, while the sample volume was 1 µL. A starting *E. coli* genomic DNA content was varied from 2.6 ng/sample (equivalent to 5.2×10^5 genomic copies/sample) down to 5.2 pg/sample (equivalent to 10^3 genomic copies/sample).

2.4. Conventional PCR Thermocycling

Initial experiments were carried out in an MJ Research PTC-150 Minicycler (MJ Research, Inc.; Waltham, MA, USA). Thermocycling conditions for PCR were as follows: denaturation for 30 s at 95°C, annealing for 30 s at 56°C, and extension for 40 s at 72°C.

2.5. Contact Angle Analysis

The contact angle analysis was performed using FTÅ200 contact angle/surface tension analyzer (First Ten Ångstroms, Inc., Portsmouth, VA, USA). A water droplet of 10 µL volume was placed on the Teflon film in either silicone or coconut oil immersion, and snapshots were taken. These were then analyzed using the FTÅ32 software.

2.6. Arduino Programming

The Arduino code was written using the free Arduino version 1.0.5 software (Arduino.cc) and the PID program was modified from the code as developed by Harshman *et al.* (2014). Fig. 2 schematically illustrates how the Arduino microcontrollers are connected and control the heaters and the motor through thermocouple feedback. Briefly, there was one surface-mounted thermocouple for each heating chamber (for annealing, extension, and denaturation, respectively). The thermocouple signal is amplified using three separate MAX31855 thermocouple amplifiers (product ID 269; Adafruit, New York City, NY, USA) and is sent to an Arduino microcontroller. The PID code used this real-time temperature feedback to adjust the on/off cycle time of the heaters in each individual chamber. This allowed for a stable temperature in each heating chamber after a short ramp time. The temperature outputs of the thermocouples,

the set temperature of each chamber, and the rate of the cycle were displayed on a serial liquid crystal display (LCD).

A separate Arduino for motor control was connected to an EasyDriver as well as an AD595-AQ op-amp (model number COM-00306; Sparkfun Electronics). The AD595-AQ was connected to a single thermocouple that ran down the center of the metal guide and acted as the top anchor and temperature feedback device for the droplet. This Arduino recorded the internal droplet temperature and used it to move the motor to the next step or to remain in the current chamber for continued heating or cooling. The thermocouple temperature sensing junction was physically positioned within the droplet to provide the most accurate measurement of the droplet temperature. This Arduino also output the droplet temperature data, the current cycle number, and step of the cycle on an LCD.

2.7. Droplet Thermocycling

The temperatures of the heating chambers were set to 98°C, 80°C, and 50°C for the denaturation, extension, and annealing chambers, respectively. The set temperatures are slightly higher than the desired extension (72°C) and denaturation (94°C) temperatures and slightly lower than the desired annealing temperature (60°C) to increase heating or cooling efficiency. The droplet initially started from the right-side (denaturation chamber), moved to the left-side (annealing chamber) through the middle (extension chamber), finally moved to the middle-side extension chamber, and returned back to the right-side (Fig. 1C). 10 µL of PCR reaction mixture, with 1 µL of *E. coli* genomic DNA, was used in each droplet experiment. The temperature of the droplet was measured approximately once every second by the immersed thermocouple. Upon reaching the desired temperature, the droplet immediately left the current chamber. For

extension, the droplet remained for approximately 5 s after reaching the desired temperature to allow sufficient time for extension by the DNA polymerase. The immersed thermocouple was bent to create a ring shape (“thermocouple loop”) around the droplet. The thermocouple loop holds the droplet steady by hydrophilic attraction and surface tension. The motion of the droplet is illustrated in Figure 3A.

2.8. Gel Electrophoresis

PCR products were analyzed by agarose gel electrophoresis using a 3% w/v agarose gel (catalog number A0169; Sigma-Aldrich) in 1x Tris-acetate-EDTA (TAE) buffer (catalog number 24710-030; Life Technologies). Gel electrophoresis was run for 40 min at 120 V with an electrophoresis power supply (catalog number FB200; Thermo Fisher Inc., Pittsburg, PA, USA). A 1 kb Plus DNA Ladder (catalog number 10787; Life Technologies) was used as a standard for fragment sizing. Gels were stained with either ethidium bromide (catalog number E1510; Sigma-Aldrich) or GelRed (Biotium, Inc., Hayward, CA, USA). Gels were imaged under UV illumination. All experiments with Promega GoTaq® Colorless Master Mix were verified using gel electrophoresis.

2.9. End-Point Detection Using Smartphone-Based Fluorescence Microscope

Once the thermocycling is finished, 1 μ L of 20X SYBR Green I (SG) dye, prepared from 10,000X SG (Molecular Probes – Life Technologies, Eugene, OR, USA), was added to the reaction droplet using a pipette, resulting in 2X SG in the final solution (Fig. 1D,E). The droplet was dislodged from the thermocouple loop using a pipette tip to ensure optimum image capture by the smartphone-based fluorescence microscope. (The thermocouple loop scattered a substantial amount of incident light, greatly overshadowing the fluorescence signal.) This

microscope attachment, designed and fabricated in our laboratory (Fronczek et al., 2014), is essentially a 3D printed attachment to a smartphone (iPhone, Apple, Inc., Cupertino, CA, USA) that uses the digital camera as a secondary objective lens and an image capture device (Fig. 1F). This attachment incorporates a 466 nm super bright blue LED (catalog number YSL-R542B5C-A11, China Young Sun LED Technologies Co., Ltd., Shenzhen, China), a 492 ± 10 nm bandpass filter for this blue LED (catalog number #65-087, Edmund Optics, Barrington, NJ, USA), a 500 nm dichroic shortpass filter (catalog number #69-178, Edmund Optics), two 10X objective lens (catalog number LA1560-A, Thor Labs, Newton, NJ, USA), and a 520 ± 10 nm bandpass filter for the smartphone camera (catalog number #65-093, Edmund Optics). The plastic attachment was designed using SolidWorks software and fabricated using a Dimension uPrint Rapid Prototyping Device with acrylonitrile butadiene styrene (ABS) material.

All images were analyzed using ImageJ (National Institute of Health, Bethesda, MD, USA) and the red, green, and blue channels were analyzed simultaneously. Pixel intensities were measured from a circular region of the image surrounding the droplet. Average green pixel intensities were collected from three different experiments. All intensities were normalized to those of a negative target control (NTC; no target with PCR mixture, amplified for 30 thermal cycles).

2.10. Impact and Vibration Tests

In order to simulate an impact for the droplet within the device, the metal base plate shown in Figure 1 was hit with a plastic mallet repeatedly. For vibrational tests, the metal base plate was lifted slightly and shaken in a consistent manner. The experiments were duplicated for the pendant droplet method, to simulate the previously reported droplet PCR device (Harshman

et al., 2014). The vibration frequency and impact energy were evaluated by analyzing video clips captured during the experiments. The impact energy was calculated from the mass of a hammer (m) and its velocity (v), using $E = mv^2/2$.

3. Results and Discussion

3.1. Contact Angle Analysis

The contact angle of a sessile water-droplet on the Teflon-coated heater surface immersed in oil was measured. The contact angle in silicone oil immersion is $154 \pm 2^\circ$ ($n = 6$) and in coconut oil immersion is $156 \pm 1^\circ$ ($n = 6$) (Fig. 3B). Both contact angles are greater than 150° and classify as superhydrophobic. The superhydrophobicity of the Teflon-coated heater surface when immersed in oil results from the similarity between the oil-water and Teflon-water contact angles (110° and 115° , respectively). The superhydrophobic surface prevents contamination between samples and maintains convective heating between the surface and the droplet.

3.2. Surface-Heated Droplet PCR Detection of *E. coli* K12

In order to demonstrate PCR amplification on our surface-heated droplet PCR system, two positive control reactions containing 2.6 ng of *E. coli* K12 genomic DNA was thermocycled for 30 cycles at a thermocycling speed of 30 s/cycle. In addition, a no template control (NTC) sample was thermocycled. Amplification of the 196 bp product, corresponding to the 16S rRNA gene V3 region, was confirmed for the positive controls by gel electrophoresis (Fig. 4A; representative images from three different set of experiments). Amplification could not be detected for the NTC sample (Fig. 4A), indicating assay specificity. The reaction droplets had a final volume of 10 μ L, with 1 μ L target DNA. The positive control experiment was conducted

with silicone oil immersion. It took 3 min to pre-heat the oil chambers to their desired temperatures from room temperature, and each sample took 15 min to thermocycle. The results of the positive control experiment provide a proof of concept that the device is functional and can be tested further.

To determine the sensitivity of our system, we conducted a dilution test (Fig. 4B). For the dilution test, we thermocycled reactions containing genomic DNA from 2.6 ng to 5.2 pg (equivalent to $5.2 \times 10^5 - 10^3$ genomic copies). Amplification was confirmed by gel electrophoresis by identifying a band in the correct location at 196 bp for all samples in the range tested. The results of the dilution test establish that the device is sufficiently sensitive to amplify the 16S rRNA gene V3 region from the equivalent of 10^3 copies of the *E. coli* genome (5.2 pg of genomic DNA; roughly corresponding to 10^3 colony forming units or CFU). This level of detection is significantly lower than our previous work, which had a detection limit of 10^5 genomic copies or 1 ng of genomic DNA (Harshman *et al.*, 2014).

3.3. End-Point Detection with Smartphone Microscope

To eliminate the need for PCR product confirmation by gel electrophoresis, we have implemented end-point identification of PCR amplification using a smartphone-based fluorescence microscope (Fig. 5B). End-point detection has been demonstrated by amplifying the V3 hypervariable region of 16S rRNA gene from 1 ng to 1 pg of *E. coli* genomic DNA. After PCR amplification, a pipette was used to dislodge the droplet from the thermocouple loop (Fig. 1D) and to add SYBR Green I (SG) dye to the reaction droplet (Fig. 1E). By dislodging the droplet, the smartphone-based fluorescence microscope can be correctly positioned (Fig. 1F) and focused and the strong scattering of incident light by the thermocouple loop is avoided. A

smartphone-based fluorescence microscope (Fig. 5B) is used to capture the green fluorescence image of the droplet while it is still immersed in oil within the device. The excitation light from the blue LED is filtered by the 492 ± 10 nm bandpass filter and is transmitted through the 500 nm dichroic mirror. The excitation light is focused on the droplet by a lens. The SG emission is reflected at a 90° angle by the dichroic mirror towards the smartphone camera. Before the green fluorescence image of the droplet reaches the camera it is filtered by a 500 ± 10 nm bandpass filter to remove scattered blue light. The use of the bandpass filters and a dichroic mirror ensure that the smartphone captures only SG fluorescence. The average green pixel intensity of the fluorescence images is subsequently analyzed using ImageJ software, and is normalized to that of a NTC droplet. The normalized intensities are plotted against the initial target concentration and show an increasing trend as the initial DNA content increases (Fig. 5A). Representative fluorescence images taken by the smartphone are shown for each concentration in Figure 5A. The bands at 196 bp on the gel electropherogram from the same experiments were also quantified, normalized, and plotted against initial DNA content (Fig. 5A). The results of the dilution test and the end-point detection test show good agreement. The increasing trend is similar whether detection is made by the smartphone-based fluorescence microscope or by gel electrophoresis. Additionally, the smartphone-based fluorescence microscope could be adapted to work with other types of smartphones.

3.4. Portability: Vibration and Impact Shock Tests and Coconut Oil

In order to evaluate the resistance to vibration and impact shock, the surface-heated droplet PCR system was vibrated at a frequency of 1 Hz and impacted with an energy of 3.59 mJ. The energy of the impact shock was calculated using $E = mv^2/2$; the mass of the hammer was

227 g and its velocity was 17.8 cm/s. The vibration frequency and impact energy were evaluated by analyzing video clips captured during the experiments, and still images taken from the video are shown in Fig. 6A. Our surface-heated droplet PCR method is compared with the pendant droplet method reported by Harshman *et al.* (2014). Still images of both methods are shown during and after vibration and during and after impact shock (during and after images are taken within 1 s of each other). The surface-heated droplet PCR method withstood both vibration and impact shock, whereas the pendant droplet was dislodged by both vibration and impact shock. When the pendant droplet was dislodged, it was unable to be recovered, causing assay failure. These tests demonstrate the increased stability of the surface-heated droplet PCR system compared with the pendant droplet PCR system. This increased stability is a result of the droplet-thermocouple and the droplet-surface contact points. The robustness of the device will potentially enable it to be used in field situations such as within a moving vehicle.

The use of coconut oil provides additional portability to the proposed system. Unlike silicone oil, coconut oil is a solid at room temperature. The coconut oil remains solid until the cartridge begins heat ramping from room temperature to the desired chamber temperatures (Fig. 6B). The oil melting process takes approximately 120 s and the heater surface temperatures stabilize in approximately 300 s. Because the coconut oil is solid at room temperature, the pre-filled cartridge is not susceptible to spilling when tilted or to cross-contamination. Additionally, a droplet of PCR mixture can be stored within the solid coconut oil to be used upon melting.

The operation and portability of the system with coconut oil are demonstrated in Figure 1 and in Supplementary Material 1. The cartridge is pre-loaded with solid coconut oil that encompasses a 9 μ L droplet of PCR mixture. Once the cartridge is attached to the system and the chambers are heated to the desired temperatures for denaturation, annealing and extension, the

coconut oil melts completely. The melted coconut oil provides the necessary oil immersion environment. After melting, a 1 μL sample of bacterial genomic DNA is added to the droplet. The resulting droplet is subsequently thermocycled by moving it over the three heated surfaces. After thermocycling is complete, the droplet can be dislodged from the thermocouple and imaged by the smartphone-based fluorescence microscope. The entire cartridge is relatively inexpensive and can be made disposable to avoid cross-contamination. Together with the vibration- and shock-proof nature described in the above, the device can be used as a rapid and field-deployable PCR assay system.

4. Conclusion

Polymerase chain reaction (PCR) by wire-guided droplet manipulation (WDM), as demonstrated in Harshman *et al.* (2014), is an excellent method to increase the heat transfer efficiency and to resolve inhibition effects of sample matrices. Taking advantage of the benefits of PCR by WDM, we have developed a surface-heated droplet PCR system that is simpler and has the following improvements: droplet stability, droplet temperature feedback, portability, and end-point detection. To increase the droplet stability, we replaced the syringe needle with a thermocouple loop, which also provides temperature feedback, and placed the droplet in contact with the Teflon-coated heater surface. The droplet stability, reduced complexity, smaller size, and use of coconut oil allow for portability and for in-field use. Due to its low power consumption, the device could be powered by lithium ion batteries, which supply 3.7 V. The heaters are currently powered by 3.3 V and 2 A (6.6 W maximum power), and all the other electronic components are powered by the Arduino's 3.3 V outputs at 150 mA (0.5 W maximum power). The maximum power consumption of the entire device is 7.1 W, and lithium-ion

batteries can provide up to 265 Wh/kg. So the minimum size of a battery pack to run the device for 19 min at a maximum power of 7.1 W is only 8.5 g.

The addition of a smartphone-based fluorescence microscope allows for end-point detection of PCR amplification. By this method, PCR results are provided faster than with gel electrophoresis and with simpler equipment. A conventional qPCR system will take at least 45 min to display results from a 30-cycle assay. In contrast, our system does not need a laboratory environment and provides a result in 19 min (3 min for pre-heating the cartridge and melting the coconut oil, 15 min for thermocycling, and 1 min for adding SYBR Green I dye to the droplet). Specifically, detection by the smartphone-based fluorescence microscope is achieved nearly immediately. The food and water safety industry is in need of tools for real-time monitoring of pathogens, and our simple, stable and portable system allows the sensitive and specific PCR assay to be conducted in the field. Our system combines rapid thermocycling and smartphone-based end-point detection to provide results quickly, to communicate the results remotely, and ultimately to prevent disease outbreaks in the food and water supply.

5. Acknowledgements

This work was supported by the research grant from the Animal and Plant Quarantine Agency, South Korea (I-1541780-2012-13- 0101). DKH acknowledges the training grant support from the Cardiovascular Biomedical Engineering Training Grant from U.S. National Institutes of Health (T32HL007955).

6. References

Angus, S.V., Kwon, H.-J., Yoon, J.-Y., 2012. *J. Environ. Monit.* 14, 3295–3304.

- Baker, M., 2012. *Nat. Meth.* 9, 541–544.
- Bartlett, J.M.S., Stirling, D., 2003. *PCR Protocols*, 2nd ed., Humana Press, New Jersey.
- CDC (United States Centers for Disease Control and Prevention), 2012. *Guidance for Public Health Laboratories on the Isolation and Characterization of Shiga Toxin-Producing *Escherichia coli* (STEC) from Clinical Specimens.* <<http://www.cdc.gov/ecoli/clinicians.html>> (accessed 17.07.2014).
- Chang, Y.-H., Lee, G.-B., Huang, F.-C., Chen, Y.-Y., Lin, J.-L., 2006. *Biomed. Microdev.* 8, 215–225.
- Cheong, K.H., Yi, D.K., Lee, J.-G., Park, J.-M., Kim, M.J., Edel, J.B., Ko, C., 2008. *Lab Chip* 8, 810–813.
- Cho, S.K., Moon, H., Kim, C.-J., 2003. *J. Microelectromech. Syst.* 12, 70–80.
- Delibato, E., Gattuso, A., Minucci, A., Auricchio, B., De Medici, D., Toti, L., Castagnola, M., Capoluongo, E., Gianfranceschi, M.V., 2009. *J. Sep. Sci.* 32, 3817–3821.
- Easley, C.J., Karlinseq, J.M., Bienvenue, J.M., Legendre, L.A., Roper, M.G., Feldman, S.H., Hughes, M.A., Hewlett, E.L., Merkel, T.J., Ferrance, J.P., Landers, J.P., 2006. *Proc. Natl. Acad. Sci. USA* 103, 19272–19277.
- Edberg, S., Rice, E., Karlin, R., Allen, M., 2000. *J. Appl. Microbiol.* 88, 106S–116S.
- Egatz-Gómez, A., Melle, S., García, A.A., Lindsay, S.A., Márquez, M., Domínguez-García, P., Rubio, M.A., Picraux, S.-T., Taraci, J.L., Clement, T., Yang, D., Hayes, M.A., Gust, D., 2006. *Appl. Phys. Lett.* 89, 034106.
- Fronczek, C.F., You, D.J., Yoon, J.-Y., 2013. *Biosens. Bioelectron.* 40, 342–349.
- Fronczek, C.F., Park, T.S., Harshman, D.K., Nicolini, A.M., Yoon, J.-Y., 2014. *RSC Adv.* 4, 11103–11110.

- Griffin, P.M., Tauxe, R.V., 1991. *Epidemiol. Rev.* 13, 60–98.
- Han, J.-H., Heinze, B.C., Yoon, J.-Y., 2008. *Biosens. Bioelectron.* 23, 1303–1306.
- Harshman, D.K., Reyes, R., Park, T.S., You, D.J., Song, J.-Y., Yoon, J.-Y., 2014. *Biosens. Bioelectron.* 53, 167–174.
- Heinze, B.C., Gamboa, J.R., Kim, K., Song, J.-Y., Yoon, J.-Y., 2010. *Anal. Bioanal. Chem.* 398, 2693–2700.
- Huang, F.-C., Liao, C.S., Lee, G.B., 2006. *Electrophoresis* 27, 3297–3305.
- Idexx Laboratories, 2014. Colilert Water Testing Product Information, 2014. <<https://www.idexx.com/water/products/colilert.html>> (accessed 17.07.2014).
- Kim, H., Dixit, S., Green, C.J., Faris, G.W., 2009. *Optics Express* 17, 283–289.
- Kwon, H.-J., Dean, Z.S., Angus, S.V., Yoon, J.-Y., 2010. *JALA: J. Assoc. Lab. Autom.* 15, 216–223.
- Lee, J.-G., Cheong, K.H., Huh, N., Kim, S., Choi, J.-W., Ko, C., 2006. *Lab Chip* 6, 886–895.
- Li, Y.Y., Zhang, C.S., Xing, D., 2011. *Anal. Biochem.* 415, 87–96.
- Life Technologies, 2014. Ethidium Bromide (EtBr) Dye for DNA and RNA Detection. <<http://www.lifetechnologies.com/us/en/home/life-science/dna-rna-purification-analysis/nucleic-acid-gel-electrophoresis/dna-stains/etbr.html>> (accessed 17.07.2014).
- Mullis, K., Faloona, F., Scharf, S., Saiki, G. H., Erlich, H., 1986. *Cold Spring Harb. Symp. Quant. Biol.* 51, 263–273.
- Murphy, J., Bustin, S.A., 2009. *Expert Rev. Mol. Diagn.* 9, 187–197.
- Myers, D., Stoeckel, D., Bushon, R., 2014. Fecal Indicator Bacteria (ver. 2.0): US Geological Survey Techniques of Water-Resources Investigations, TWRI Book 9, <<http://water.usgs.gov/owq/FieldManual/Chapter7/7.1.html>> (accessed 05.08.2014).

- Ohashi, T., Kuyama, H., Hanafusa, N., Togawa, Y., 2007. *Biomed. Microdev.* 9, 695–702.
- Prescott, S.C., Winslow, C.-E.A., 1931. *Elements of Water Bacteriology: With Special Reference to Sanitary Water Analysis*, 5th edn. Wiley, New York,.
- Rocha-Gaso, M.-I., March-Iborra, C., Montoya-Baides, A., Arnau-Vives, A., 2009. *Sensors* 9, 5740–5769.
- Sauer, S., Kliem, M., 2010. *Nat. Rev. Microbiol.* 8, 74–82.
- Shannon, K.E., Lee, D.-Y., Trevors, J.T., Beaudette, L.A., 2007. *Sci. Total Environ.* 382, 121–129.
- Welsh, J., McClelland, M., 1990. *Nucleic Acids Res.* 18, 7213–7218.
- Welsh, J., Petersen, C., McClelland, M., 1991. *Nucleic Acids Res.* 19, 303–306.
- Yoon, J.-Y., Kim, B., 2012. *Sensors* 12, 10713–10741.
- You, D.J., Yoon, J.-Y., 2012. *J. Biol. Eng.* 6, 15.
- Zhu, Z., Jenkins, G., Zhang, W., Zhang, M., Guan, Z., Yang, C. J., 2012. *Anal. Bioanal. Chem.* 403, 2127–43.

7. Figures

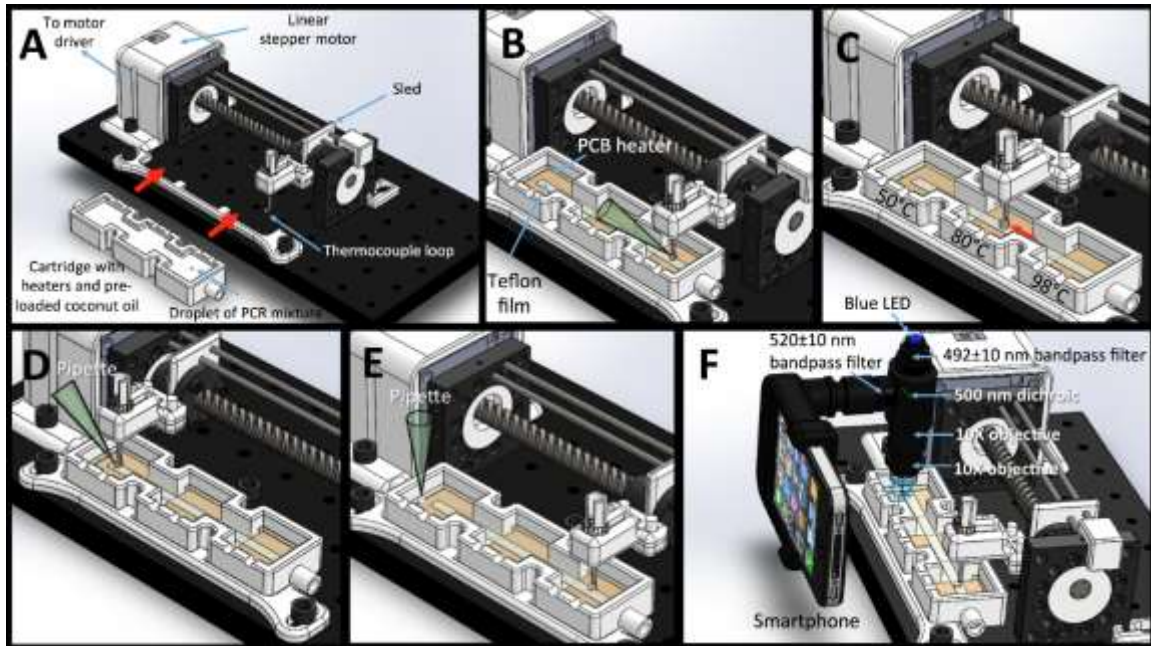


Figure A - 1

Schematic illustrations for the device layout and its operation. (A) All the major components of the device, less the circuit. A disposable cartridge, pre-loaded with solid coconut oil at room temperature and a droplet of PCR mixture (within the oil), is connected to the device. (B) The oil melts upon initial heating and the thermocouple loop picks up the droplet (PCR mixture + sample target). The sample solution is added to the PCR mixture droplet using a pipette. (C) In one complete thermal cycle, the droplet moves from the denaturation chamber (98°C), to the annealing chamber (50°C), and then to the extension chamber (80°C). The droplet returns back to the denaturation chamber to commence another cycle. The droplet is guided across the chambers by a thermocouple loop, and it contacts on the Teflon-coated heater surfaces. A PCB heater and a surface-mounted thermocouple control the oil temperature in each chamber. The droplet stays in each chamber until the thermocouple loop detects that it has reached the desired

temperature (95°C, 56°C, and 72°C, respectively). (D) A pipette dislodges the droplet upon completion of PCR thermocycling. (E) The thermocouple loop and the metal guide are moved to the extension chamber to secure room for a smartphone microscope. 1 μ L of 20X SYBR Green I dye solution is added to the droplet. (F) A smartphone-based fluorescence microscope measures fluorescence.

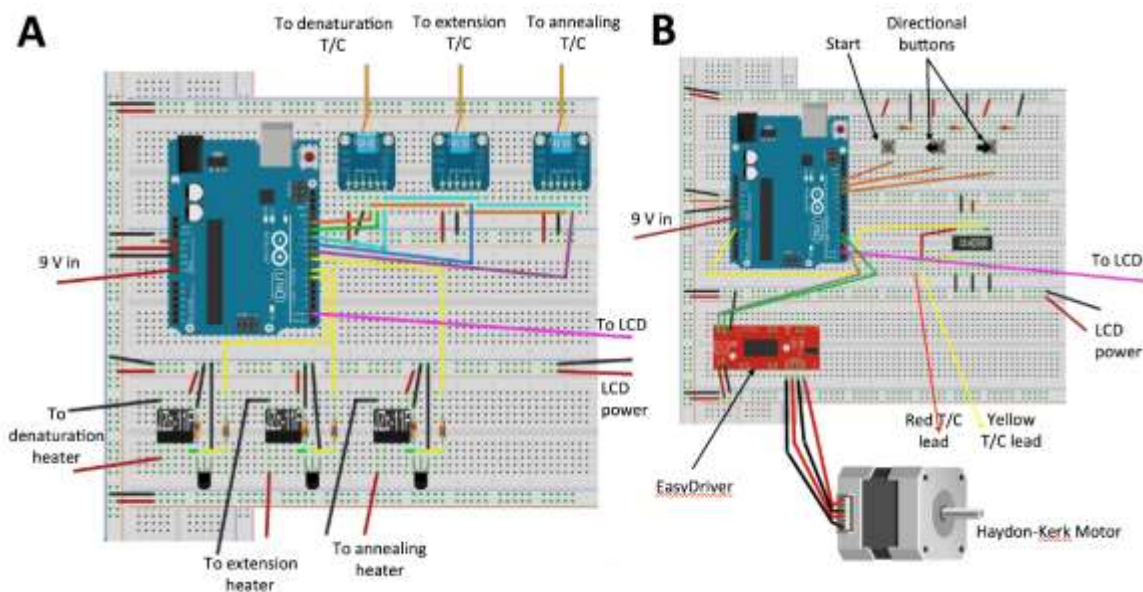


Figure A - 2

Circuit layout as seen on the breadboards. (A) There are 3 MAX31855, one for each surface-mounted thermocouple. Three JZC-11F relays, one for each heater. The temperature and PID settings are displayed on a 20×4 serial LCD (not shown). (B) The motor controller circuit, showing the AD595 used for the thermocouple loop, which measures internal droplet temperature. Also shown is the EasyDriver connected to the Arduino microcontroller and Haydon-Kerk linear stepper motor. The output of the thermocouple is displayed on another 20×4 serial LCD (not shown). There are 3 buttons, one for starting thermocycling and two for

manually positioning the thermocouple loop and droplet. Images created using Fritzing software (Friends of Fritzing e.V., Berlin, Germany). T/C =temperature control.

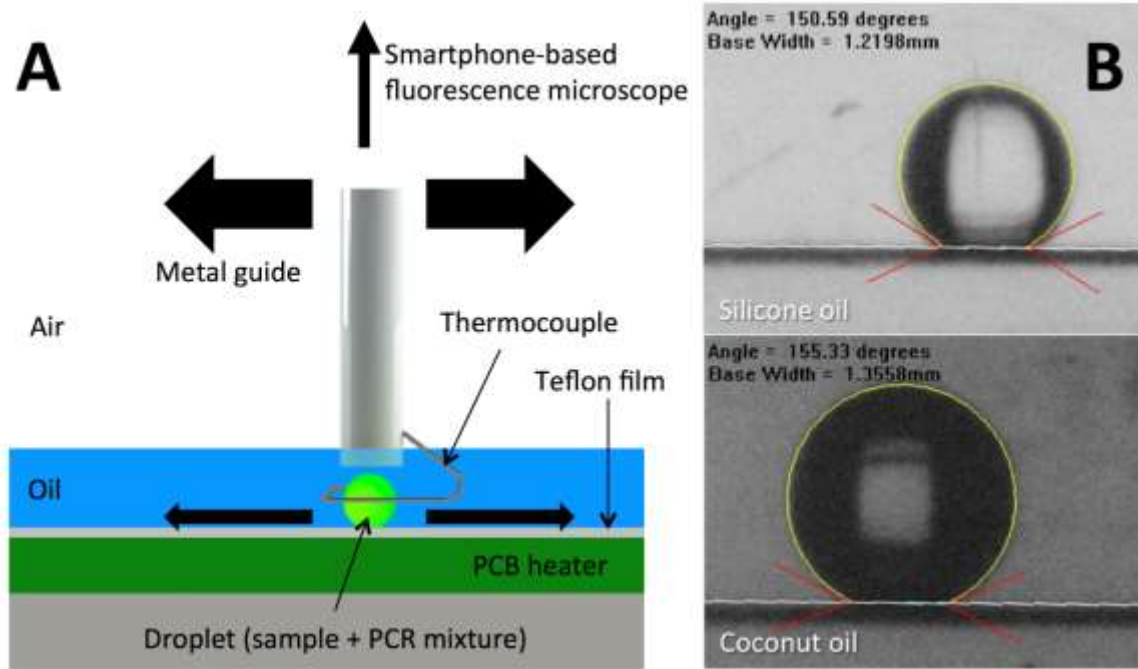


Figure A - 3

(A) Graphical representation of the droplet being held steady with the thermocouple loop while simultaneously reading the internal droplet temperature for feedback to the controller. (B) The water droplet on the Teflon-coated heater surface in silicone oil immersion (top) and coconut oil immersion (bottom). The contact angle in silicone oil immersion is $154 \pm 2^\circ$ ($n = 6$), and the contact angle in coconut oil immersion is $157 \pm 1^\circ$ ($n = 6$).

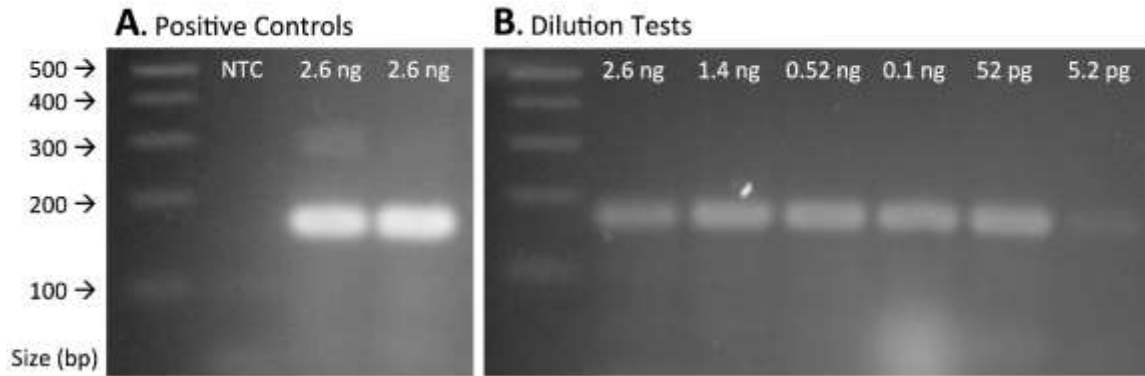


Figure A - 4

(A) Gel electropherogram showing results from the positive control experiment using 2.6 ng of genomic DNA (equivalent to 5.2×10^5 genomic copies) extracted from *E. coli* K12 and thermocycled for 30 cycles, with thermal cycle times of 30 s, on the surface-heated droplet PCR device. The genomic DNA was quantified by a Qubit 2.0 fluorimeter. The 196 bp product band is at the expected location, and there is no band observed for the no template control (NTC) sample. (B) Gel electropherogram showing the result of the dilution test. Genomic DNA in the range of 2.6 ng to 5.2 pg ($5.2 \times 10^5 - 10^3$ genomic copies) was thermocycled for 30 cycles, with thermocycle times of 30 s, on the surface-heated droplet PCR device. The PCR with the lowest DNA content (5.2 pg or approximately 10^3 genomic copies) produced a visible band.

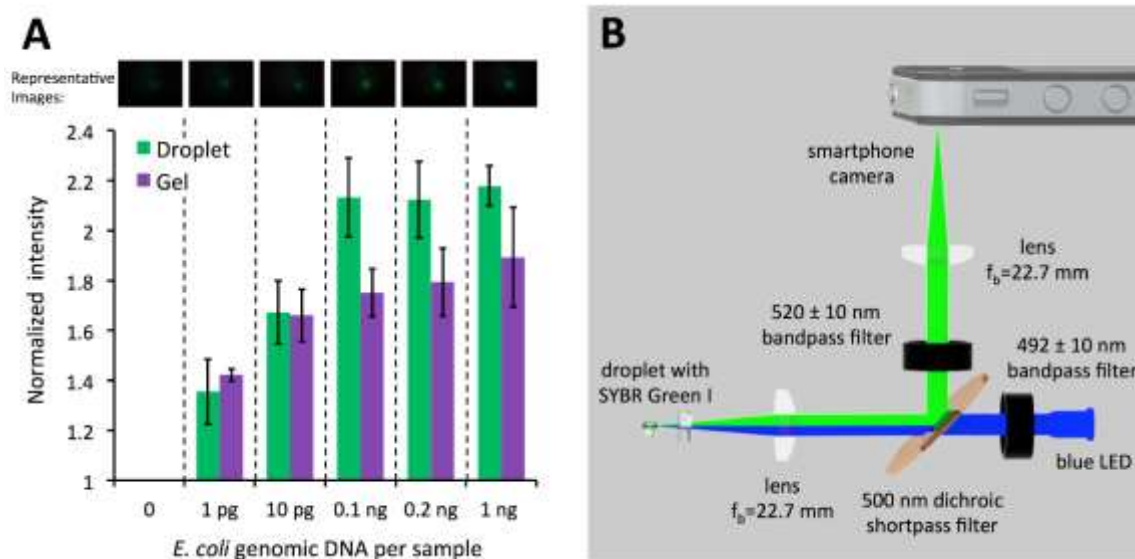


Figure A - 5

(A) Normalized intensity is plotted against the *E. coli* genomic DNA content of the reaction. Green bars (left) show the average green pixel intensities of the images taken with the smartphone-based fluorescence microscope of a droplet on the device after thermocycling. Purple bars (right) show the average band intensities for the same amplifications analyzed by gel electrophoresis. All results are normalized to no target controls (NTC = no *E. coli* gene + PCR mixture, amplified for 30 cycles). All results are the mean of three different experiments and error bars represent standard error. Representative fluorescence images of the droplet on the device are shown above the chart for each concentration. (B) Schematic of the optical layout of the smartphone-based fluorescence microscope, which is contained within the 3D printed housing. The excitation source is a 466 nm blue LED that is filtered by a 492 \pm 10 nm bandpass filter. A 500 nm dichroic shortpass filter separates the excitation light from the fluorescence emission from the droplet. The emission is further filtered by a 520 \pm 10 nm bandpass filter before reaching the smartphone camera. Two lenses are used to focus the light at the position of the droplet and on the smartphone camera.

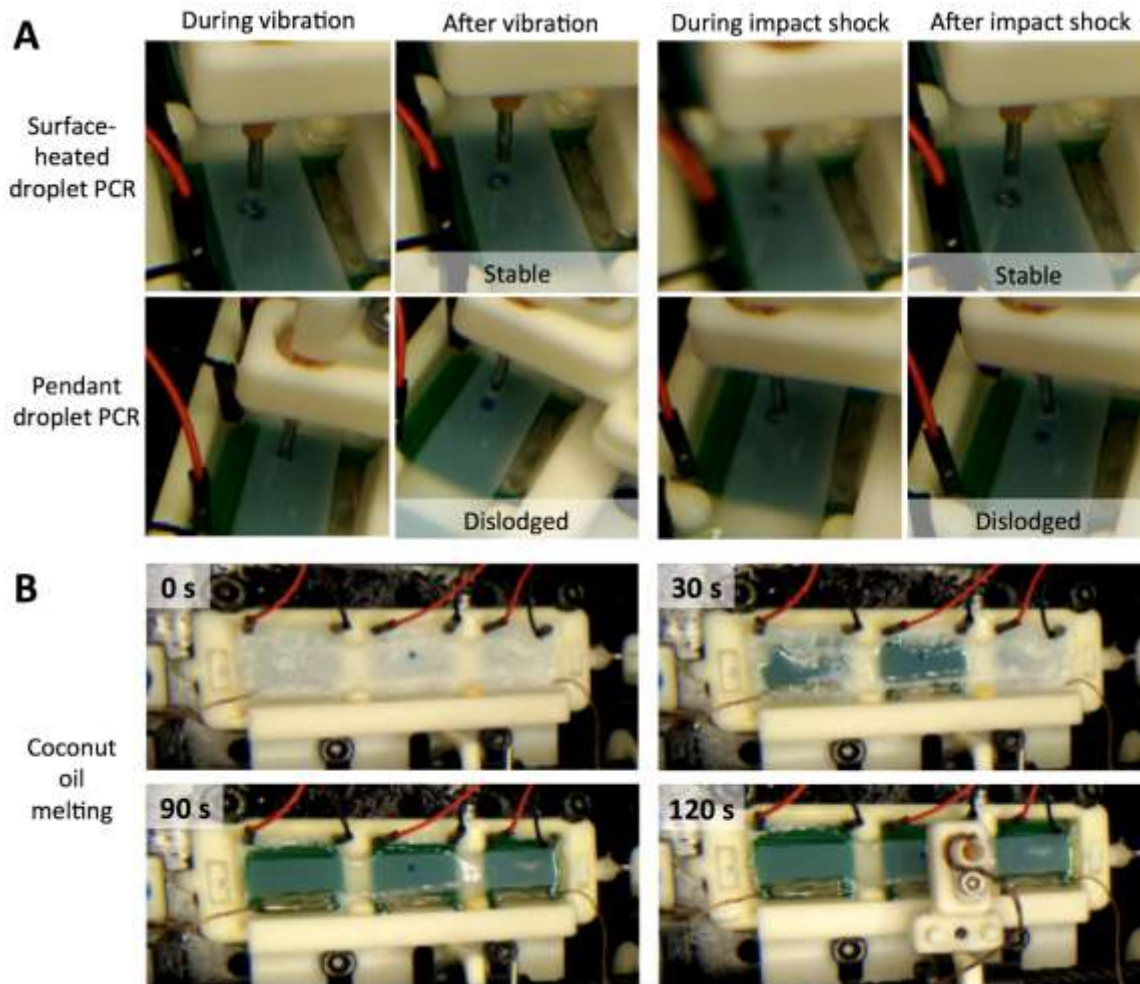


Figure A - 6

(A) Still images taken from a video of the vibration and impact shock tests of the surface-heated droplet PCR and the pendant droplet PCR methods. Images are shown during and after vibration and during and after impact shock (the during and after images are taken within 1 s of each other). The surface-heated droplet PCR method was able to successfully recover from vibration and impact shock and maintain droplet control. In comparison, the pendant droplet PCR method (where the droplet hangs from a syringe needle) was unable to recover from neither the vibration nor the impact shock and the droplet was dislodged from the needle tip. (B) Images taken from

Supplementary Video 1 of the coconut oil melting with a 9 μL droplet of PCR mixture contained within. The images are taken at 0, 30, 90, and 120 s.

Supplementary Video A - 1

A video demonstrating the portability of the droplet PCR system with coconut oil. The heating chambers are pre-filled with coconut oil that is solid at room temperature. Once the heaters are turned on, the coconut oil melts, revealing a 9 μL droplet of PCR mixture. A 1 μL sample that may contain bacterial genomic DNA is added to the droplet of PCR mixture, and the resulting droplet is subsequently thermocycled by moving across the surface of three heating chambers.

Operation of video can be found at <https://doi.org/10.1016/j.bios.2015.06.026>.

Appendix B

Smartphone-Based, Sensitive μ PAD Detection of Urinary Tract Infection and Gonorrhea

Soohee Cho^{a,†}, Tu San Park^{a,†}, Tigran G. Nahapetian^b, and Jeong-Yeol Yoon^{a,b,*}

^aDepartment of Agricultural and Biosystems Engineering and ^bBiomedical Engineering Graduate Interdisciplinary Program, The University of Arizona, Tucson, Arizona 85721-0038, U.S.A.

[†]These authors contributed equally to this work.

*Corresponding author at: Department of Agricultural and Biosystems Engineering, The University of Arizona, Tucson, Arizona 85721-0038, USA. Tel.: +1 520-621-3587; fax: +1-520-621-3963. URL: <http://biosensors.abe.arizona.edu>. E-mail address: jyoon@email.arizona.edu (J.-Y. Yoon).

Received 28 April 2015; received in revised form 22 June 2015; accepted 8 July 2015; available online 11 July 2015.

Biosensors & Bioelectronics **74**, 601-611 (2015)

© 2015 Elsevier B.V. – All rights reserved.

Abstract

The presence of bacteria in urine can be used to monitor the onset or prognosis of urinary tract infection (UTI) and some sexually-transmitted diseases (STDs), such as gonorrhea. Typically, bacteria's presence in urine is confirmed by culturing samples overnight on agar plates, followed by a microscopic examination. Additionally, the presence of *E. coli* in a urine sample can be indirectly confirmed through assaying for nitrite (generated by reducing nitrate in urine), however this is not sufficiently specific and sensitive. Species/strains identification of bacteria in a urine sample provides insight to appropriate antibiotic treatment options. In this work, a microfluidic paper analytic device (μ PAD) was designed and fabricated for evaluating UTI (*Escherichia coli*) and STD (*Neisseria gonorrhoeae*) from human urine samples. Anti-*E. coli* or anti-*N. gonorrhoeae* antibodies were conjugated to submicron particles then pre-loaded and dried in the center of each paper microfluidic channel. Human urine samples (undiluted) spiked with *E. coli* or *N. gonorrhoeae* were incubated for 5 minutes with 1% Tween 80. The bacteria-spiked urine samples were then introduced to the inlet of paper microfluidic channel, which flowed through the channel by capillary force. Data confirms proteins were not filtered by μ PAD, which is essential for this assay. Urobilin, the component responsible for the yellow appearance of urine and green fluorescence emission, was filtered by μ PAD, resulting in significantly minimized false-positive signals. This filtration was simultaneously made during the μ PAD assay and no pretreatment/purification step was necessary. Antibody-conjugated particles were immunoagglutinated at the center of the paper channel. The extent of immunoagglutination was quantified by angle-specific Mie scatter under ambient lighting conditions, utilizing a smartphone camera as a detector. The total μ PAD assay time was less than 30 seconds. The detection limit was 10 CFU/mL for both *E. coli* and *N. gonorrhoeae*, while

commercially available gonorrhea rapid kit showed a detection limit of 10^6 CFU/mL. A commercially available nitrite assay test strip also had a detection limit of 10^6 CFU/mL, but this method is not antibody-based and thus not sufficiently specific. By optimizing the particle concentration, we were also able to extend the linear range of the assay up to 10^7 CFU/mL. The proposed prototype will serve as a low-cost, point-of-care, sensitive urinalysis biosensor to monitor UTI and gonorrhea from human urine.

Keywords: urinalysis; paper microfluidics; *Escherichia coli*; *Neisseria gonorrhoeae*; urobilin; point-of-care; smartphone.

1. Introduction

Urinary tract infection (UTI) is a common problem among humans throughout the world. Although they are generally considered non-life-threatening, they may cause significant discomfort with potential for persistent reoccurrence, affecting the quality of a patient's life. As high as 40%-50% of UTIs are symptomatic and identified in primary care practices (Lin et al., 2011). Among those patients, 25% of them show retracted, reoccurring disease within 6 months (Lin et al., 2011).

Most UTIs are caused by *Escherichia coli*. In many cases, UTIs are associated with the *E. coli* found in the patient's own colon. Females show higher occurrence of UTI than males, due to the anatomical proximity of the urinary tract and anus in females. In some cases, UTI can spread from person to person, similar to sexually transmitted diseases (STDs). Some STD-causing bacteria can also reside in the urinary tract (similar to UTI), but are transmitted through sexual intercourse. Their symptoms are more severe and typically lead to higher medical costs (CDC, 2013). The most common STD that affects the urinary tract is gonorrhea, caused by *Neisseria gonorrhoeae*, which is the second most commonly reported STD in the United States (CDC, 2013). In 2013, there were 333,004 cases of gonorrhea reported by CDC (U.S. Centers for Disease Control and Prevention). Gonorrhea affects women as young as 15 (CDC, 2014).

Both bacterial infections, UTI and gonorrhea, are preventable by early detection, but this is arduous to do because most cases are often asymptomatic. CDC claims that a simplified screening method would provide a critical strategy for early identification and prevention (CDC, 2014). Currently available methods have such high detection limits that only cases showing symptoms are detected. At such stages, more treatment and costs are required due to further

progression of the disease. Therefore, there is a critical need for early diagnostic methods with increased sensitivity and specificity for bacterial agents of UTIs and STDs. Such methods can greatly reduce the long-term consequences of diseases and reduce healthcare costs, which are of high demand by healthcare agencies around the world (CDC, 2013).

High concentrations of *E. coli* and *N. gonorrhoeae* induce the symptomatic UTI and gonorrhea, respectively. At high concentrations, both types of bacteria can cause serious health effects to the host. Most cases, however, go undetected with asymptomatic behavior, as mentioned previously. The gold standard of detecting *E. coli* and *N. gonorrhoeae* is by culturing the urine sample and quantifying the bacterial concentration, which takes half a day for *E. coli* and 48 hours for *N. gonorrhoeae*. Lateral flow assays (LFAs; more precisely, lateral flow immunochromatographic assays), popularly known as rapid kits, are commercially available for detecting *N. gonorrhoeae*. However, they have high detection limits (typically 10^6 colony forming units or CFU per mL sample) and low sensitivities, making them unable to detect low concentrations of bacteria. This situation eventually causes complications with the development of an STD. There is currently no commercially available test for directly detecting *E. coli* (or other UTI-causing bacteria) from human urine. Colorimetric strips (not LFA) are available, detecting the presence of nitrites in urine. *E. coli* produces nitrate reductase that reduces nitrate in urine into nitrite (Hu et al., 2014; Lazzarini and Atkinson, 1961). These colorimetric strips are indirect, thus lacking specificity and sensitivity. In fact, these nitrite strips are unable to detect the low concentrations of bacteria necessary for the early detection of UTI or STD. Both direct gonorrhea LFAs and indirect nitrite strips typically require concentrated samples or overnight incubation to complement their insufficient detection limits, often combined with invasive sampling by inserting a swab into a patient's urinary tract. A newer platform is necessary,

detecting multiple types of UTI- and STD-causing bacteria with high specificity and sensitivity, as well as very low limit of detection that enables early detection of such infections.

Lately, microfluidic paper analytical devices (μ PADs) have gained much attention as an advantageous lab-on-a-chip (LOC) system. These LOC systems have previously been reported to include less sample and reagent consumption, lower power consumption, a lower per-unit cost, a reduced risk of contamination, higher reliability and functionality, automation and portability (Martinez et al., 2008; Park et al., 2013). μ PADs are biodegradable, make disease diagnosis cost-effective, and can be operated without the assistance of trained medical personnel. These features make μ PADs attractive for diagnostic applications in remote locations and the developing world (Sechi et al., 2013). Hence, numerous publications have recently appeared regarding μ PADs, but these systems still face the challenging demand for better sensitivity, especially when relying on colorimetric detection for diagnosis (Yetisen et al., 2013).

While urinalysis can be performed on μ PADs, detection of bacterial culture directly from human urine has been considered a laborious task. Urine is a complicated bio-fluid that usually requires sample pretreatment, such as purification and/or enrichment steps prior to analytical steps to determine specific components in the urine (Lin et al., 2011). Not to mention, the exposure of urine to benchtop-based protocols and devices increases risk of contamination and requires large sample volume. Literature reports that there is a necessity for automatic, miniaturized, inexpensive and easy-to-use microdevices for urinary sample pretreatment (Lin et al., 2011).

Previously, our group quantified the concentration of bacteria by evaluating the angle-specific Mie scatter signal from immunoagglutinated polystyrene particles (Fronczek et al., 2013; Park et al., 2013; You et al., 2011). By using paper microfluidic chips as our μ PADs along

with smartphone-based optical detection, *E. coli* was detected from waste water samples through quantifying the extent of immunoagglutination (Park and Yoon, 2015). However, our previous demonstration failed to detect *E. coli* concentrations higher than 10^5 CFU/mL (opposite problem to the conventional LFAs), due to the complex nature of *E. coli* colonies, i.e., they did not react with antibody-conjugated polystyrene particles sufficiently and reproducibly.

In Table 1, a summary of previously reported LOC-based assays for bacteria detection is provided. As reported, there few LFA or μ PAD methods that can efficiently detect bacteria. There are minimal amounts of methods (numbers 1-4) that detect bacteria directly from a urine sample matrix using microfluidic platforms (not LFA or μ PAD). Unfortunately, either pretreatment (filtration, centrifugation, and/or rinsing) was necessary or the detection limit was quite high (10^5 - 10^8 CFU/mL). There are a few methods that do report low detection limits within 100 CFU/mL (numbers 2, 9, 12 and 13). Most of these “low detection limit” methods utilized loop-mediated isothermal amplification (LAMP), which amplifies DNA targets to increase the concentration for their assays (numbers 2, 9 and 13), as well as the use of relatively clean sample matrix (e.g. buffer; number 9 and 13). In contrast to our near-real-time assay, none of the referenced methods are close to real-time and may take hours for results.

In this paper, we discuss our further development of μ PAD for the detection of *E. coli* and *N. gonorrhoeae* with fast assay time, low detection limit, and broader and clinically relevant range of detection, all directly from the human urine sample. We aim to accomplish these goals without any purification/enrichment steps, towards near-real-time assays (< 30 seconds). Additionally, we investigate how the paper fibers are beneficial in detecting bacteria from urine, specifically their filtration capability. *E. coli* concentration of 10^5 CFU/mL correlates with the onset of symptomatic UTI. As indicated previously, there is no commercially available LFA that

specifically detects *E. coli*. Our interest is the low-level detection of $10\text{--}10^3$ CFU/mL that may predict high risk of UTI development and allows early reaction to prevent UTIs. Specific and sensitive detection of other UTI-causing bacteria (most notably *Staphylococcus saprophyticus*) (Nicolle, 2008) should also be possible through switching the antibodies conjugated to the polystyrene particles. *N. gonorrhoeae* concentration of 10^5 CFU/mL correlates with the onset of symptomatic gonorrhea. Our interest is the detection of lower concentrations ($10\text{--}10^3$ CFU/mL) that may predict high risk of gonorrhea development, allowing for early reaction to prevent gonorrhea. For both cases, detection of higher bacterial concentrations (up to 10^7 CFU/mL; previously not demonstrated with this method) is demonstrated in this work, which correlates with substantially symptomatic UTI and gonorrhea. In addition, specificity experiments are also performed (again, previously not demonstrated with this method).

Overall, we aim to develop a point-of-care and near-real-time diagnostic tool with superior detection limit and sensitivity that can be used for wider ranges of bacterial concentrations and species, combined with the use of a smartphone. Previous studies show that the fast growing mobile phone market in the developing world has made camera phones a potential platform for the delivery of rapid diagnostics (Yetisen et al., 2013). Towards these goals, we attempt to evaluate and optimize the antibody conjugation procedure and particle concentration to make our assay fully adaptable to various disease conditions.

2. Materials and Method

2.1. Urine Samples with *Escherichia coli* and *Neisseria gonorrhoeae*

Escherichia coli solutions were prepared from lyophilized *E. coli* K12 cell powders (Sigma-Aldrich; St. Louis, MO, USA) by culturing them in brain heart infusion broth (Remel; Lenexa,

KS, USA) for 7.5 hours at 37°C. The culture reached its highest bacterial concentration of 10⁸ CFU/mL. Serial dilutions were made using normal urine from pooled human donors (Lee Biosolutions; St. Louis, MO, USA). This serial urine dilution allowed us to prepare virtually undiluted, *E. coli*-spiked urine samples. *E. coli* culture was measured by the plate counting method using brain heart infusion broth agar plates (BIO5 Media Facility; Tucson, AZ, USA). A standard curve of the serial *E. coli* K12 dilutions (10 to 10⁷ CFU/mL) was made by validating its concentration with the results of plate counting.

Neisseria gonorrhoeae solution was prepared from *N. gonorrhoeae* (catalog number 19424, ATCC; Manassas, VA, USA) by culturing in 814 medium for 48 hours at 37°C with 5% CO₂ using HERAcell 150i CO₂ incubator (Thermo Scientific, Waltham, MA, USA). The 814 medium recipe was provided by ATCC and custom made by BIO5 Media Facility. The culture reached its highest bacterial concentration of 10⁸ CFU/mL at 48 hours. The cultures were diluted by 2:1 with PBS (phosphate buffered saline; pH 7.4, Sigma-Aldrich). A 3-mL syringe (BD, Franklin Lakes, NJ, USA) with a 2-μL syringe filter (EMD Millipore, Billerica, MA, USA) was used to isolate the cells from the contaminants and bulky constituents in the media. Serial dilutions were made using the normal urine from pooled human donors (Lee Biosolutions). Again, virtually undiluted, *N. gonorrhoeae* urine samples were prepared with this serial urine dilution. *N. gonorrhoeae* cultures were evaluated with the plate counting method using 814 medium agar plates (BIO5 Media Facility). After validating its concentration with the results of plate counting, a standard curve of the serial *N. gonorrhoeae* dilutions (10 to 10⁷ CFU/mL) was made. Confirmed 10⁷ CFU/mL sample was further incubated for 7 to 9 days to mimic the realistic and symptomatic high concentration of *N. gonorrhoeae* in the human body.

2.2. Fabrication of Paper Microfluidic Chips

Microfluidic channels were patterned on paper using a standard lithography technique with UV exposure/development (Park et al., 2013). The multi-channel paper microfluidic chip (hereafter paper chip) was fabricated using cellulose chromatography paper (thickness = 100 μm ; GE Healthcare; Kent, UK). A mask of each chip consisted of four channels: negative control, low detection, middle detection, and high detection. The cellulose chromatography paper was immersed in SU-8 2010 negative photoresist (Microchem; Westborough, MA, USA) and then UV-exposed with the multi-channel mask following pre-baking. The paper chip was rinsed with acetone (Sigma-Aldrich) and isopropyl alcohol (Sigma-Aldrich). Each channel consisted of a straight channel (2.5 mm x 11.5 mm), including an area of detection where antibody conjugated particles were loaded, and an oval shape for an absorbent pad (4.5 mm x 5.5 mm) (Figure 1).

2.3. Antibody Conjugation to Particles

Goat polyclonal antibody to *E. coli* (catalog number B47385G, Meridian Life Sciences; Memphis, TN, USA) was used for *E. coli* detection. Rabbit polyclonal antibody to *N. gonorrhoeae* (catalog number PA 1-7233, Pierce-Antibodies; Rockford, IL, USA) was used for *N. gonorrhoeae* detection. To eliminate the need for a separate negative control solution, bovine serum albumin (BSA; Sigma-Aldrich) was also used to generate negative control signals (I_N) with bacteria-positive urine samples. In this way, a separate negative solution (bacteria-negative urine sample) was not necessary.

Anti-*E. coli* antibody, anti-*N. gonorrhoeae* antibody, and BSA were covalently conjugated to highly carboxylated, 920-nm diameter, polystyrene latex particles (Magsphere; Pasadena, CA, USA). These particles were selected from a wide variety of particles varying diameter and

vendors, through evaluating their stability (preferably all singlets) and polydispersity index (preferably less than 1.05) via light microscopy and dynamic light scattering. Antibodies were covalently conjugated to the particles by the following method: a solution of antibodies or BSA with activation buffer, 50 mM 2-(N-morpholino) ethanesulfonic acid (MES; Sigma-Aldrich) at pH 6.0, was prepared. The particles were added to the antibody (or BSA) solution and rocked for 15 minutes at room temperature. Water-soluble carbodiimide (Sigma-Aldrich) and 1 M sodium hydroxide (Sigma-Aldrich) were added to the antibody-particle (or BSA-particle) solution to yield saturated surface coverage on the particle surface, and rocked for 2 hours at room temperature. 1 M glycine (Sigma-Aldrich) was added to yield a final concentration of 100 mM to quench the reaction, which rocked for 30 minutes at room temperature. The antibody-particle (or BSA-particle) suspension was centrifuged and washed with deionized water a total of three times. After the final centrifuge, the particles were soft centrifuged to isolate non-specific aggregates from the suspension. Antibody-conjugated particles were stored in deionized water in 3-8°C.

2.4. Assay Procedure

The concentrations of antibody-conjugated particle suspension were calibrated by measuring 45° forward light scattering of particle suspension on a 2-well slide, using the device described in our previous work (You et al., 2011). These concentration-calibrated particles were loaded to the detection area (center of each channel, next to white linear marker). The final amount of particles loaded to the detection area was varied from 0.50 µg, 1.0 µg to 1.9 µg. The volume of particle suspension that was loaded on the paper was 3.4 µL. All paper chips were dried in room temperature prior to use.

A 1% solution of Tween 80 (Sigma-Aldrich) was added to each bacteria-spiked urine sample to release free antigens from bacterial aggregates for 5 minutes. Each bacteria-spiked urine sample (with Tween 80) was loaded on the inlets of the paper chip, resulting in capillary flow of urine samples. Scatter detection was done using a smartphone (iPhone; Apple, Inc., CA, USA) 30 seconds after sample loading.

Specificity experiments were performed for 10^5 CFU/mL *E. coli* samples in urine using anti-*N. gonorrhoeae* antibody conjugated particles (1.0 μ g), as well as 10^5 CFU/mL *N. gonorrhoeae* samples in urine using anti-*E. coli* antibody conjugated particles (1.0 μ g).

2.5. Smartphone-Based Detection and Data Analysis

The smartphone was arranged in an angled holder. The paper chip was placed 9 cm vertically from the smartphone camera. The smartphone was positioned 115° from the incident light (ambient lighting) or 25° from the paper chip, following the results of Mie scatter simulations (see Results section) using the software by Laven (2013) (Supplementary Material 1). Fluorescent lamps on the laboratory ceiling (ambient light) were used as a light source for image acquisition from the paper chip. Images were taken after locking exposure, focus, and white balance for both before (background signal) and 30 seconds after (sample signal) the samples were loaded, and when the samples reached the neck of the absorbent pad. These images were analyzed using ImageJ (U.S. National Institutes of Health; Bethesda, MD, USA) in a separate desktop computer, in which the pictures of channels were split to red, green and blue images. Green images were assessed to analyze the extent of scattered intensity, which has shown maximum changes under ambient lighting in previous findings (Park and Yoon, 2015). On ImageJ, rectangular areas adjacent to the normalized line marker from the central region of each

channel were analyzed. In these areas of interest, the antigens in the sample traveled through the channel and bind with the pre-loaded antibody-conjugated particles.

After the particles were pre-loaded and dried to the center of each designated channel, a “background intensity” (I_B) from each channel was taken. An example is shown in Figure 1C where I_{NB} was obtained from the negative channel with BSA-particles and I_{LB} from the low channel with antibody-particles loaded. Sample intensity (I_N from the negative channel and I_L from the low channel) was taken from each channel after bacteria-spiked urine had traveled past the central pre-loaded location. The background-normalized signal from the negative channel was I_N / I_{NB} , and thereafter for the low channel was I_L / I_{LB} . Channel-to-channel variations and the effect of different ambient light conditions were canceled out through this first normalization step.

A second normalization step was performed by dividing the above background-normalized signals from low, medium, and high detection channels with that of a negative channel. For example, the final signal from the low channel should be $(I_L / I_{LB}) / (I_N / I_{NB})$. Variations among different batches of antibody- or BSA-conjugated particles, specifically their extent of aggregation before the immunoagglutination assays, were eliminated through this second normalization step.

BSA-conjugated particles did not immunoagglutinate with either target, effectively resulting in a negative control signal without the need for a separate negative control solution, thus eliminating chip-to-chip and assay-to-assay variations. The use of BSA-conjugated particles with bacterial targets eliminates the concern of non-specific aggregation of the particles, greatly reducing the possibility of false-positive results. However, BSA-particles did show slight non-specific binding with each other prior to pre-loading on paper.

A series of double-normalized intensity values were plotted against the concentrations of *E. coli* and *N. gonorrhoeae*. Three sets of different experiments were performed per graph to provide standard error bars and support consistency of the assays. For every double-normalized intensity data, different paper chips (each loaded with antibody- or BSA-conjugated particles) were used.

2.6. μ PAD Filtration of Proteins from Urine

To investigate the filtration effect during the capillary flow of a urine sample through paper fibers, the previously described cellulose chromatography papers were cut out into small pieces and placed in a sterile, disposable filter unit (Nalgene Rapid-Flow, Thermo Scientific). Unfiltered normal human urine was filtered through to result in filtered human urine.

Firstly, the amount of total protein was quantified before and after filtration using the DC™ protein assay (based on the modified Lowry method; Bio-Rad Laboratories; Hercules, CA, USA) using the manufacturer's protocol (Bio-Rad Laboratories, 1995). BSA (Sigma-Aldrich) was used to generate a standard curve. Microarray scanner (Spectramax M2, Molecular Devices; Sunnyvale, CA, USA) was used to read the colorimetric signals from the samples. To further assess the size and the amount of proteins in the filtered urine, sodium dodecyl sulfate polyacrylamide gel electrophoresis (SDS-PAGE) was used for both unfiltered and filtered urine. Gel casting was performed according to the quick reference sheet by Life Technologies (2014). SDS-PAGE was performed following an available protocol (Sino Biological, 2014) with 12.5% resolving gel and 5% stacking gel. Empty gel cassettes (catalog number NC2015, Thermo Fisher Scientific) were used to prepare gels. XCell SureLock Mini-Cell (Thermo Fisher Scientific) was used to run electrophoresis. The amount of protein loaded was 25 μ g per sample. The standard

protein markers with molecular weights from 10-250 kDa (Precision Plus Protein Dual Color, Bio-Rad Laboratories) were used. Gel was stained with Imperial Protein Stain (Thermo Fisher Scientific), according to its provided protocol (Thermo Fisher Scientific, 2010). The gel was destained overnight on an orbital shaker in ultrapure water, and read with a gel scanner (Chemidoc XRS+, Bio-Rad Laboratories). ImageJ software was used to analyze the bands.

2.7. μ PAD Filtration of Urobilin from Urine

Fluorescence characteristics of unfiltered and filtered urine sample were evaluated in disposable plastic cuvettes, excited with a blue LED light source (LS-450, Ocean Optics; Dunedin, FL, USA). Spectra were measured using a pair of optical fibers (R400-7-UV-VIS, Ocean Optics), connected to a miniature spectrometer (USB4000, Ocean Optics) with accompanying software (SpectraSuite, Ocean Optics). Our specific molecule of interest was urobilin, which is responsible for the yellow coloration of urine. Urobilin is excited at 450 nm (blue) and emits green fluorescence at 530 nm (Craine, 2002).

To investigate whether urobilin (and its precursor form urobilinogen) is responsible for non-specific aggregation of particles, urobilinogen solutions were prepared, passively converted to urobilin (as it happens in typical urine samples within 24-hour incubation time) (Cornelius, 1980), and added to the antibody-particles. Solutions of urobilinogen (catalog number 651-10, Lee Biosolutions) were prepared at concentrations of 2.5 mg/L and 0.75 mg/L, while the mean value of urobilinogen in 24-hour urine is 0.71 mg/L (Kerkhoff and Peters, 1968), therefore representing high and normal urobilin concentrations. Both dilutions were exposed to ambient lighting at room temperature up to 24 hours to induce *in vitro* oxidation of urobilinogen to urobilin (Cornelius, 1980). These solutions were added to anti-*E. coli* antibody-particles at 1:1

ratio, and incubated in a refrigerator (4°C) for 24 hours. These mixtures were observed under the light microscope immediately after mixing and after 24-hour incubation.

2.8. Assays with Commercial Strips

Gonorrhea Rapid Test (Home-bio-test.com; Bloomington, CA, USA) was used as the commercially available test strips for *N. gonorrhoeae* detection. The instructions provided by each test kit were followed using 20 μ L of undiluted human urine sample with 10^5 and 10^6 CFU/mL *N. gonorrhoeae*.

For the commercial nitrite strips, Uriscan (YD Diagnostics, Yongin, Gyeonggi-do, Republic of Korea) was used. After incubating *E. coli* with 0.01 M sodium nitrate (ThermoFisher Scientific; Lazzarini) for 8 hours, the solution was serially diluted as described previously. Uriscan strips were used following the provided instructions with 8 μ L of 10^4 , 10^5 , and 10^6 CFU/mL *E. coli*. Images of color intensity were taken with a smartphone and analyzed with ImageJ.

2.9. Statistical Analysis

All reported p-values were obtained from paired t-tests of sample versus blank (i.e. bacteria-negative urine sample) performed by Stata/IC 12.0 (StataCorp LP, 2011) using $\alpha = 0.05$.

3. Results

3.1. Optimization of Particle Loading to Paper Chips

Initially, the procedures and protocols described in our previous publications (Park et al., 2013; Park and Yoon, 2015) were used without any modifications in assaying *E. coli* and *N.*

gonorrhoeae from undiluted human urine. The normalized scattering intensity values were quite small and not consistent from experiment to experiment. According to the microscopic images of the antibody-conjugated particles before and after the assays, we found non-specific aggregations before the assay, presumably due to the particles' instability. In addition, the amount of antibody-particles in each channel should be optimized specifically for this type of assay. Therefore, in this work, we decided to soft centrifuge the antibody-conjugated particles to isolate these non-specific aggregations prior to their loading onto the paper microfluidic chips. With this procedure, the antibody-conjugated particles mostly existed in singlet form (Figure 1C inset), while the ones mixed with 10^5 CFU/mL *E. coli* showed increased extent of immunoagglutination (Figure 1C inset). However, this soft-centrifuging resulted in varying the particle concentration. We complemented this variance by measuring the 45° forward light scattering of particle suspension using a two-well slide and the scattering reader device described in You et al. (2011), followed by adding the necessary amount of deionized water to the particle suspension. Supplementary Material 2 shows microscopic images of anti-*E. coli* antibody-particles right after completing covalent conjugation (A) and after soft centrifugation (B), clearly indicating elimination of non-specifically aggregated antibody-particles.

As described in the Materials and Method section, fixed concentrations and amounts of antibody-conjugated particles were loaded onto the central part of each channel and subsequently dried out. There were four channels. 1) "Negative" channel, where BSA-conjugated particles were loaded, provided a negative control signal (I_N), without the need for a separate negative control solution, since BSA-conjugated particles would not immunoagglutinate in the presence of target bacteria. 2) "Low" channel, where 0.5 μ g antibody-conjugated particles were loaded, provided a target signal (I_L). 3) "Medium" channel, where 1.0 μ g of antibody-conjugated

particles were loaded, provided a target signal (I_M). 4) “High” channel, where 1.9 μg of antibody-conjugated particles were loaded, provided a target signal as well (I_H). Undiluted urine samples with varying concentrations of *E. coli* and *N. gonorrhoeae* were loaded to all four channels at the same time, eliminating any possible chip-to-chip variation between the measurements of I (i.e. I_L , I_M and I_H) and I_B .

The first normalization step, dividing I_N with I_{NB} for the negative channel and I_L with I_{LB} for the low channel, etc., eliminated the effects of any variations in paper morphology and ambient lighting conditions (Figure 1C). The second normalization step, dividing the background-normalized intensity of low, medium or high channel (e.g. I_L/I_{LB}) with that of negative channel (I_N/I_{NB}), eliminated the variations among different batches of antibody- or BSA-conjugated particles, including a slight variation in particle concentration (despite being calibrated as described in Materials and Method), small extent of pre-aggregation (despite being soft-washed as described in Materials and Method), etc. Supplementary Material 1 shows Mie scattering simulation, indicating that 116° has the greatest change in scattering intensity as the particle size increased to represent the increase from immunoagglutination. To maintain consistency, we used 115° to position our smartphone, since our positioning assembly utilized increment changes of 5° , as shown in Figure 1.

The final amount of antibody-conjugated particles loaded onto the chips were, as described previously, 0.50 μg , 1.0 μg , and 1.9 μg for both detection of *E. coli* and *N. gonorrhoeae*. These numbers were selected from various different trials that maximized the linear range of the assay. The concentrations (w/v) of BSA-conjugated particles were made to be the same as those of antibody-conjugated particles. For comparison purpose, blank samples (0 CFU/mL bacteria in human urine) were also tested with BSA-particles and antibody-particles, which should generate

the normalized intensities very close to 1, but not necessarily exactly 1. Paired t-tests were performed between this blank and each target concentration, and * marks were provided in Figures 2 and 3 for the results substantially different (with $p < 0.05$) from the blank result, indicating the positive assay results.

3.2. *E. coli* Detection

Figure 2 shows the results with paper microfluidic detection of *E. coli* from undiluted human urine. With 0.50 μg particles, the double-normalized intensities increased up to 10^3 CFU/mL *E. coli*, followed by a decrease with larger error bars. The lowest concentration that passed the paired t-test with blank solution (i.e. undiluted human urine with no *E. coli*) was 10^1 CFU/mL ($p < 0.05$), which is the detection limit of this assay. With 1.0 μg particles, the linear range was extended to 10^5 CFU/mL. With 1.9 μg particles, the linear range was further extended to 10^7 CFU/mL, at a cost of inability to detect low *E. coli* concentrations. Specificity experiments for 10^5 CFU/mL *E. coli* samples in urine using *N. gonorrhoeae* antibody conjugated particles (1.0 μg) did not result in any significant changes.

3.3. *N. gonorrhoeae* Detection

Figure 3 shows the results with paper microfluidic detection of *N. gonorrhoeae* from undiluted human urine. With 0.5 μg particles, the double-normalized intensity values increased up to 10^5 CFU/mL, but the changes were relatively small with large error bars. With 1.0 μg particles, the double-normalized intensity values were greater than those with 0.5 μg particles, as well as those with *E. coli*. The normalized intensities increased up to 10^3 CFU/mL followed by a decrease. The detection limit was demonstrated to be 10 CFU/mL ($p < 0.05$). With 1.9 μg

particles, even larger normalized intensities were obtained, with the detection limit again at 10 CFU/mL ($p < 0.05$), while the signals kept increasing to 10^7 CFU/mL. Specificity experiments for 10^5 CFU/mL *N. gonorrhoeae* samples in urine using anti-*E. coli* antibody conjugated particles (1.0 μ g) did not result in significant changes, similar to the case of *E. coli* specificity experiments.

3.4. μ PAD Filtration of Proteins from Urine

To evaluate the filtration of urine through the μ PAD channel, undiluted human urine samples were filtered through the cellulose chromatography papers and various assays were performed before and after filtration (Figure 4). Urine was noticeably more transparent after filtration, as shown in Figure 4C. DCTM Protein Assay results were 1.64 mg/mL for the unfiltered urine and 1.57 mg/mL for the filtered urine, indicating no substantial filtration of total proteins. SDS-PAGE results of unfiltered and filtered urine are shown in Figure 4A,B. Two bands were observed from both unfiltered and filtered urine samples, a strong band at 67 kDa and a faint band at 26 kDa, which were consistent with the bands from urine of control subjects (Nesselhut et al, 1989). No significant change in band intensities were observed between unfiltered (Figure 4A) and filtered urine (Figure 4B). Subsequent ImageJ analysis of the gel enabled pixel profile analysis, with slight increase of the 67 kDa band in the filtered urine sample and no difference in the 26 kDa band. Again, no substantial filtration of proteins (reduction in concentration) was indicated from these SDS-PAGE experiments.

3.5. μ PAD Filtration of Urobilin from Urine

The fluorescence spectra of unfiltered and filtered urine samples are shown in Figure 4D and the actual fluorescence within a plastic cuvette is shown in Figure 4E. Both results suggest substantial reduction in fluorescence, with a peak at 530 nm upon 450 nm blue irradiation, which was identical to the fluorescence behavior of 24-hour incubated urobilinogen (= mostly urobilin) solution. These results suggest that substantial amount of urobilin was filtered through cellulose fibers and subsequently in μ PAD.

To investigate the possible negative impacts of urobilin to the particle stability, 2.5 mg/L and 0.75 mg/L urobilinogen solutions (24-hour incubated, thus mostly urobilin; simulating high and normal level of urobilin, respectively) were added to the anti-*E. coli* antibody-particles (Supplementary Material 3). In all cases, the singlet particles were unaffected (i.e., did not aggregate) after 24 hours of incubation, indicating that urobilin did not destabilize the antibody-particles.

3.6. Commercial Test Strips

The manufacturer of the commercially available LFA (antibody-based) for *N. gonorrhoeae* reports that their detection limit is 10^6 CFU/mL. Using the identical, undiluted human urine samples spiked with *N. gonorrhoeae*, a faint positive band was observed with 10^6 CFU/mL sample, while no positive band was observed with 10^5 CFU/mL sample, confirming the detection limit reported by the manufacturer (Figure 5A).

Currently, there is no commercial LFA for *E. coli* detection from urine. However, we used a commercially available colorimetric strip that can detect nitrite. The same, undiluted human urine samples spiked with *E. coli* were mixed with sodium nitrate and incubated as mentioned in

Materials and Method. The resulting solutions were tested using the colorimetric nitrite strips. Unlike the gonorrhea LFAs, colorations should be quantified by comparing with the color chart provided by the manufacturer. To provide quantifiable results for this assay, the normalized color intensities were obtained using ImageJ software. Results (Figure 5B) show no significant change in color intensity for 10^4 CFU/mL *E. coli* in urine. For 10^5 CFU/mL, there was a slight change as the strip appeared pale pink. For 10^6 CFU/mL, there was a significant change as the strip appeared bright pink. Although the strip with 10^5 CFU/mL showed slight increase in coloration, paired t-test resulted in a p-value of 0.053. Hence, the detection limit of this assay is 10^6 CFU/mL ($p < 0.0001$), although this assay is not specific to *E. coli*.

4. Discussion

Various available rapid tests for UTI and gonorrhea are nonspecific with high detection limits. The current reliant method for physicians to diagnose UTI and gonorrhea in patients is by extracting the tissue/bacteria sample from the urethra in men or from the cervix in women. The sample is sent to a lab where it is cultured for at least half a day for *E. coli* and 48 hours for *N. gonorrhoeae*. Using this method, the patient receives their results days after visiting the physician. The available test strips are convenient and meet the demands of point-of-care testing, but sensitivity is insufficient to detect the level of infection that is asymptomatic.

Our previous research supports that immunoagglutination of antibody-conjugated particles provides a specific method of detecting *E. coli* from wastewater (Park and Yoon, 2015). Current work is an improvement by targeting bacterial agents that cause UTI and STD (specifically gonorrhea), directly from the sample matrix – urine. Although there are commercial LFAs available for gonorrhea, we prove that our assay has a lower detection limit (10 CFU/mL vs. 10^6

CFU/mL). Considering the volume of human urine that flowed through each channel (7 μ L), this detection limit (10 CFU/mL) corresponds to sub-single-cell level. This is still possible since we are detecting antigens from bacteria but not the viable cell colonies. We have previously addressed this sub-single-cell level detection with particle immunoagglutination assays, most notably in Han et al. (2008). Our assay is also superior in detecting UTI, with a superior detection limit (10 CFU/mL) and antibody-based specificity, which is not possible with the currently available nitrite strips.

Our urinalysis biosensor provides a fast point-of-care method for easy and early detection of *E. coli* and *N. gonorrhoeae*. The amount of particles loaded onto paper was optimized to specifically detect certain ranges of target concentrations. The particles were also soft-centrifuged to isolate non-specific aggregates, illustrated in Supplementary Material 2, to improve the reproducibility and specificity of the assays. In preliminary studies that lacked soft-centrifuging and optimization of antibody-particle amount, assays resulted in very small signal changes and were not reproducible. In addition, BSA-conjugated particles were used for “negative” channel, which eliminated the need for a separate negative control solution. The superior detection limit (10 CFU/mL) and wider range of assays (up to 10^7 CFU/mL) for *E. coli* and *N. gonorrhoeae* from undiluted human urine allows detection for both asymptomatic and symptomatic patients.

The data shown in Figure 2A (*E. coli* assay with 0.50 μ g particles) indicates that the assay worked quite well up to 10^3 CFU/mL, while the average normalized intensities for 10^4 CFU/mL and 10^5 CFU/mL are quite small with extremely large error bars. This result indicates that the range of assay is 10 – 10^3 CFU/mL with 0.50 μ g of antibody-particles. This range of assay is shifted to higher concentrations by increasing the amount of antibody-particles loaded on the

paper microfluidics: 10^3 – 10^5 CFU/mL with 1.0 μg of antibody-particles (Figure 2B) and 10^5 – 10^7 CFU/mL with 1.9 μg of antibody-particles. Within these respective usable ranges, our μPAD assay reproducibly generated statistically relevant signals. To note, we see that 10^7 CFU/mL data with 1.9 μg particles had slightly larger error bars, which is explainable by the larger colonies at such high concentration.

In accordance with the previous findings, we expected to achieve a similar optimization for *N. gonorrhoeae* assays. As shown in Figure 3A, 0.5 μg of particles did lead to a small increase in signal up to 10^5 CFU/mL, but had inferior sensitivity. The particle amount of 1.0 μg (Figure 3B) provided good sensitivity with a very low detection limit of 10 CFU/mL, while the linear range was up to 10^3 CFU/mL. Further increasing the particle amount to 1.9 μg extended the linear range to 10^5 CFU/mL, with the large normalized intensity at 10^7 CFU/mL (Figure 3C).

In general, reproducible results could be obtained for the given range of assays, which could be adjusted by varying the amount of antibody-particles loaded on μPAD (0.50, 1.0, and 1.9 μg). For practical applications, three pairs of channels can be simultaneously used, each with different amount of antibody-particles, to cover the whole range of bacterial concentrations. Detection limits for both *E. coli* and *N. gonorrhoeae* were 10 CFU/mL, which were much lower than the commercially available test strips (10^6 CFU/mL with gonorrhea LFA and 10^6 CFU/mL for nitrite strip).

Further investigations were performed to determine the extent of urine filtration by the cellulose fibers of μPAD . Since urine samples continuously flowed through cellulose fibers along each channel, the cut-out chromatography papers were used in a filter unit to best model our μPAD filtration. The reduction in coloration of the filtered urine initially suggested a decrease of some component(s) in urine. Proteins were initially suspected. However, DC™

Protein Assay results were not substantially different between unfiltered urine (1.64 mg/mL) and filtered urine (1.57 mg/mL). SDS-PAGE results also confirmed the same trend – no substantial difference in band intensities between unfiltered and filtered urine. Hence, protein was determined not the causation of coloration loss. Further investigation on urobilin was conducted, which is the pigment responsible for the yellow appearance of urine (Bixler et al., 2014). In fact, it was stated in 1925 that the fluorescence of urobilin could be accurately measured by use of a spectrophotometer (Elman and McMaster, 1925). The study reported the spectrometric characteristic of urobilin: blue excitation (460 ± 20 nm) and green emission (520 ± 20 nm) (Bixler et al, 2014). Both unfiltered and filtered urine were tested for green fluorescence emission with blue irradiation, and substantial decrease in urobilin fluorescence at 530 nm was observed (Figure 4D). This suggests that urobilin was filtered by the chromatography papers and subsequently the μ PAD. It is possible that the abundant amine and carboxyl groups in urobilin may form strong hydrogen bonds with also abundant hydroxyl groups in cellulose, with minimum steric hindrance due to the relatively small size of urobilin compared to typical proteins.

To investigate adverse effects of urobilin to our μ PAD assay, urobilin solutions were added to antibody-particles to observe its effects on particle stability. The particles remained mostly singlets when mixed with both 2.5 mg/L and 0.75 mg/L urobilin solutions (Supplementary Material 3). Thus, urobilin does not have adverse effects on particle stability that may lead to non-specific aggregation.

Green fluorescence of urobilin, however, does exhibit strong adverse effect to our μ PAD assay, since it shows very strong green fluorescence and we utilized green channel images to collect the signals, where the Mie scatter intensities were maximum. By reducing urobilin

concentration, any anomaly in green channel intensities from the urine sample could be minimized. Without filtering or reducing false positive signals by urobilin, other assays based on colorimetry are susceptible to error and lack of sensitivity.

Overall, our biosensor for both targets provides compelling evidence of its superiority to the current methods of detecting *E. coli* and *N. gonorrhoeae*. By rapid and specific detection of the two targets, this method provides an easy tool for diagnosing or even preventing the onset of UTI or gonorrhea. With its paper microfluidic chip format, this system can come preloaded with the optimized particle concentrations as a user-friendly sensor that does not require a physician to execute. Especially considering the widespread use and feasibility of smartphones for image analysis, our smartphone based biosensor provides patients with a diagnostic method that eliminates the overwhelming costs and time-consuming lab work of current methods. Not to mention, we present the first LFA of its kind to detect low concentrations of *E. coli* from human urine without having to detect indirect parameters such as nitrite.

Future direction of this research towards commercialization would be an improvement in user-friendliness. For example, we can fabricate paper microfluidic chips that include four channels that are optimized for detection of negative control, low concentration (i.e. $10-10^3$ CFU/mL), medium concentration (i.e. 10^3-10^5 CFU/mL) and high concentration (i.e. 10^5-10^7 CFU/mL). Instead of quantifying exact bacterial concentration, the smartphone can simply provide an easy-to-understand assay result, such as 1) asymptomatic infection, 2) onset of infection, and 3) developing infection. Such a biosensor can provide prognosis on whether a patient is at risk for developing UTI/gonorrhea, having UTI/gonorrhea, or at extreme risk and threat by UTI/gonorrhea. Another valuable direction is a smartphone app that analyzes results of test strip without the need for separate desktop computer and image processing.

5. Acknowledgements

Funding for this research was provided by Seoul VioSys. Soohye Cho acknowledges the fellowship support from Richard A. Harvill graduate fellowship. The authors would also like to thank Dr. Daewoong “Dave” Suh and Dr. Kyujin Choi at Seoul VioSys for helpful discussions and guidance.

6. References

- Bercovici, M., Kaigala, G.V., M. K.E., Han, C.M., Liao, J.C., Santiago, J.G., 2011. *Anal Chem.*, 83, 4110-4117.
- Bio-Rad Laboratories, 1995. DC™ Protein Assay Instruction Manual. http://www.bio-rad.com/LifeScience/pdf/Bulletin_9005.pdf. (accessed 06.02.15)
- Bixler, J.N., Cone, M.T., Hokr, B.H., Mason, J.D., Figueroa, E., Fry, E.S., Yakovlev, V.V., Scully, M.O., 2014. *Proc. Natl. Acad. Sci. USA* 111, 7208-7211.
- CDC (U.S. Centers for Disease Control and Prevention), 2013. Incidence, Prevalence, and Cost of Sexually Transmitted Infections in the United States. <http://www.cdc.gov/std/stats/sti-estimates-fact-sheet-feb-2013.pdf> (accessed 02.05.2015).
- CDC (U.S. Centers for Disease Control and Prevention), 2014. Sexually Transmitted Disease Surveillance 2013. <http://www.cdc.gov/std/stats> (accessed 02.05.2015).
- Chang, W.-H., Wang, C.-H., Lin, C.-L., Wu, J.-J., Lee, M.S., Lee, G.-B., 2015. *Biosens. Bioelectron.*, 66, 148-154.
- Cornelius, C.E., 1980. Liver Function, in: Kaneko, J.J. (Ed.), *Clinical Biochemistry of Domestic Animals*, 3rd Edn. Academic Press: Massachusetts, pp. 201-257.

Craine, B.L., 2002. *U.S. Patent Application Publication*. U.S. 2002/0076820A1.

Elman, R., McMaster, P.D., 1925. *J. Exp. Med.* 31, 503-512.

Fang, X., Chen, H., Xu, L., Jiang, X., Wu, W., Kong, J., 2012. *Lab Chip*, 12, 1495-1499.

Fronczek, C.F., You, D.J., Yoon J.-Y., 2013. *Biosens. Bioelectron.*, 40, 342-349.

Golberg, A., Linshiz, G., Kravets, I., Stawski, N., Hilson, N.J., Yarmush, M.L., Marks, R.S., Konry, T., 2014. *PLoS ONE*, 9, 1-9.

Han, J.-H., Heinze, B.C., Yoon, J.-Y., 2008. *Biosens. Bioelectron.* 23, 1303-1306.

Hu, J., Wang, S., Wang, L., Li, F., Pingguan-Murphy, B., Lu, T.J., Xu, F., 2014. *Biosens. Bioelectron.*, 54, 585-597.

Jiang, X., Jing, W., Zheng, L., Liu, S., Wu, W., Sui, G., 2014a. *Lab Chip*, 14, 671-676.

Jiang, J., Wang, X., Chao, R., Ren, Y., Hu, C., Xu, Z., Liu, G.L., 2014b. *Sens. Actuat. B*, 193, 653-659.

Kerkhoff, J. F., Peters, H.J., 1968. *Clin. Chim. Acta* 21, 133-137.

Laven, P., 2013. *MiePlot* V.4.2.11. <http://philiplaven.com>. (accessed 01.08.2015)

Lazzarini, R.A., Atkinson, D.E., 1961. *J. Biol. Chem.*, 236, 3330-3335.

Liao, J.C., Mastali, M., Gau, V., Suchard, M.A., Møller, A.K., Bruckner, D.A., Babbitt, J.T., Li, Y., Gornbein, J., Landaw, E.M., McCabe, E.R.B., Churchill, B.M., Haake, D.A., 2006. *J. Clin. Microbiol.* 44, 561-570.

Life Technologies, 2014. Gel Casting Instructions. http://tools.lifetechnologies.com/content/sfs/manuals/gelcasting_man.pdf. (accessed 06.02.15).

Lin, C.-C., Tseng, C.-C., Chuang, T.-K., Lee, D.-S., Lee, G.-B., 2011. *Analyst*, 136, 2669-2688.

Martinez, A.W., Phillips, S.T., Carrilho, E., 2008. *Anal. Chem.*, 80, 3699.

- Nesselhut, T., Rath, W., Grospietsch, G., Weber, M.H., Kuhn, W., 1989. *Arch. Gynecol. Obstet.* 246, 97-105.
- Nicolle, L.E., 2008. *Urol. Clin. North Am.*, 35, 1-12.
- Packard, M.M., Shusteff, M., Alocilja, E.C., 2012. *Biosensors*, 2, 405-416.
- Park, T.S., Li, W., McCracken, K.E., Yoon, J.-Y., 2013. *Lab Chip*, 13, 4832-4840.
- Park, T.S., Yoon, J.-Y., 2015. *IEEE Sens. J.*, 15, 1902-1907.
- Pires, N.M.M., Dong, T., 2013. *Sensors*, 13, 15898-15911.
- Safavieh, M., Ahmed, M.U., Sokullu, E., Ng, A., Braescu, L., Zourob, M., 2014. *Analyst*, 139, 482-487.
- Safavieh, M., Ahmed, M.U., Tolba, M., Zourob, M., 2012. *Biosens. Bioelectron.*, 31, 523-528.
- Sechi, D., Greer, B., Johnson, J., Hashemi, N., 2013. *Anal. Chem.*, 85, 10733-10737.
- Sino Biological, 2014. Assay-Protocol SDS-PAGE. http://www.assay-protocol.com/uploads/Clean_Lilaic/SDS%20PAGE.pdf. (accessed 06.02.15).
- StataCorp LP, 2011. Stata/IC 12.0. <http://www.stata.com/>. (accessed 01.08.2015).
- Thermo Scientific, 2010. Instructions Imperial Protein Stain. https://tools.lifetechnologies.com/content/sfs/manuals/MAN0011533_Imperial_Protein_Stain_UG.pdf. (accessed 06.02.15).
- Wang, S., Inci, F., Chaunzwa, T.L., Ramanujam, A., Vasudevan, A., Subramanian, S., Ip, A.C.F., Sridharan, B., Gurkan, U.A., Demirci, U., 2012. *Int. J. Nanomed.*, 7, 2591-2600.
- Yang, Y., Kim, S., Chae, J., 2011. *J. Microelectromech. Syst.*, 20, 819-827.
- Yetisen, A.K., Akram, M.S., Lowe, C.R., 2013. *Lab Chip*, 13, 2210-2251.
- Yoo, J.H., Woo, D.H., Chang, M.-S., Chun, M.-S., 2014. *Sens. Actuat. B*, 191, 211-218.
- You, D.J., Geshell, K.J., Yoon J.-Y., 2011. *Biosens. Bioelectron.* 28, 399-406.

7. Figures and Table

Reference	Detection method	Bacteria	Detection limit	Pre-treatment	Assay time	Sample
Liao et al. (2006)	Micro-fabricated electrode array	<i>E. coli</i> <i>P. mirabilis</i> <i>K. pneumoniae</i> <i>E. aerogenes</i> <i>Pseudomonas</i> sp. <i>Enterococcus</i> sp. <i>E. coli</i>	2.6×10^8 CFU/mL 1.0×10^5 CFU/mL 4.0×10^4 CFU/mL 1.6×10^7 CFU/mL 1.0×10^5 CFU/mL 1.3×10^6 CFU/mL 10^6 CFU/mL	Lysis	45 min	Urine
Bercowici et al. (2011)	Microfluidic isotachopheresis with FRET	<i>E. coli</i>	48 CFU/mL	Centrifugation, lysis and dilution	15 min	Urine
Safaviieh et al. (2012)	Microfluidic LAMP with electrochemical detection	<i>E. coli</i>	3.4×10^4 CFU/mL	Filtration	60 min	Filtered urine
Yang et al. (2011)	Microfluidic cell impedance assay	<i>E. coli</i>	10^2 CFU (live bacteria), 10^2 – 10^4 CFU (typing bacteria)	No pre-treatment	100 min	Synthetic urine
Chang et al. (2015)	Colorimetric/PCR on a chip	<i>E. coli</i> , <i>S. aureus</i> , <i>P. syringae</i> , <i>Enterococcus</i> sp., <i>Staphylococci</i> sp. <i>E. coli</i>	50 CFU/mL	Automated washing on chip	30 min, +40 min for PCR	Human joint fluid
Wang et al. (2012)	Microfluidic fluorescence assay	<i>E. coli</i>	118 cells/reaction (10^4 – 10^6 CFU)	Filtering	30 min	PBS, blood and food
X. Jiang et al. (2014)	Gel electrophoresis/PCR on a chip	<i>E. coli</i> , <i>C. koseri</i> , <i>S. aureus</i> , <i>K. pneumoniae</i> , <i>E. faecalis</i> , <i>P. aeruginosa</i> <i>E. coli</i>	150 CFU/mL	Bacteria capture, washing, lysis and enrichment	70 min	Aerosol
Golberg et al. (2014)	Microfluidic fluorescence assay	<i>E. coli</i>	10^3 cells/mL	Filtering, incubation, on-chip enrichment	8 h	Water with feces
Yoo et al. (2014)	Microfluidic fluorescence assay	<i>E. coli</i>	10^3 cells/mL	Not reported	<30 min, +45 min staining	PBS
J. Jiang et al. (2014)	Microfluidic cell impedance assay	<i>E. coli</i>	10^3 cells/mL	Centrifuge and rinsing	Not reported	Water
Pires and Dong (2013)	Microfluidic chemiluminescence assay	<i>E. coli</i> <i>C. jejuni</i> Adenovirus <i>E. coli</i> , <i>M. tuberculosis</i>	5×10^5 cells/mL 10^5 cells/mL 10^{-8} mg/mL 10–100 copies of DNA	Not reported	<35 min	Water
Fang et al. (2012)	Microfluidic LAMP with fluorescence	<i>E. coli</i>	30 CFU/mL	Lysis and centrifugation	30–60 min	Water
Safaviieh et al. (2014)	Ribbon cassette LAMP with colorimetry	<i>E. coli</i> <i>S. aureus</i>	200 CFU/mL	Not reported	<1 h	Water
Packard et al. (2012)	Microfluidic FRET-ISH (in situ hybridization)	<i>E. coli</i>	10^2 CFU/mL	Centrifuge, dilution and dye staining	30 min	Water

Table B - 1

Summary of microfluidic assays previously reported for pathogen detection in literature. Reported techniques are compared regarding target bacteria, method of detection, sensing platform, detection limit, pretreatment, assay time, and the type of sample.

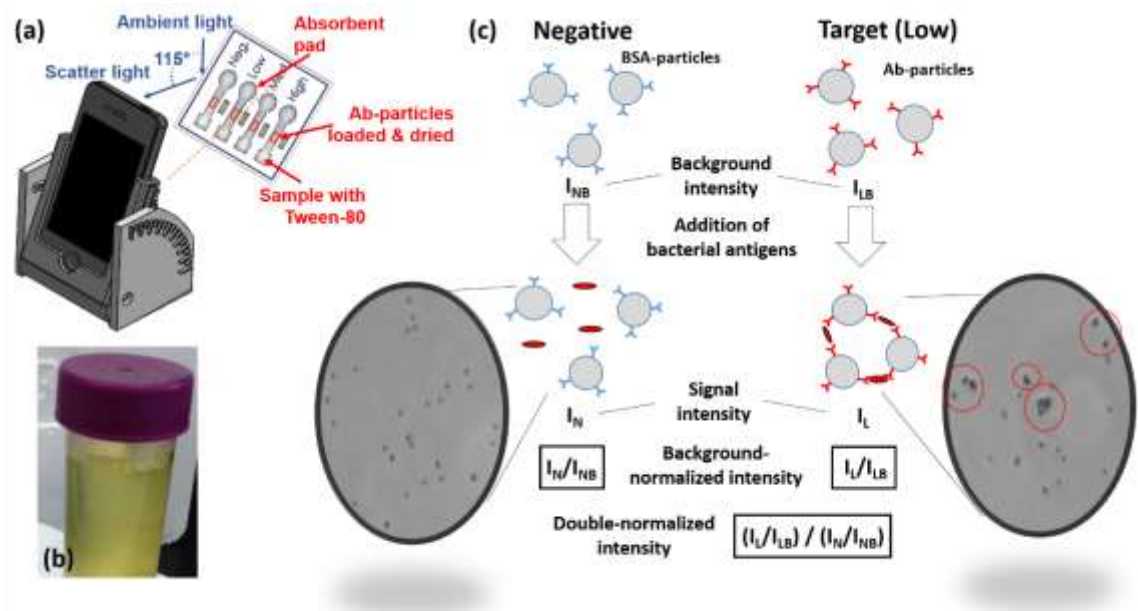


Figure B - 1

Antibody-conjugated particles (Ab-particles) are loaded on the μ PAD (a) in the loading site next to horizontal marker, located at the center of each channel. Sample with Tween 80 is loaded onto the inlet that flows through each channel towards the loading site. Target antigens in the sample induce immunoagglutination of Ab-particles. This causes an increase in light scattering, which is captured by a smartphone (a). Bacteria-spiked normal human urine is used with no pretreatment or purification (b). First step of light intensity normalization is shown by obtaining a background intensity (I_B) of the loading site of a paper channel, pre-loaded with the particles (c). After addition of bacteria-spiked urine, immunoagglutination occurs, which increases scatter intensity

(I_L for the low channel) compared to I_B (c). I_N and I_{NB} are not necessarily the same, since I_N was measured while the channel was still wet while I_{NB} was measured after the pre-loaded particles were dried. The double normalized intensity is defined as $(I_L / I_{LB}) / (I_N / I_{NB})$. Inset images with 400X objective shows no immunoagglutination for BSA-particles and immunoagglutination for Ab-particles (aggregates are outlined in red circles).

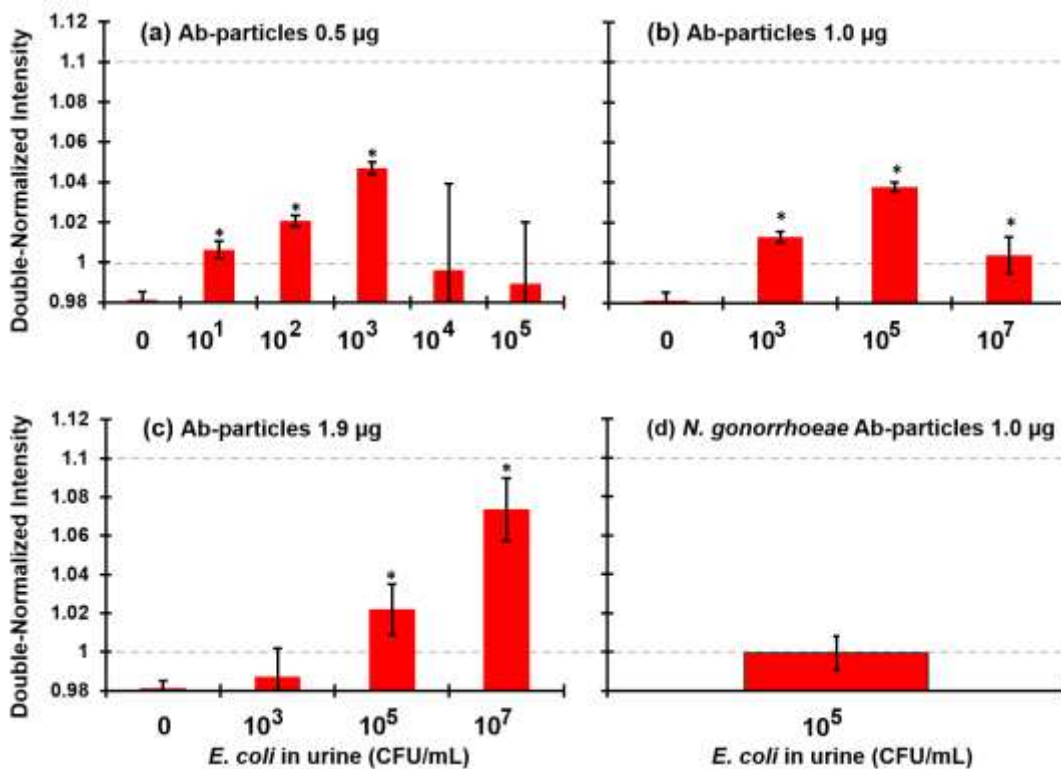


Figure B - 2

Results of paper microfluidic assay for *E. coli* in urine. See Figure 1C for double-normalization procedure. Each channel can be optimized for a specific range of *E. coli* concentration by adjusting the amount of Ab-particles loaded on a paper chip. By use of 0.5 µg of Ab-particles (a), the highest peak was obtained at 10^3 CFU/mL, with the lowest concentration passing the t-test (in comparison with the blank result) being 10 CFU/mL. By use of 1.0 µg of Ab-particles

(b), the highest peak was obtained at 10^5 CFU/mL. By use of 1.9 μg of Ab-particles (c), the highest peak was obtained at 10^7 CFU/mL. With 1.0 μg of anti-*N. gonorrhoeae* antibody particles to detect 10^5 CFU/mL *E. coli*, there was no change in signal intensity (d). * denotes $p < 0.05$.

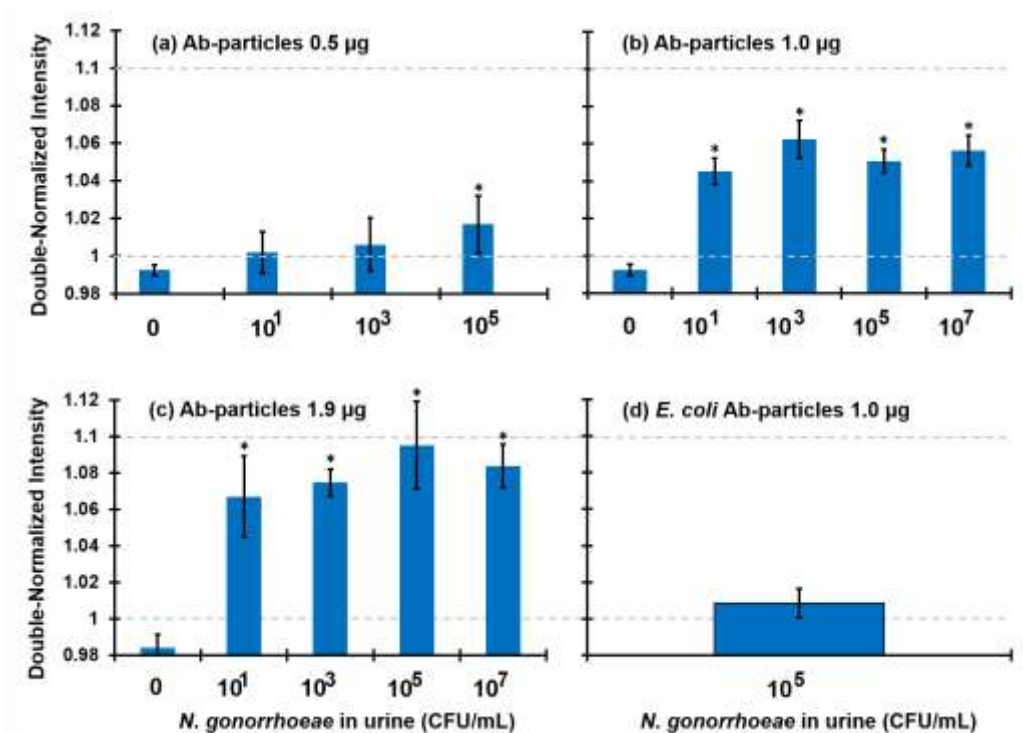


Figure B - 3

Results of paper microfluidic assay for *N. gonorrhoeae* in human urine. By use of 0.5 μg of Ab-particles (a), a linear increase was observed, but with large error bars. The lowest concentration passing the t-test (in comparison with the blank result) was 10^5 CFU/mL. With 1.0 μg (b), near-saturation of signals was observed starting from 10 CFU/mL. With 1.9 μg particles (c), significant signals were observed starting from 10 CFU/mL, with a linearly increasing trend. With 1.0 μg of anti-*E. coli* antibody particles to detect 10^5 CFU/mL *N. gonorrhoeae*, there was no change in signal intensity (d). * denotes $p < 0.05$.

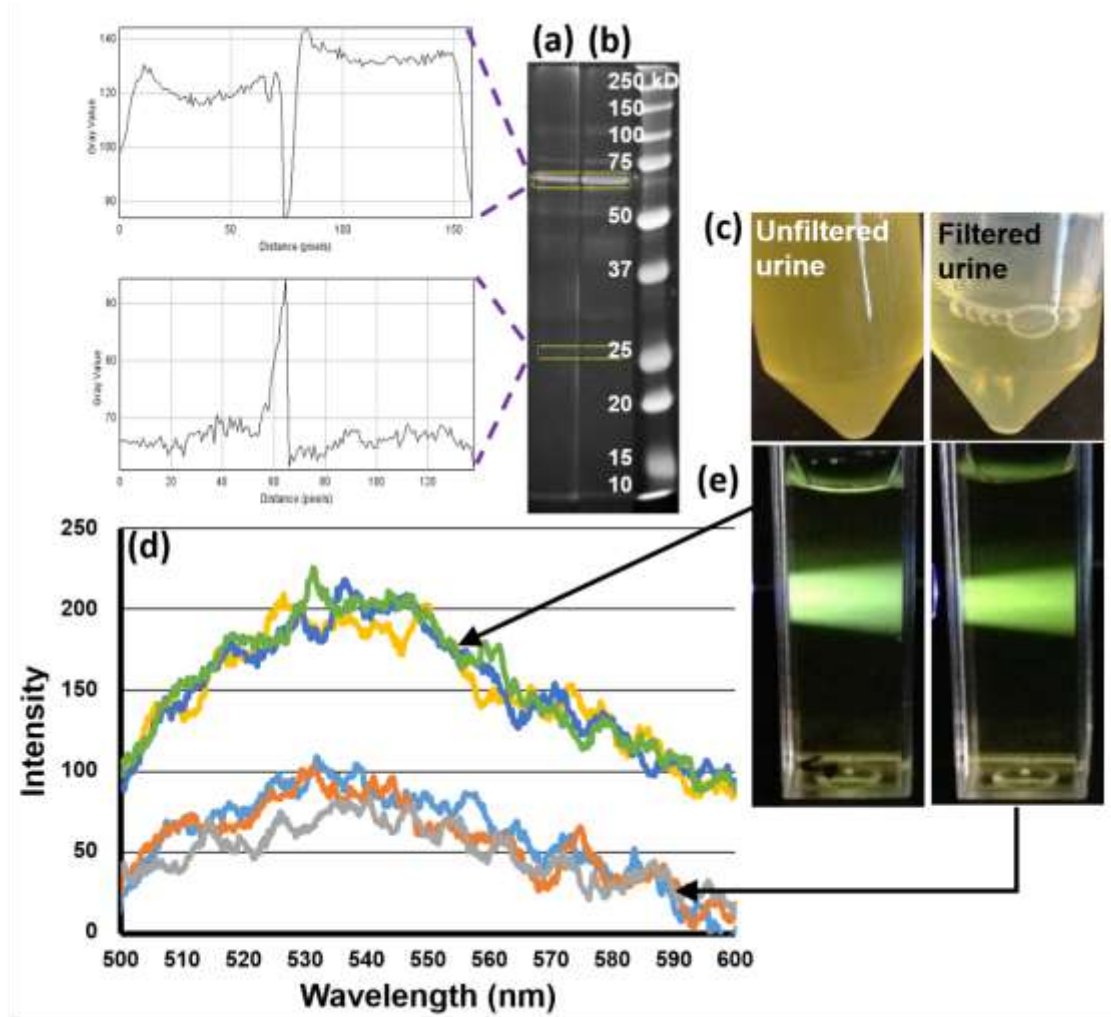


Figure B - 4

SDS-PAGE of unfiltered (a) and filtered (b) human urine. Pixel intensities of 67 kDa and 26 kDa bands are also shown to the left of (a) and (b). Representative images of unfiltered and filtered human urine samples are shown in (c), showing reduction of turbidity and yellow coloration. Emission spectra of unfiltered and filtered human urine (3 sets each) in response to 450 nm blue LED are shown in (d). Same unfiltered and filtered urine samples were placed in cuvettes and irradiated with 450 nm blue LED, generating visible green fluorescence (e).

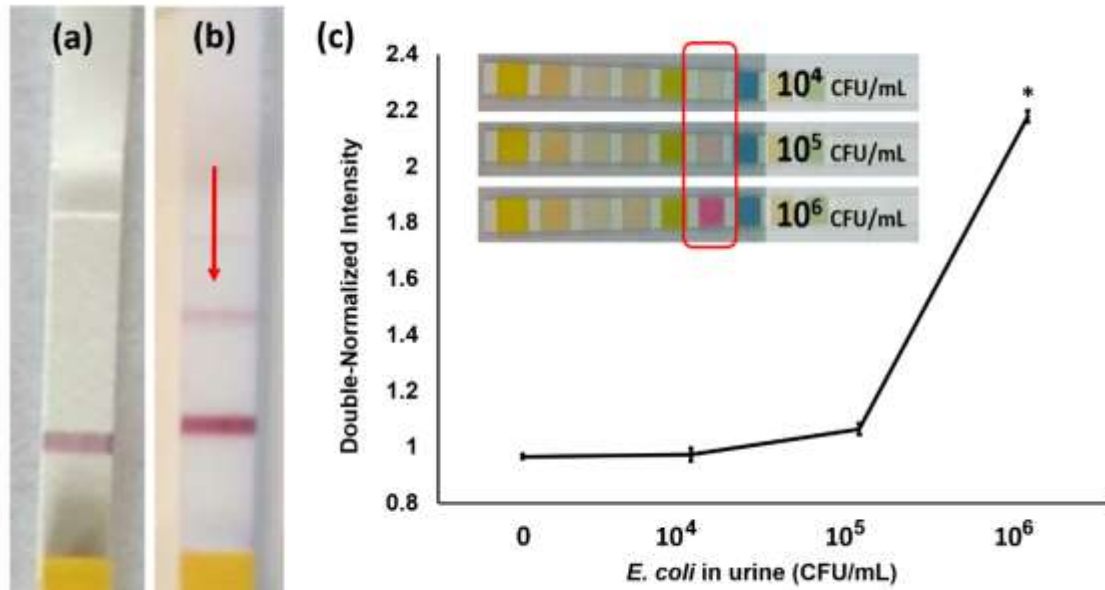
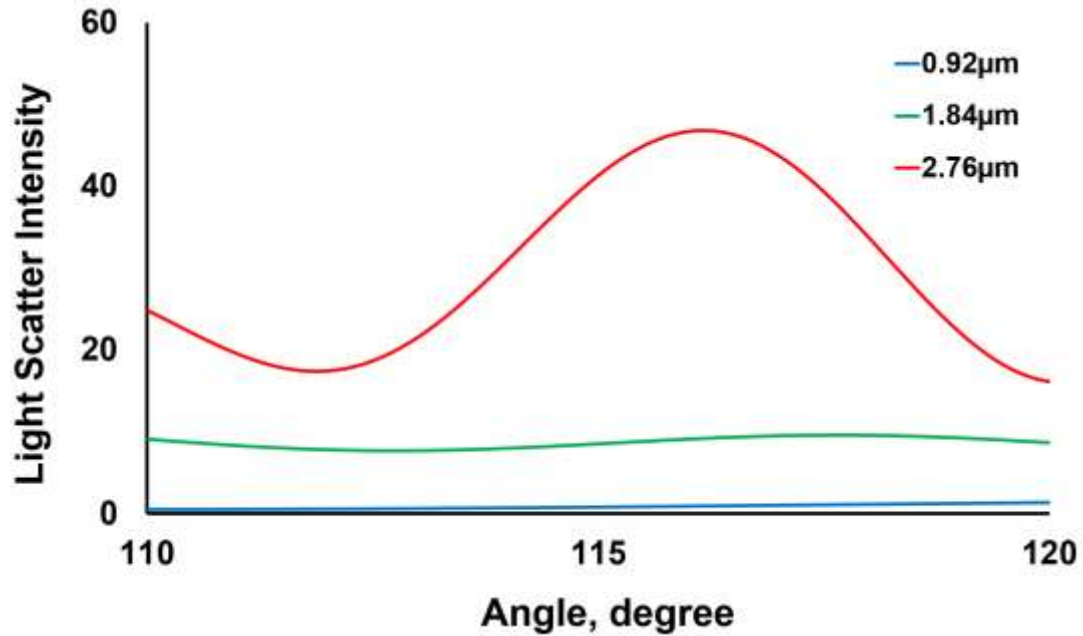


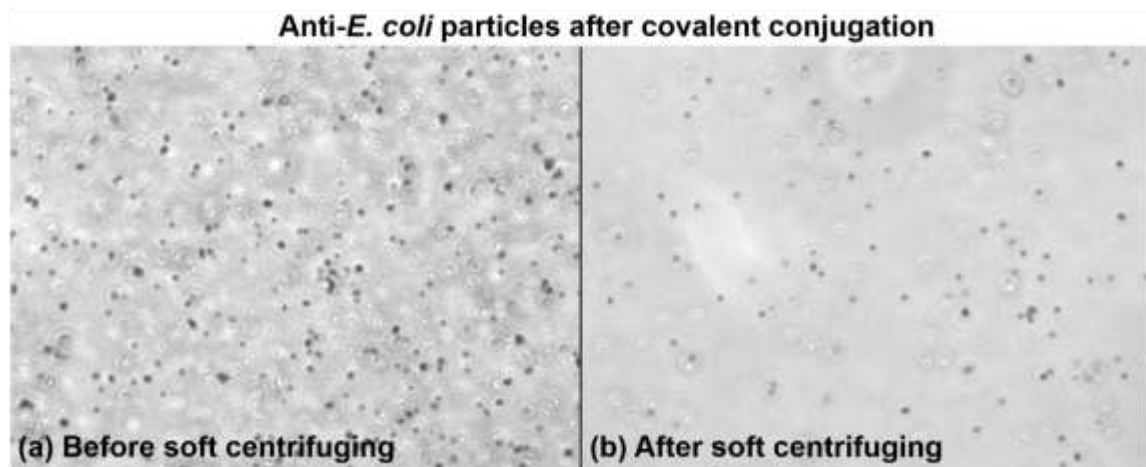
Figure B - 5

Results of commercial test strips. 20 μ L urine sample with 10^5 CFU/mL *N. gonorrhoeae* resulted in no positive band with commercial gonorrhea rapid test strips (a). 20 μ L urine sample with 10^6 CFU/mL *N. gonorrhoeae* resulted in faint positive band (b). Commercial urinalysis test strips were used with urine samples with 10^4 , 10^5 , 10^6 CFU/mL *E. coli* (c). Analysis of color change intensity shows statistically significant change in signal from 10^6 CFU/mL. * denotes $p < 0.05$ of paired t-test.



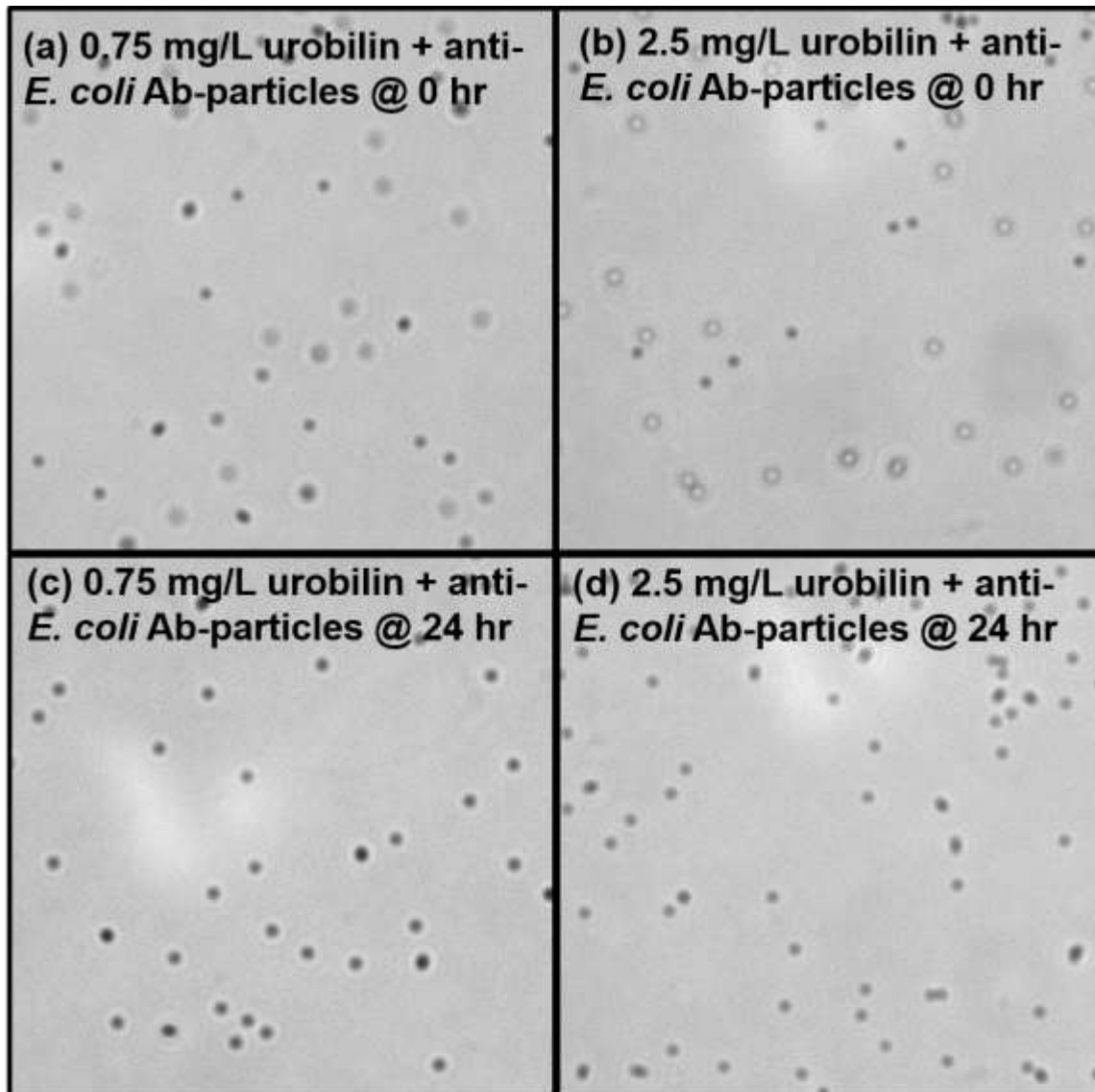
Supplementary Material B - 1

Mie scatter simulation shows maximum increase in light scatter at 115° upon immunoagglutination (0.92 μm for singlet particles, 1.84 and 2.76 μm for immunoagglutinated particles).



Supplementary Material B - 2

Effects of soft centrifugation on anti-*E. coli* antibody-particles. 400X light microscope image shows aggregated antibody-particles after conjugation (a). After soft centrifugation, most non-specifically aggregated particles are removed, resulting in majorly singlet (non-aggregated) particles (b).



Supplementary Material B - 3

Mixing of urobilin with anti-*E. coli* antibody particles. Right after mixing (a, b) and 24 hours later (c, d). 0.75 mg/L (a, c) and 2.5 mg/L (b, d) urobilin. In all cases, antibody-particles did not aggregate.

Appendix C

In situ, dual-mode monitoring of organ-on-a-chip with smartphone-based fluorescence microscope

Soohee Cho¹, Argel Islas-Robles^{2†}, Ariana M. Nicolini³, Terrence J. Monks^{2†}, Jeong-Yeol Yoon^{1,3*}

¹Department of Agricultural and Biosystems Engineering, ²Department of Pharmacology and Toxicology, and ³Biomedical Engineering Graduate Interdisciplinary Program, The University of Arizona, Tucson, Arizona 85721-0038, U.S.A.

[†]Present address: Eugene Applebaum College of Pharmacy and Health Sciences, Wayne State University, Detroit, Michigan 48201, U.S.A.

*Corresponding author at: Department of Agricultural and Biosystems Engineering, The University of Arizona, Tucson, Arizona 85721-0038, USA. Tel.: +1 520-621-3587; fax: +1-520-621-3963. URL: <http://biosensors.abe.arizona.edu>. E-mail address: jyoon@email.arizona.edu (J.-Y. Yoon).

Received 4 May 2016; received in revised form 29 June 2016; accepted 6 July 2016; available online 7 July 2016.

Biosensors & Bioelectronics **86**, 697-705 (2016)

© 2016 Elsevier B.V. – All rights reserved.

Abstract

The use of organ-on-a-chip (OOC) platforms enables improved simulation of the human kidney's response to nephrotoxic drugs. The standard method of analyzing nephrotoxicity from existing OOC has majorly consisted of invasively collecting samples (cells, lysates, media, etc.) from OOC. Such disruptive analyses potentiate contamination, disrupt the replicated *in vivo* environment, and require expertise to execute. Moreover, traditional analyses, including immunofluorescence microscopy, immunoblot, and microplate immunoassay are essentially not *in situ* and require substantial time, resources, and cost. In the present work, the incorporation of fluorescence nanoparticle immunocapture/immunoagglutination assay into an OOC enabled dual-mode monitoring of drug-induced nephrotoxicity *in situ*. A smartphone-based fluorescence microscope was fabricated as a handheld *in situ* monitoring device attached to an OOC. Both the presence of γ -glutamyl transpeptidase (GGT) on the apical brush-border membrane of 786-O proximal tubule cells within the OOC surface, and the release of GGT to the outflow of the OOC were evaluated with the fluorescence scatter detection of captured and immunoagglutinated anti-GGT conjugated nanoparticles. This dual-mode assay method provides a novel groundbreaking tool to enable the internal and external *in situ* monitoring of the OOC, which may be integrated into any existing OOCs to facilitate their subsequent analyses.

Keywords: Particle immunoagglutination; Kidney-on-a-chip; γ -glutamyl transpeptidase; 786-O cells; Smartphone microscope.

1. Introduction

Organ-on-a-chip (OOC) is defined as an integration of advanced 3D tissue engineered constructs with microfluidic network systems, i.e., lab-on-a-chip (LOC) (Bhise et al., 2014). Human cells are seeded and proliferated within the LOCs, providing a realistic replicate of the human organ. Such novel platforms improve preclinical testing of drugs, implants, biomedical devices, or stem cell therapies, due to their more realistic simulation of physiological function. OOCs have been developed to mimic the functions of various organs, including kidney, liver, brain, heart, skeletal muscle, and intestine (Ghaemmaghami et al., 2012; Esch et al., 2011). In OOCs, fluid flow generates mechanical forces that recapitulate the *in vivo* microenvironment experienced by cells, which cannot be accomplished by static 2D mammalian cell culture (Bhise et al., 2014). In this work, we are interested in developing kidney-on-a-chip to assess chemical-induced toxicity. Kidney is the main excretory organ that is exposed to drugs and xenobiotics. The epithelial cells of the renal proximal tubules in kidney are the most susceptible target for such drugs and xenobiotics (referred to as nephrotoxicants), due to their roles in the concentration of glomerular filtrate and their capacity for drug metabolism (Tiong et al., 2014). Specifically, previous studies of kidney-on-a-chip observed that proximal tubular cell (PTCs) functionality and morphology are improved under flow conditions (Jang et al., 2013), which is critical to emulate a response similar to the human kidney.

However, assessment of cell response during such OOC experiments remain tedious, disruptive, time-consuming, and lack real-time *in situ* analyses (Cai et al., 2015; Jang et al., 2013; Johnson et al., 2016; Maschmeyer et al., 2015). For example, a reported kidney-on-a-chip required immunofluorescence microscopy of the membrane within the OOC via cell fixation to monitor the growth of the epithelial cells (thus not *in situ*) and immunoblot of cells harvested

from the OOC post-treatment (Jang et al., 2013). Moreover, both methods require overnight analyses steps and invasive collection of the membrane and cells. Consequentially, the irreversible, permanent bonding of polydimethyl siloxane (PDMS)-based OOCs, the most common material used for not only OOCs but also bulk of LOCs, challenges the users in accessing, isolating, and processing cultured cells for certain preferred analysis including histology and electron microscopy (Huh et al., 2013). Thus, the users are subject to destructive methods of subsequent analyses of cells, or may heavily rely on fluorescence microscopy after fixation and subsequent immunostaining (Huh et al., 2012; Huh et al., 2013; van der Meer et al., 2013; Maschmeyer et al., 2015; Johnson et al., 2016). In several studies, the secreted cellular products have been analyzed, but they generally lacked the required sensitivity due to the low cell count (~10,000 cells) and the dilution of such products upon continuous perfusion (Huh et al., 2013). Therefore, existing OOCs can be significantly improved by application of a highly sensitive, direct detection tool to assess cytotoxicity, e.g., immediate and *in situ* quantification of the changes in target cell/protein concentrations. It is also preferable to fabricate such a tool as simply and inexpensively as possible to ensure ready availability to the widest selection of researchers.

In order to demonstrate our *in situ*, dual-mode monitoring tool, we propose to prototype a simple OOC with the use of 3D printing and a common house-use cutter machine. We will use a 3D printed template for conventional soft lithography towards fabrication of PDMS-based OOC (Comina et al., 2014), as a simpler and faster alternative. Since 3D printing does not provide sufficient resolution required for promoting cellular adhesion on its surface, we will use a common house-use cutter machine to create the patterns on the inner channel surfaces of an OOC. Although a cutter machine has been previously utilized to “cut” specific channel layouts to

fabricate paper-based LOC devices (Fang et al., 2015; Fang et al., 2014), it has not yet been utilized to modify the surface topography of LOC or OOC devices. This technique can provide a simpler and affordable alternative for adding micro-scale structures to the 3D printed LOC or OOC devices. Such textural detail addition may improve cellular adhesion to the substrates of OOCs.

Most importantly, a non-invasive, *in situ* monitoring tool needs to be incorporated into OOC, which should be easy to use, affordable, and potentially handheld, yet provide accurate and specific assay results. With this goal in mind, we propose the use of a fluorescent nanoparticle immunocapture as well as immunoagglutination assay coupled to a smartphone-based fluorescence microscope. This method will ultimately reduce assay time, offer sufficient assay specificity, ease of fabrication and use, while drastically reducing costly analytical procedures for *in situ* monitoring of cytotoxicity on OOC. Renal proximal tubule derived cells (PTCs) express various PTC specific brush border enzymes, such as γ -glutamyl transpeptidase (GGT), a protein that catalyzes the first step in the metabolism of glutathione (GSH) and GSH conjugates (Tiong et al., 2014). In response to PTC toxicants, the brush border membrane frequently sheds, releasing GGT into the tubular lumen, providing a desired target for detection of cytotoxicity. The use of nanoparticle immunocapture/immunoagglutination for *in situ* monitoring can be incorporated into any existing OOC system by altering the antibody to any given target. Thus, researchers will benefit greatly by improving their OOC analysis techniques. Our report represents the first demonstration of incorporating particle immunocapture/immunoagglutination assays to OOC systems.

Our group has quantified the concentration of bacteria by evaluating the angle-specific Mie scatter signal from immunoagglutinated polystyrene particles (You et al., 2011; Fronczek et

al., 2013; Park et al., 2013; Cho et al., 2015). Using smartphone-based optical detection, *Escherichia coli* and *Neisseria gonorrhoeae* were sensitively and specifically detected from undiluted human urine, a complicated bodily fluid (Cho et al., 2015). Particle concentration was optimized to detect a varying range of pathogen concentration. Our group has also previously constructed a 3D printed smartphone-based fluorescence microscope for the end-point quantification of PCR products (Angus et al., 2015). As emphasized, existing OOCs and LOCs would benefit greatly from a versatile analysis method that is noninvasive to the device and its content. With the intent of performing analysis on-chip, many approaches have been developed, including electrochemical electrodes, optical sensors, label-free detection of molecules, field-effect transistor sensors, and micro-cantilevers (Sung et al., 2013). One such proof-of-concept study was a portable fluorescence optical detection system to analyze the dynamics of cell viability (Choi et al., 2010). However, the detailed optical system is quite technical and a static 3D culture was fluorescently dyed, which would limit the scope of its application. Cells ideally need to be exposed under flow, especially when studying the cytotoxic response of cells that line directional flow with fluid-filled compartments, which is a similar microenvironment as human tissue.

In the current work, we predicted that the anti-GGT conjugated nanoparticles would be immunoagglutinated upon binding with the GGT either specifically released from the damaged PTCs within the OOC, or captured on the membrane fragments also released from the brush border membrane of PTCs (Fig. 1). Both behaviors can be monitored *in situ* through the use of fluorescent nanoparticles and subsequent detection via a smartphone-based fluorescence microscope. The method provides a novel groundbreaking tool, enabling *in situ*, dual-mode monitoring of the internal and external compartments of the OOC, and which may be integrated

into any existing OOCs to facilitate analyses. This dual-mode of detection, i.e., nanoparticle immunoagglutination and particle capture, has not been previously demonstrated, which is particularly suited for OOC experiments in monitoring both membrane expression and subsequent release of protein products, without the need for collecting, fixing, and/or staining the cells.

2. Materials and Method

2.1 OOC Fabrication

PDMS base and curing agent (Fisher Scientific; Pittsburgh, PA, USA) were combined at 10:1 ratio, and poured over the 3D-printed templates (3.5 mm x 25 mm x 1 mm) adhered to glass Petri dishes (100 mm x 1 mm). The resulting PDMS replicas were separated from the mold, the inlet and outlet holes were made using a 1 mm biopsy punch (Miltex, Inc.; York, PA, USA), and they were bonded to the bottom substrate (microscope glass slide; SPI Supplies; West Chester, PA, USA). The bottom substrate was etched with 400 μm deep line etchings with a Cricut Explore One™ (Provo Craft & Novelty, Inc.; Spanish Fork, Utah, USA). Three layers were patterned onto glass in the following order: straight lines with 20 mm length x 5 mm height with 1 mm spacing in between, zigzag patterns of 20 mm x 10 mm with 15° lines, and zigzag patterns rotated 180° and shifted by 1 mm.

2.2 Antibody Conjugation to Particles

Rabbit polyclonal antibody to γ -glutamyl transpeptidase (anti-GGT; catalog number ab175384, Abcam, Inc.; Cambridge, MA, USA) was used for GGT detection. Bovine serum albumin (BSA; Sigma-Aldrich; St. Louis, MO, USA) was used to generate negative control

signals with GGT-positive cell cultures. Anti-GGT and BSA were covalently conjugated to highly carboxylated, yellow-green, 500-nm diameter, polystyrene fluorescent particles (Masphere, Inc.; Pasadena, CA, USA). The fluorescence characteristics of these particles were reported by the vendor (Magsphere, Inc.) as 480 nm excitation and 510 nm emission. Prior to antibody and BSA conjugation to fluorescent polystyrene particles, particles were centrifuged and pre-washed with deionized water to remove surfactants from the stock solution as received from the vendor. Anti-GGT antibodies and BSA were conjugated to polystyrene particles following the protocol described in Cho et al. (2015).

2.3 Cell Culture and Seeding on OOC

Renal adenocarcinoma cell cultures (786-O; catalog number CRL-1932, ATCC; Manassas, VA, USA) were grown in Roswell Park Memorial Institute medium (RPMI) with L-glutamine (catalog number MT10040CV, Fisher Scientific) supplemented with 10% (v/v) fetal bovine serum (FBS; catalog number 10438018, Fisher Scientific). Cells were cultured at 37°C (HERAcell 150i; Cambridge Scientific; Watertown, MA, USA) in 5% CO₂ until 90% confluent.

After reaching ~90% confluency, 786-O cells were passaged following standard procedures (Abcam, 2015). Cells were resuspended at $4.5\text{-}5 \times 10^5$ cells/mL from which 100 μ L aliquots were seeded into each OOC, and incubated in static culture for 24 h. The OOC was subsequently placed in a biosafety cabinet. Polyethylene tubing (Braintree Scientific, Inc.; Braintree, MA, USA) with inner diameter (ID) = 0.381 mm and outer diameter (OD) = 1.092 mm was used to connect the inlet(s)/outlet to 27 gauge needle tips (ID = 0.229 mm and OD = 0.406 mm; Jensen Global; Santa Barbara, CA, USA). Syringes (1 mL; BD, Franklin Lakes, NJ,

USA) were connected and positioned on a microfluidic dual syringe pump (New Era Pump Systems, Inc.; Farmingdale, NY, USA).

2.4 Static Assays

Static immunoagglutination assays were performed *ex situ*, i.e., not on OOC, using 786-O lysates, prepared by seeding 60% confluent cells onto 6 cm dishes (Fisher Scientific) for 24 h, 72 h, and 144 h (i.e., until 90-100% confluent). Dishes were washed once with cold DPBS, followed by adding 300 μ L of lysis buffer. Anti-GGT particles or BSA particles were incubated with lysate solutions for 2 h. Static immunoagglutination assay was then performed with a scratched 786-O culture. 786-O cells were cultured and scratched to simulate brush border damage and GGT release by a nephrotoxicant. Microscopic videos of the fluorescent anti-GGT particles and BSA particles were acquired. These assay results were compared with the static GGT activity assay, following the method described by Silber et al. (1986), which measures the rate at which the substrate analog γ -glutamyl-*p*-nitroanilide (GPNA) is cleaved to form *p*-nitroaniline detected spectrophotometrically at 405 nm in a microplate spectrophotometer (Spectramax M2; Molecular Devices; Sunnyvale, CA, USA). In addition, 786-O cell viability assays were conducted on a microplate well, by measuring the optical transmission at 600 nm, with known nephrotoxicant (cisplatin) and non-nephrotoxicant (glycine). Details of all static assays can be found in Supplementary Material 1 – Static Assays.

2.5 Immunoagglutination Assay of the Outflow Solutions from the OOC

Fluorescence light scatter intensities were evaluated on a glass slide (MP Biomedicals; Santa Ana, CA, USA) for the samples (50 μ L) collected from the OOC outlet. Spectral

measurements were made using a reflection probe and a pair of optical fibers (R400-7-UV-VIS; Ocean Optics; Dunedin, FL, USA). The 480 nm blue LED irradiated the top of a droplet perpendicularly through the core fiber of a reflection probe, while the backscattered fluorescence signals were collected through the shell-side bundle of fibers of a reflection probe, which was connected to a miniature spectrometer (USB4000, Ocean Optics) via accompanying software (OceanView; Ocean Optics). Fluorescence of particles was measured at their emission maximum, 515 nm (green). The fluorescence intensities were normalized to those of the BSA particles in the same outflow solutions, or those of the anti-GGT particles in the absence of cells (only DPBS). A normalized intensity value of 1 represented the same fluorescence intensity as that of a normalization reference; an intensity <1 represents the loss of particles, and an intensity >1 represents an increase in fluorescence intensity and evidence of immunoagglutination.

2.6 OOC Immunoagglutination Assay with and without Toxicant

After 24 h incubation, 786-O cells were washed with DPBS, fixed with 4% paraformaldehyde solution (Affymetrix; Cleveland, OH, USA) for 10 min, and then washed with DPBS. A straight-channel OOC (for the assays without toxicant) or a Y-channel OOC (for the assays with toxicant) was used to perform the immunoagglutination assays (using optical fibers and a miniature spectrometer). Cisplatin (known nephrotoxicant) and glycine (known non-nephrotoxicant) were used, at 0, 1, 3 or 5 mM concentrations. Particles in DPBS (1:8 ratio) were passed through a syringe pump at a flow rate of 500 $\mu\text{L}/\text{h}$ (without toxicant) or 190 $\mu\text{L}/\text{h}$ (with toxicant – lower flow rate was necessary due to the tear in cell monolayer caused by toxicant) for 30 min. For the Y-channel OOC, one inlet was used for toxicant addition while the other for anti-GGT particles. For post-immunoagglutination assays on the OOC, cells were washed once with

DPBS for 30 min, and the outflow containing diluted particles were collected into 2 mL tubes (USA Scientific; Ocala, FL, USA). The 786-O cells within the OOC were then fixed with 4% paraformaldehyde solution for 15 min, washed twice with DPBS (500 or 190 $\mu\text{L}/\text{h}$), then stored in DPBS with 0.05% Tween 20 (DPBST; Fisher Scientific). The outflow was collected until the initial DPBS was fully washed away. Assays were repeated with varying concentrations of compounds (glycine and cisplatin), each time using new OOC, under dark conditions to prevent photobleaching of fluorescent particles.

2.7 Fabrication of Smartphone-based Fluorescence Microscope

The smartphone-based fluorescence microscope attachment was designed on SolidWorks software (Dassault Systèmes, SolidWorks Corporation; Waltham, MA, USA) and fabricated using a Dimension uPrint Rapid Prototyping Device (Stratasys, Inc.; Eden Prairie, MN, USA) using acrylonitrile butadiene styrene (ABS) material. Attachment consisted of three white LEDs (Edmund Optics; Barrington, NJ, USA), an objective lens (catalog number CAS100, Thor Labs; Newton, NJ, USA), 480 \pm 10 nm bandpass filter for the light source (catalog number 43-115, Edmund Optics) and 500 nm longpass filter (catalog number GG-495, Edmund Optics) for the smartphone camera. Light sources were powered by two 3 V button batteries (CR2032, Energizer; St. Louis, MO, USA). The smartphone's digital camera (iPhone 5S, Apple, Inc.; Cupertino, CA, USA) functioned as a secondary objective lens as well as an image-capturing device (Fig. 2).

2.8 Smartphone-based *In Situ* Monitoring of On-Chip Expression

All images were collected from the rear glass view of the OOC, which enabled clear image acquisition. Under dark conditions, the OOCs were positioned 10 mm from the primary objective lens of the smartphone-based fluorescence microscope. Images were collected after locking exposure and focus on a blank OOC. With appropriate adjustments to reduce the random light scatter from etchings of blank OOC, images were collected from various OOCs in presence and absence of cisplatin and glycine. Images were analyzed using ImageJ (National Institute of Health; Bethesda, MD, USA) on a separate desktop computer, and split to red, green, and blue channel images. The green images were assessed to specifically measure the intensity of the green fluorescent signal. On ImageJ, circular areas from the center of the images were analyzed. The fluorescence of immunoagglutinated particles on cell surfaces was measured from these areas of interest. The measured green intensities from OOCs were normalized to the measured green intensity of the blank OOC to eliminate the random light scattering from the etchings within the OOC channel. A series of normalized intensity values were plotted against the concentrations of cisplatin and glycine.

2.9 Statistical Analysis

All reported p-values were obtained from two sample independent t tests of sample versus blank (i.e. BSA-particles or anti-GGT particles with 0 mM toxicant) performed by Stata/IC 12.0 (StataCorp LP, 2011) using $\alpha = 0.05$. Statistical analysis of normalized intensities from outflow solutions were performed comparing cisplatin and glycine per respective concentration.

3. Results

3.1 Static Immunoagglutination Assays of 786-O Lysates

Proximal tubule cells (PTCs) express GGTs on the apical brush border membrane, which typically shed in response to a nephrotoxic insult (Bhise et al., 2014). This shedding causes the release of, and increase in the amount of GGT in the media available for particle immunoagglutination. Initially, the GGT enzymatic activities from the static 786-O cell monolayer cultures, 24 h, 72 h, and 144 h after seeding, were evaluated by a standard colorimetric enzymatic assay (Silber et al., 1986). A value of 28.4, 35.7, and 44.3 U/L were obtained.

Subsequently, a standard curve was constructed for the immunoagglutination assay with 786-O lysates, with the normalized fluorescent scatter intensities plotted against the GGT enzymatic activities of 28.4, 35.7, and 44.3 U/L. All fluorescent scatter intensities were normalized to those of the anti-GGT particles in the 786-O lysates that were not incubated at all (thus no immunoagglutination). All data points were statistically different from the control (i.e., those that were not incubated), with a linear increase at $y = 0.0054x + 0.99$ ($R^2 = 0.97$) (Fig. 3a).

Next, immunoagglutination assays were repeated for the same 786-O lysates at a fixed GGT activity, 31.8 U/L, but this time using BSA conjugated particles in comparison with anti-GGT particles. The normalized intensity with BSA particles is very close to 1, which represents the same fluorescence intensity of the BSA particles with or without incubation (Fig. 3b). There is a statistically significant difference of the normalized intensity with BSA particles than with anti-GGT particles (Fig. 3b). Thus, BSA particles can be used as a good negative control in the presence of tissue culture media and other cellular contaminants.

Microscopic images of anti-GGT particles revealed large aggregates with increased fluorescence (Fig. 3c), whereas the equivalent BSA particles revealed primarily singlets, i.e. non-agglutinated (Fig. 3d). In addition, the majority of immunoagglutinated anti-GGT particles were identified on the cell surface, whereas the BSA particles did not bind to the apical cell surface.

3.2 OOC Assays in the Absence of Toxicant

After 24 h incubation of 786-O cells in the OOC under static flow conditions, immunoagglutination assays were conducted on the outflow from the OOC at 500 $\mu\text{L}/\text{h}$ for 30 min. Two single, straight channel OOCs were used in parallel to evaluate the immunoagglutination assays using anti-GGT particles in one channel, and BSA particles in the other, under identical conditions. All fluorescence scatter intensities were normalized to the experiments replicated with DPBS (normalization reference), with respective particle type (anti-GGT or BSA particles). Anti-GGT particles showed a 15% decrease in normalized intensity from the control (Fig. 4a), which correlates to a loss of particles in the outflow. Following the same protocol, BSA particles exhibited a slightly increased normalized intensity from the control (Fig. 4a). This slightly higher intensity may arise from the non-specific aggregation of BSA particles, under the long duration of assay time (1 h). Since there was a loss of signal in the outflow with anti-GGT particles, we suspect that the particles are bound to the cell surface and subsequently trapped within the OOC. This interpretation was confirmed with the fluorescence microscopic images of the chip surface showing greater and sharper fluorescence and the presence of particles on the chip surface (Fig. 4c). In contrast, the BSA particles appeared more diffused, and were not firmly attached to the chip surface (Fig. 4b), but remained discharged into the outflow.

3.3 Chemical-Induced Cytotoxicity Assays in OOC

Immunoagglutination assays for the outflow solutions from OOC were performed with the 24 h cultured 786-O cells incubated with either glycine or cisplatin. Fluorescence scatter intensities were normalized as described above with particles diluted in DPBS. The results followed the pattern observed in Supplementary Material 1 – Static Assays. At varying glycine concentration, the normalized intensities remained similar, at ~50% of the reference (DPBS) (Fig. 5), indicating that ~50% of anti-GGT particles remained bound to the 786-O cell surface within the OOC and that glycine had no effect on altering such GGT expression. In contrast, increasing concentrations of cisplatin, raised normalized intensities from 0.50 (no cisplatin), 0.63 (1 mM cisplatin), 1.43 (3 mM cisplatin), and 1.90 (5 mM cisplatin) (Fig. 5). In other words, it varied from the 50% loss of anti-GGT particles (no cisplatin) to the 90% increase by immunoagglutination (5 mM cisplatin). These results indicate that with increasing cisplatin concentration the anti-GGT particles no longer remain bound to the cell surface within the OOC and are immunoagglutinated with the GGTs shed into the outflow solutions. These results are consistent with the fact that 786-O cell viability decreases at increasing cisplatin concentrations (Supplementary Material 1 – Static Assays).

3.4 *In Situ* Monitoring with Smartphone-based Fluorescence Microscopy

A smartphone-based fluorescence microscope was used to capture images of the OOC channels *in situ*, to monitor treatment induced cytotoxicity. Normalized intensities were collected in the same manner as described above (normalized to the respective particles diluted in DPBS). Subsequent analysis revealed the extent of immunoagglutination between the anti-GGT particles

and the GGTs on the cell surface within the OOC. Smartphone-based *in situ* monitoring on OOC revealed no significant changes in normalized intensities at different glycine concentrations, and were similar to that in absence of glycine (0 mM) (Fig. 6a). This is consistent with the lack of toxicity of glycine. In contrast, 1 mM cisplatin enhanced the normalized intensity relative to the 0 mM control, a consequence of GGT release from the brush border membrane in response to a cytotoxicant. Higher concentrations of cisplatin (3 and 5 mM) resulted in a linearly decreasing trend (Fig. 6), which is similar to that observed in the static cell viability (Supplementary Material 1 – Static Assays) and OOC assays (Fig. 4). Overtly cytotoxic concentrations of cisplatin causes cell death and cell detachment from the OOC surface in a manner equivalent to physiological anoikis, resulting in reduced amounts of anti-GGT particles bound to the chip surface and a decrease in normalized intensities. These findings are also consistent with the increased normalized intensities observed from the OOC outflow under high cisplatin concentrations (Fig. 5).

In situ images acquired by the smartphone-based fluorescence microscope from the surface of the OOC are shown in Fig. 6b, and revealed that at 0 mM glycine or cisplatin no significant fluorescence was observed. However, significant fluorescence was observed at 5 mM glycine, perhaps explaining the larger error bar for 5 mM glycine in Fig. 6a. Substantial fluorescence was observed with 1 mM cisplatin, consistent with the data in Fig. 6a. Similarly, 5 mM cisplatin diminished fluorescence consistent with other data (Figs. 4 and 6a; Supplementary Material 1).

4. Discussion

786-O cell cultures exhibit markers of differentiation representative of renal proximal tubule cells (PTCs) (Chiatar et al., 2013). We confirmed the presence of GGT enzymatic activity in 786-O cell lysates from 24 h, 72 h, 144 h cultures (28.4, 35.7, and 44.3 U/L). A standard curve was constructed, which demonstrated an increase of statistically significant fluorescent scatter intensities with increasing GGT enzymatic activity (Fig. 3a). Existing studies show that the detection limit of 1 U/L GGT can be measured from human urine by following standard automatic biochemistry analyzer (Zhang et al., 2015). However, the values tested in this study (28.4 – 44.3 U/L) covered the normal range of GGT expression (Orlowski and Szeqczuk, 1962; Westhuyzen et al., 2003, Zhang et al., 2015), which our anti-GGT particles may indeed detect and monitor the changes in GGT enzymatic activity. Meanwhile, higher level of GGT expression is expected under nephrotoxic insult. A previous clinical study reported a significant contrast of urinary GGT concentration among patients without acute renal failure (40.3 U/L) versus patients with the condition (77 U/L; Westhuyzen et al., 2003). Ideally, the standard curve can be used to quantify the GGT expression in the collected outflow solution of a nephrotoxic-induced organ-on-a-chip in order to expedite early detection in lieu of measuring excreted GGT from urinary samples.

The static immunoagglutination assay revealed that anti-GGT particles and subsequent fluorescence scatter measurements could successfully detect the presence of GGT in these lysates. BSA particles served as an appropriate negative control since they do not immunoagglutinate in the presence of GGT. To compare the extent of immunoagglutination between BSA particles and anti-GGT particles, 786-O monolayers cultured for 24 h were scratched to induce shedding of brush border membrane proteins in a fashion similar to that seen

in response to nephrotoxicants. Incubation (2 h) of BSA particles with the pre-scratched 786-O monolayers resulted in the presence of primarily randomly drifting particles (Supplementary Video S1). In contrast, incubation (2 h) of the anti-GGT particles with the pre-scratched 786-O cell monolayers resulted primarily in fixed particles on the cell surface, as would be anticipated by the capturing of anti-GGT particles on the brush border membrane (Supplementary Video S2). Anti-GGT particles also bound to the scratched surface, probably due the presence of cell fragments that remain adhered to the glass surface. Normalization was performed with the particles diluted in lysate solution, and consisted primarily of singlets. This provided a precise normalization rather than utilizing a DPBS solution since the lysates themselves induce non-specific aggregation and thus contribute to the increase in scattering signal. (Later experiments used DPBS as a negative control since lysates were not used.) Under the flow conditions using an OOC (with no toxicant), the outflow was assayed for GGT using anti-GGT and BSA particles (as control). With BSA particles, a slight increase in normalized intensity was observed, resulting from minor, non-specific, aggregation due to the long assay time (1 h). With anti-GGT particles, a significant decrease in normalized intensity was observed since 786-O cells express GGT on their brush border membrane, which captures the anti-GGT particles within the OOC, reducing the amount of GGTs in the outflow.

When investigating chemical- and drug-induced nephrotoxicity under the flow conditions of the OOC, the analysis of outflow and the *in situ* monitoring by a smartphone-based fluorescence microscope offered a coupled-tool for validating the assay in two simultaneous ways. As a nephrotoxicant (cisplatin) circulated through the OOC, GGT release into the media from 786-O cells increases, with corresponding increases in immunoagglutination of the anti-GGT particles in the outflow. Thus, as nephrotoxicant concentrations increase, GGT availability

and subsequently normalized intensity increase in the outflow (see Fig. 5, inset). In contrast, *in situ* monitoring within the OOC revealed a complementary decrease in normalized intensity, due to the loss of cells at overt cytotoxicity (Fig. 6). The dynamic range of the system thus benefits from this inversely coupled assay approach, as intensity in the outflow increases, whilst the intensity within the OOC decreases.

In response to drug-induced nephrotoxicity, all static and OOC assays with glycine exhibited no significant changes, consistent with glycine being non-toxicant. In contrast, studies with cisplatin exhibited significant increases in signal in the outflow and a general decrease in signal within the OOC, as expected from a known nephrotoxicant. The use of glycine and cisplatin therefore confirms the specificity of the assays. It may be possible that glycine and cisplatin had some effects on particle stability and thus generating non-specific signal increase. Therefore, both anti-GGT and BSA particles were incubated with 5 mM glycine or 5 mM cisplatin, and no significant signal increase was observed (Supplementary Material 2 – Effect of Toxicant on Particle Stability).

5. Conclusion

No previous reports addressing the incorporation of particle immunoagglutination assays into the OOC have yet been published. Standard methods of analyzing kidney cell culture upon exposure to toxicants include cell viability assay, enzymatic assay of the released GGTs, and fluorescence immunostaining of the GGTs expressed on cell membranes (Wilmer et al., 2016). The results of our particle immunoagglutination assay matched very well to those of static cell viability assay (Supplementary Material 1 vs. Figure 6A – trends are almost identical) as well as the GGT enzymatic assay (Figure 3A showed excellent correlation with $R^2 = 0.9664$ between

immunoagglutination and GGT enzymatic assays). As for immunofluorescence staining, our fluorescent anti-GGT nanoparticles perform similarly to the fluorescent dyes of immunofluorescence staining, while they provided additional advantage of dual-mode monitoring of GGT. Since particle immunoagglutination assays and subsequent light scatter detection can serve as an essentially one-step, rinse-free assay with very low limits of detection (typically down to 10 pg proteins per mL sample) (You et al., 2011; Fronczek et al., 2013; Park et al., 2013; Cho et al., 2015), this method can serve as an easy-to-use and versatile monitoring tool for OOC. Additionally, the antibody-conjugated particles can be used for monitoring both the outflow and the on-chip target protein content in response to induced cytotoxicity, offering a coupled-tool for validating the assays in two simultaneous ways. Furthermore, the inverse relationship of the coupled assays significantly increases the overall dynamic range of the system. Such unique and advantageous tool can be used towards more complex OOCs, for example, those requiring co-culture of different cell types. Co-culture has widely been considered a necessary trait in reconstituting the true organ-level functionality. Our dual-mode detection enables efficient analysis *in situ*, while with conventional invasive methods there is a risk of cross-contamination and disruption of *in vivo* environment. We also demonstrated the application of a 3D printed template and a commercial cutter machine to provide a simple and affordable fabrication of OOC. Moreover, the versatility of the immunoagglutination method also facilitates the testing of any protein for which antibodies are available to target. The *in situ* monitoring of the extent of immunoagglutination within the OOC with a smartphone-based microscope, another very important aspect of this work, and to the best of our knowledge is novel. Not only does such a hand-held, compact, and feasible analytic device simplify the analytic monitoring within the OOC (and potentially other LOCs), but it can broaden research

capabilities for those who otherwise lack the resources. The fast growing smartphone market in the developing world has enabled their potential application for rapid diagnostics (Yetisen et al., 2013).

Literature survey on recent nephrotoxicity studies with biosensor emphasis revealed that electrochemical sensors have been majorly utilized. In addition, cell viability and/or proliferation has been unanimously evaluated in such work (Cai et al., 2014; Lei et al., 2014; Liu et al., 2013; Shih et al., 2013; Tran et al., 2013; Zan et al., 2013), which assessed only the presence/absence of cells, and did not concern the analysis of cellular response. Such methodologies may satisfy initial drug screening and cell viability assay (Lei et al., 2014; Shih et al., 2013; Tran et al., 2013), but will not be able to provide detailed insight regarding cellular response. Thus, the incorporation of our dual-mode, protein marker-specific nanoparticle immunoagglutination assay within organ-on-a-chip may greatly potentiate the emergence of biosensors towards detailed drug screening and the study of cellular responses. Future direction of our research may entail investigations on detection from multiple target presence (using monoclonal antibodies), use of other enzyme/protein markers, not limited to nephrotoxicity, and to collaborative opportunities to incorporate our novel analytic methodologies to existing OOC/LOC systems.

6. Acknowledgements

Funding for this research was provided by the pilot grant program of the Southwest Environmental Health Sciences Center (SWEHSC) at the University of Arizona, funded by U.S. National Institutes of Health (grant number P30ES006694). Soohye Cho acknowledges the fellowship support from the Graduate STEM Fellows in K-12 Education (GK-12) Program, funded by U.S. National Science Foundation (grant number 0947836).

7. References

- Abcam, 2015. Cell Culture Guidelines, Abcam, Inc., Cambridge. <http://www.abcam.com/ps/pdf/protocols/cell_culture.pdf> (accessed 26.10.2015).
- Angus, S.V., Cho, S., Harshman, D.K., Song, J.Y., Yoon, J.Y., 2015. *Biosens. Bioelectron.* 74, 360-368.
- Bhise, N.S., Ribas, J., Manoharan, V., Zhang, Y.S., Polini, A., Massa, S., Dokmeci, M.R., Khademhosseini, A., 2014. *J. Control. Release* 190, 82-93.
- Cai, H.-H., Pi, J., Lin, X., Li, B., Li, A., Yang, P.-H., Cai, J., 2015. *Biosens. Bioelectron.* 74, 165-169.
- Chiatar, S.S., Eze, O.P., Schoenfeld, A.R., 2013. *Cell Dev. Biol.* 2, 1-12.
- Cho, S., Park, T.S., Nahapetian, T.G., Yoon, J.Y., 2015. *Biosens. Bioelectron.* 74, 601-611.
- Choi, J.R., Sung, J.H., Shuler, M.L., Kim, D., 2010. *Optics Lett.* 35, 1374-1376.
- Comina, G., Suska, A., Filippini, D., 2014. *Lab Chip* 14, 424-430.
- Esch, M.B., Sung, J.H., Yang, J., Yu, C., Yu, J., March, J.C., Shuler, M.L., 2012. *Biomed. Microdev.* 14, 895-906.
- Fang, X., Guan, M., Kong, J., 2015. *RSC Adv.* 6, 64614-64616.
- Fang, X., Wei, S., Kong, J., 2014. *Lab Chip* 14, 911-915.
- Fronczek, C.F., You, D.J., Yoon, J.Y., 2013. *Biosens. Bioelectron.* 40, 342-349.
- Ghaemmaghami, A.M., Hancock, M.J., Harrington, H., Kaji, H., Khademhosseini, A., 2012. *Drug Discov. Today* 17: 173-181.
- Huh, D., Kim, H.J., Fraser, J.P., Shea, D.E., Khan, M., Bahinski, A., Hamilton, G.A., Ingber, D.E., 2013. *Nat. Protoc.* 8, 2135-2157.

Huh, D., Leslie, D.C., Matthews, B.D., Fraser, J.P., Jurek, S., Hamilton, G.A., Thorneloe, K.S., McAlexander, M.A., Ingber, D.E., 2012. *Sci. Transl. Med.* 4, 159ra147.

Jang, K.J., Mehr, A.P., Hamilton, G.A., McPartlin, L.A., Chung, S., Suh, K.Y., Ingber, D.E., 2013. *Integr. Biol.* 5, 1119-1129.

Johnson, B.N., Lancaster, K.Z., Hogue, I.B., Meng, F., Kong, Y.L., Enquist, L.W., McAlpine, M.C., 2016. *Lab Chip*, 16, 1393-1400.

Lei, K.F., Wu, M.-H., Hsu, C.-W., Chen, Y.-D., 2014. *Biosens. Bioelectron.* 51, 16-21.

Liu, J., Qin, Y., Li, D., Wang, T., Liu, Y., Wang, J., Wang, E., 2013. *Biosens. Bioelectron.* 41, 436-441.

Maschmeyer, I., Lorenz, A.K., Schimek, K., Hasenberg, T., Ramme, A.P., Hübner, J., Lidner, M., Drewell, C., Bauer, S., Thomas, A., Sambo, N.S., Sonntag, F., Lauster, R., Marx, U., 2015. *Lab Chip* 15, 2688-2699.

Orlowski, M. and Szeqczuk, A., 1962. *Clin. Chim. Acta* 7, 755-760.

Park, T.S., Li, W., McCracken, K.E., Yoon, J.Y., 2013. *Lab Chip* 13, 4832-4840.

Shih, S.C.C., Barbulovic-Nad, I., Yang, X., Fobel, R., Wheeler, A.R., 2013. *Biosens. Bioelectron.* 42, 314-320.

Silber, P.M., Gandolfi, A.J., Brendel, K., 1986. *Anal. Biochem.* 158, 68-71.

StataCorp LP, 2011. *Stata/IC 12.0* <<http://www.stata.com/>> (accessed 06.11.16).

Sung, J.H., Esch, M.B., Prot, J.M., Long, C.J., Smith, A., Hickman, J.J., Shuler, M.L., 2013. *Lab Chip* 13, 1201-1212.

Tiong, H.Y., Huang, P., Xiong, S., Li, Y., Vathsala, A., Zink, D., 2014. *Mol. Pharmaceut.* 11, 1933-1948.

Tran, T.B., Cho, S., Min, J., 2013. *Biosens. Bioelectron.* 50, 453-459.

- van der Meer, A.D., Orlova, V.V., ten Dijke, P., van den Berg, A., Mummery, C.L., 2013. *Lab Chip* 13, 3562-3568.
- Westhuyzen, J., Endre, Z.H., Reece, G., Reith, D.M., Saltssi, D., Morgan, T.J., 2003. *Nephrol. Dial. Transplant* 18, 543-551.
- Wilmer, M.J., Ng, C.P., Lanz, H.L., Vulto, P., Suter-Dick, L., Masereeuw, R., 2016. *Trends Biotechnol.* 34, 156-170.
- Yetisen, A.K., Akram, M.S., Lowe, C.R., 2013. *Lab Chip* 12, 2210-51.
- You, D.J., Geshell, K.J., Yoon, J.Y., 2011. *Biosens. Bioelectron.* 28, 399-406.
- Zan, X., Fang, Z., Wu, J., Xiao, F., Huo, F., Duan, H., 2013. *Biosens. Bioelectron.* 49, 71-78.
- Zhang, Y.-R., Wang, P., Liang, X.-X., Tan, C.S., Tan, J.-B., Wang, J., Huang, Q., Huang, R., Li, Z.-X., Chen, W.-C., Wu, S.-X., Ong, C.N., Yang, X.-F., Wu, Y.-N. 2015. *Int. J. Environ. Res. Public Health* 12, 11988-12001.

8. Figures

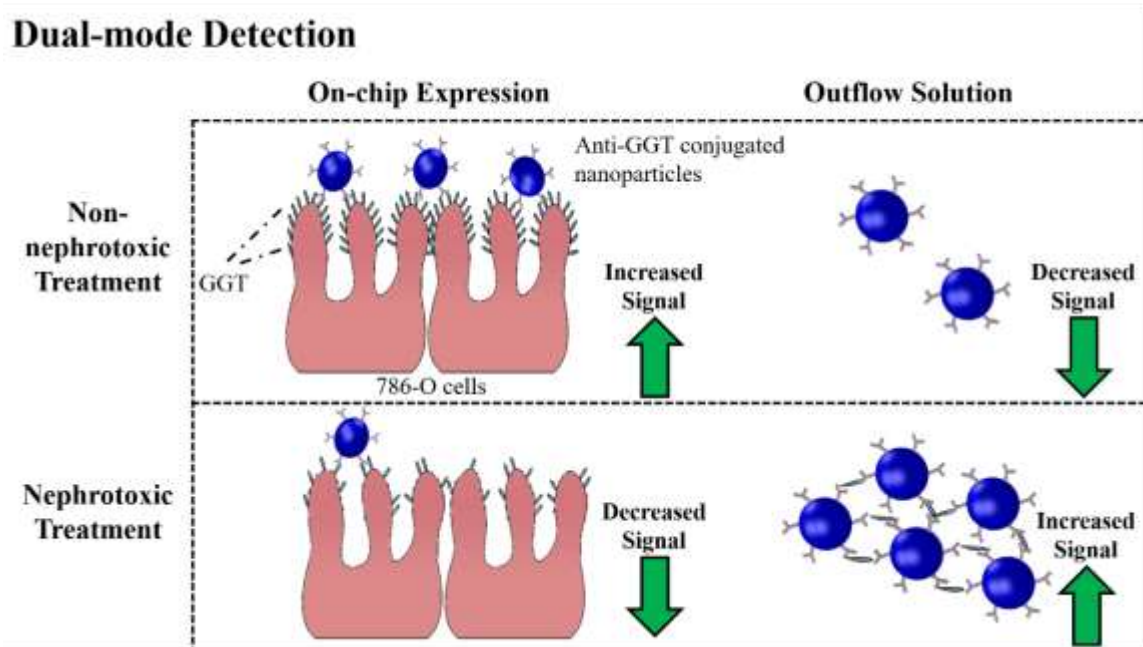


Figure C - 1

Schematic illustration of dual-mode detection. Anti-GGT particles bind to the GGTs expressed on the membrane of 786-O proximal tubule cells (PTCs), which can be identified *in situ* (i.e. on chip). With nephrotoxic treatment, such GGTs are released from the membrane and detected in the outflow solution.



Figure C - 2

In situ monitoring OOC device. A smartphone-based fluorescence microscope measured fluorescence scatter intensities from the Y-channel OOC. Red-dyed water was flow through the OOC for the purpose of visualization.

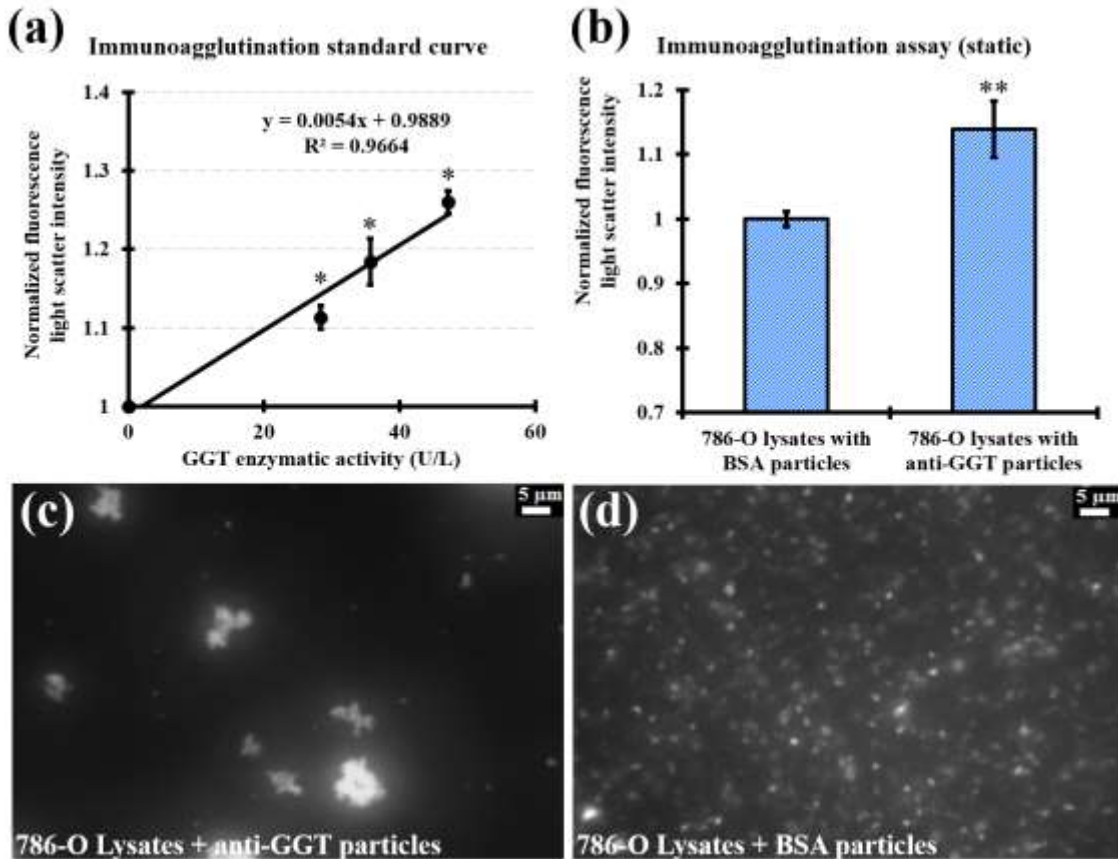


Figure C - 3

Standard curve of static immunoagglutination GGT assay from the 786-O lysates. A standard curve was constructed from a series of particle immunoagglutination GGT assays from the 786-O lysates under static conditions for 2 h, where x-axis is the enzymatic activities of GGT (a). Scatter intensities were normalized to those that have not been incubated (i.e., comprised of mostly singlets). The results with BSA conjugated particles are also shown in (b). Fluorescence

imaging on a light microscope showed aggregates and increased intensity from the 786-O lysates with anti-GGT particles (c), in contrast to majority of singlets from the 786-O lysates with BSA particles (d). * denotes $p < 0.05$ of two sample independent t-test; ** denotes $p < 0.0001$ of two sample independent t-test.

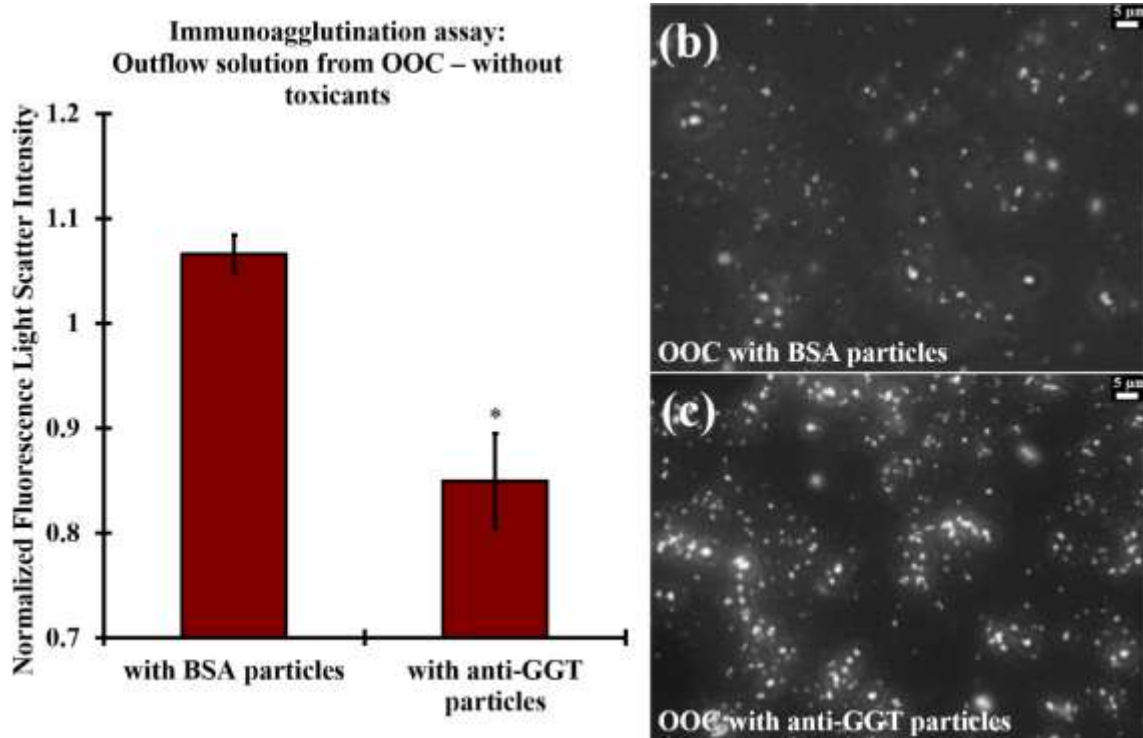


Figure C - 4

Particle immunoagglutination assay of the outflow solutions from OOC without toxicant. Compared to the normalized fluorescence scatter intensity with BSA particles, those with anti-GGT particles was lower by about 20% (a). Fluorescence scatter intensities of anti-GGT particles and BSA particles were normalized to the fluorescence scatter intensity of respective particles diluted in DPBS without incubation. Fluorescence imaging of the OOC channel using a light microscope showed greater presence of particles and fluorescence with anti-GGT particles (c), than BSA particles (b). * denotes $p < 0.05$ of two sample independent t-test.

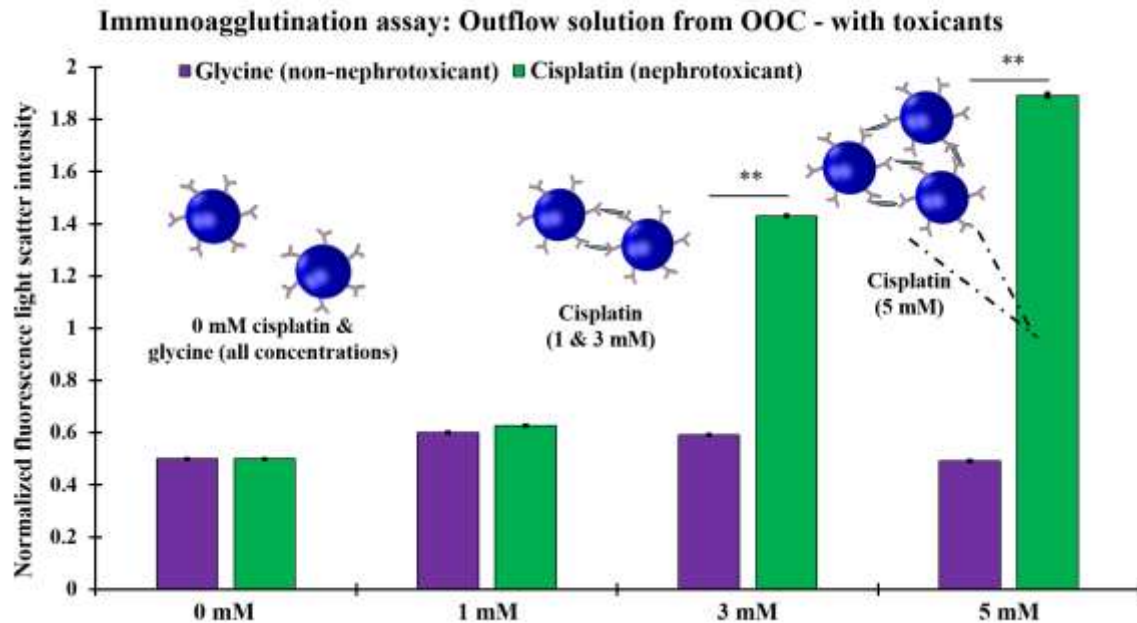


Figure C - 5

Particle immunoagglutination assay for the outflow solutions from OOC with toxicants. With increasing glycine concentration, the normalized intensities stayed the same around 0.5. With increasing cisplatin concentration, the normalized intensities increased. Inset images show the illustrations of anti-GGT particles with toxicant treatment. With no toxicant or glycine, GGT antigens are intact on the 786-O membranes, which renders anti-GGT particles to remain largely as singlets in the outflow solution. With increasing cisplatin concentrations, GGT antigens are released into the media and subsequently to the outflow solution as cell viability decreases. Anti-GGT particles more easily bind to free GGT antigens under flow condition, rather than binding to the disturbed membrane. With 5 mM cisplatin, hardly any cells are present within OOC. With increasing GGT antigens, extent of anti-GGT particle immunoagglutination increases, which contributes to the highest normalized intensities. ** denotes $p < 0.0001$ of two sample independent t-test.

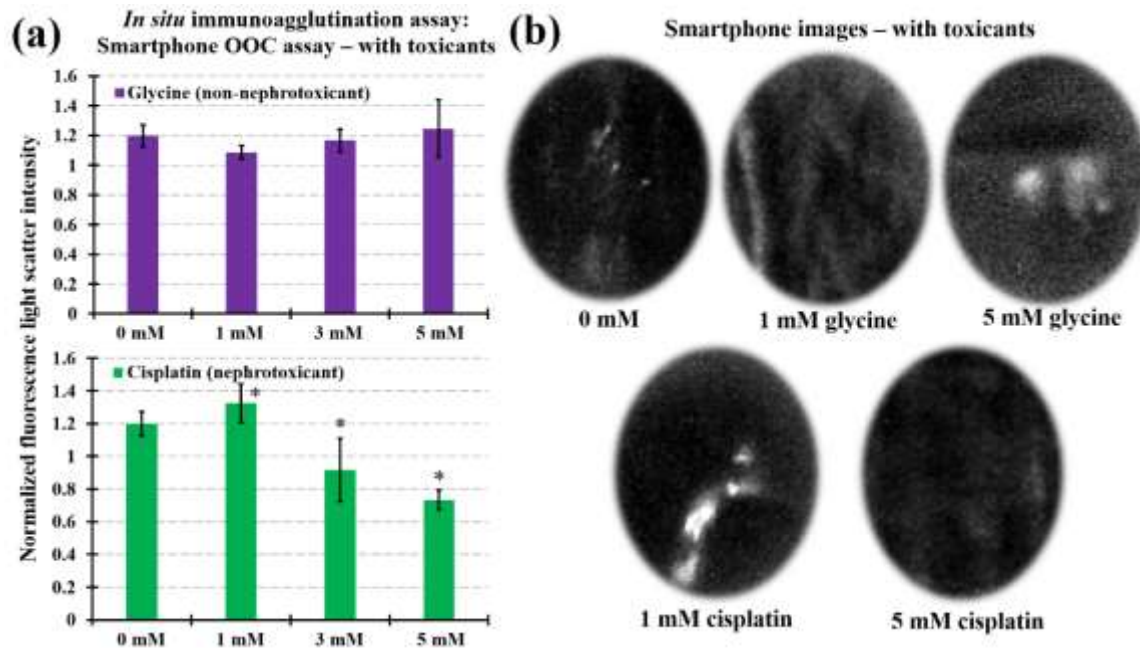


Figure C - 6

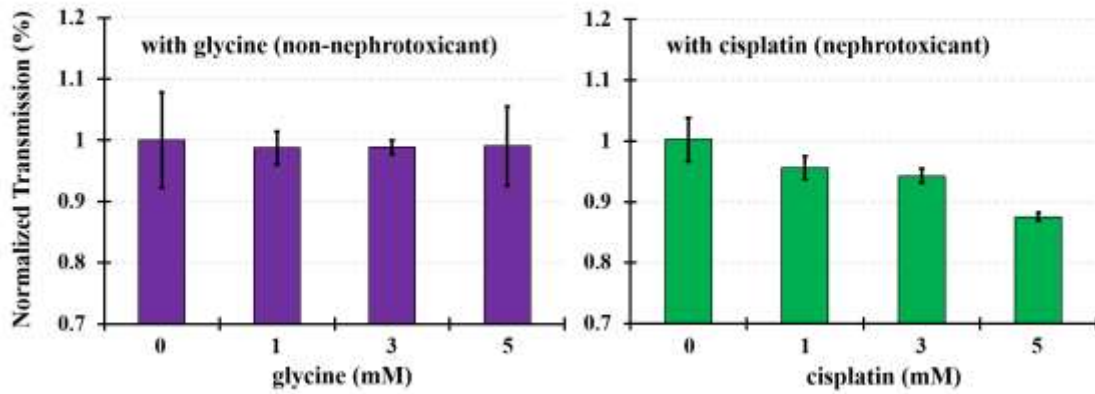
In situ assay results with smartphone-based fluorescence microscope. Images were taken after 1 h immunoagglutination assay in OOC with induced nephrotoxicity (glycine vs. cisplatin).

Normalized fluorescence scatter intensities, obtained from image analysis, are plotted against varying concentrations of glycine (non-nephrotoxicant) and cisplatin (PTC-specific nephrotoxicant) (a).

In situ images taken by the smartphone-based fluorescence microscope with 0 mM (absence of toxicant), 1 mM glycine, 5 mM glycine, 1 mM cisplatin, and 5 mM cisplatin

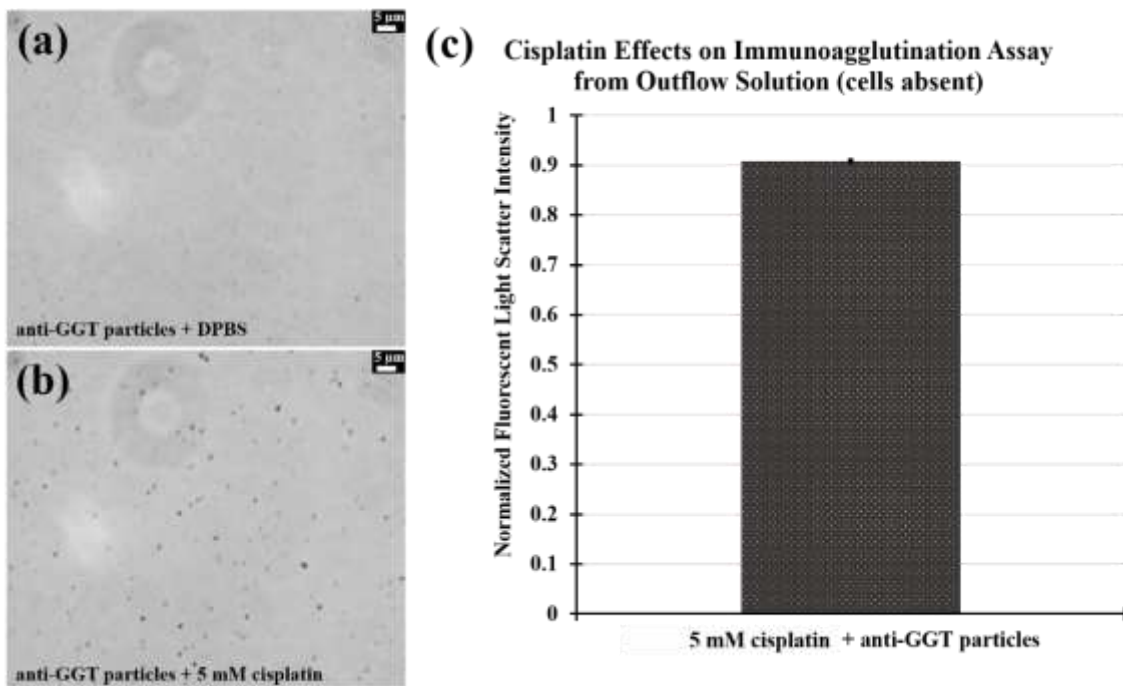
(b). Images are acquired with 5x magnification. * denotes $p < 0.05$ of two sample independent t-test.

786-O Cell Viability Assay



Supplementary Material C - 1

Static Assays.



Supplementary Material C - 2

Effect of Toxicant on Particle Stability.



Supplementary Video C - S 1

Video of static incubation of the BSA particles and the 786-O cells under scratched conditions. 786-O cells, after 24 h incubation, were scratched with a pipette tip to induce damage of brush border membrane. The well plate was slightly vibrated to demonstrate the floating BSA particles that were neither immunoagglutinated nor bound on the cells. Video is sped up 3x that of original.

Operation of video can be found at <https://doi.org/10.1016/j.bios.2016.07.015>.



Supplementary Video C - S 2

Video of static incubation between anti-GGT particles and cells under scratched conditions. 786-O cells, after 24 h incubation, were scratched with a pipette tip to induce shedding of brush border membrane. Video demonstrated that the majority of anti-GGT particles were fixed on the surface. Video is sped up 3x that of original.

Operation of video can be found at <https://doi.org/10.1016/j.bios.2016.07.015>.

Appendix D

Smartphone Detection of UV LED Enhanced Particle Immunoassay on Paper Microfluidics

Tu San Park^{1,†}, Soohye Cho^{1,†}, Tigran G. Nahapetian^{2,†}, and Jeong-Yeol Yoon^{1,2,*}

¹Department of Agricultural and Biosystems Engineering and ²Biomedical Engineering Graduate Interdisciplinary Program, The University of Arizona, Tucson, AZ 85721, USA

[†]These authors contributed equally to this work.

Corresponding Author:

Jeong-Yeol Yoon, The University of Arizona, 1177 E. 4th St., Rm. 403, Tucson, AZ 85721-0038, USA. E-mail: jyoon@email.arizona.edu

Received 2 December 2015; available online 18 March 2016; issue published 1 February 2017

SLAS Technology **22**, 7-12 (2017)

© 2017 Society for Laboratory Automation and Screening

Abstract

Use of a smartphone as an optical detector for paper microfluidic devices has recently gained substantial attention due to its simplicity, ease-of-use, and handheld capability. Utilization of a UV light source enhances the optical signal intensities, especially for the particle immunoagglutination assay that has typically utilized visible or ambient light. Such enhancement is essential for true assimilation of assays to field deployable and point-of-care applications by greatly reducing the effects by independent environmental factors. This work is the first demonstration of utilizing a UV LED (UVA) to enhance the Mie scatter signals from the particle immunoagglutination assay on the paper microfluidic devices, and subsequent smartphone detection. Smartphone's CMOS camera can recognize the UVA scatter from the paper microfluidic channels efficiently in its green channel. For *Escherichia coli* assay, the normalized signal intensities increased up to 50% from the negative signal with UV LED, compared to the 4-7% with ambient light. Detection limit was 10 CFU/mL. Similar results were obtained in the presence of 10% human whole blood.

Keywords: Light scatter; *E. coli*; whole blood; UVA; CMOS camera.

1. Introduction

Paper microfluidics has become a popular sensor platform due to its simplified patterning protocol,¹⁻⁴ smaller sample volume, and filtration capability.⁵ Many different chemical and biological assays have been demonstrated on paper microfluidics, such as detecting glucose,^{4,6} proteins,^{4,7,8} cholesterol,^{4,9} enzymes,¹⁰ antibodies,⁸ and so forth.^{11,12} Incorporating smartphone detection to paper microfluidics has also gained significant attention,^{5-8,13-16} towards field-deployable, low-cost, and easy-to-use chemical and biological assays. Detection of pathogenic bacteria from myriads of sample matrices, including field/waste water, food samples, stool/urine/blood from animals/humans would be the ultimate, yet challenging application of paper microfluidics assay with a smartphone.

A latex particle immunoagglutination assay can be used to achieve very sensitive detection of bacteria. It is a sensitive and robust method of detecting a target antigen by using antibody conjugated latex particles (typically submicron polystyrene particles) and subsequent Mie scatter detection. The antibody conjugated latex particles form aggregates in the presence of corresponding bacterial antigens and subsequently change the extent of angle-specific Mie scattering.¹⁷ Our group has recently demonstrated this assay on paper microfluidics with a smartphone, to detect *Escherichia coli* and *Salmonella* Typhimurium with the limit of detection of 10 CFU/mL.^{5,13,16} Optimizing the angle of the Mie scatter detection and minimizing the background scatter from paper fibers enabled high sensitivity and subsequently a very low limit of detection. However, the change of normalized signal intensity was only up to 5-7% over the negative control, partly due to its inherent limitation in distinguishing between the target and the non-target signals. Although the small error bars confirmed statistically significant sensitivity for bacterial detection, other independent factors in environmental conditions (such as ambient

lighting, temperature, humidity, paper porosity, etc.) can overshadow this small signal change. This situation applies to not only the particle immunoagglutination assay but also any type of chemical/biological optical assays, towards translating them into field-deployable and point-of-care applications.

One method of improving the signal change is the use of a shorter wavelength light source, such as UV LED (ultraviolet light emitting diode). UV light would provide higher energy to the particles and subsequently allow strong scatter than visible light ($E = hc/\lambda$, where E is the energy, h the Planck constant, c the speed of light, and λ the wavelength of light). Use of UV light towards handheld biosensing, however, requires caution as it can be dangerous to human skin and eyes. Therefore, longer wavelength UV such as UVA (315-400 nm) would be preferred over UVB (280-315 nm) or UVC (100-280 nm).

There exists one potential problem in utilizing UV LED towards smartphone based Mie scatter detection. Can a smartphone's camera recognize UV light? If so, which color channel should be used? Towards this end, the response characteristics of a smartphone camera (complementary metal oxide semiconductor or CMOS array) to UV irradiation was investigated. In addition, a Mie scatter simulation was conducted to confirm whether the UV light generates a greater change in scatter intensity upon immunoagglutination than visible light. A standard curve was also constructed for varying concentrations of *E. coli* using a paper microfluidic platform and smartphone detection, without using any optical filter. Finally, the *E. coli* assay was repeated with whole blood (in 10% dilution) to assess the enhanced scatter from UV LED, which has not been demonstrated previously. Thus, the utilization of a UV light source may be imperative for true assimilation of assays to field-deployable and point-of-care applications.

2. Materials and Method

Prior to the assays, Mie scatter simulations were conducted using MiePlot software¹⁸ to compare the scatter intensities from polystyrene (PS) particles under green (representative visible or ambient light) vs. UV light.

The paper microfluidic chips were fabricated using cellulose chromatography paper (GE Healthcare, Maidstone, Kent, UK) and SU-8 negative photoresist (MicroChem, Newton, MA, USA), following the same method as described in Park and Yoon⁵ and Park et al.¹³ Three keyhole-shaped channels were printed on each chip with 4.5 mm × 3.5 mm rectangular inlet, 2.5 mm wide × 11.5 mm long channel, and 4.5 mm × 5.5 mm oval-shaped adsorbent pad. The first channel was designated negative, the second low positive, and the third high positive.

Polyclonal antibody to *Escherichia coli* (anti-*E. coli*; Meridian Life Science, Memphis, TN, USA) conjugated PS particles (diameter = 920 nm; Magsphere, Pasadena, CA, USA) were prepared following the protocol described in Park and Yoon⁵ and Park et al.,¹³ and loaded to the center of each paper microfluidic channel (low and high positive channels), and subsequently dried. Bovine serum albumin (BSA) conjugated PS particles (0.5 µg) were loaded to the negative channel, to generate the negative signal without necessarily using a separate, blank control. A total of 0.5 µg of particles were loaded to each channel. Prior to loading to the paper channels, the antibody- or BSA-conjugated particles were soft-centrifuged¹⁶ to isolate unstable particles from the suspension.

E. coli K12 (Sigma-Aldrich, MO, USA) was cultured in brain heart infusion growth media (Remel, KS, USA) for 12 hours at 37°C. The fully grown bacteria culture (10⁸ CFU/mL; confirmed by MacConkey agar plating) was serially diluted in deionized water to make 10, 10², 10³, 10⁴, and 10⁵ CFU/mL samples. 1% Tween 80 (Sigma-Aldrich) was added to each serially

diluted *E. coli* solution at 1:10 ratio, which isolates the antigens from the viable colonies that can travel through the paper fibers. 7 μL of *E. coli* sample was loaded on the inlets of negative and positive channels.

The UV LEDs (275, 340, 365, 375, 385, and 395 nm; Seoul VioSys, Ansan, Republic of Korea) irradiated the paper microfluidic chip at an incident angle of 30 degrees to the chip surface and the smartphone took the image at 25 degrees from the chip surface (Fig. 1). These angles were optimized from a series of experiments that maximized the Mie scatter intensities from the PS particles and minimized the background scatter from paper fibers, using the procedure described in Park et al.¹³ The smartphone took two images before (background image) and after (signal image) the sample was loaded. The focus, exposure, and white balance were all locked to their optimal values to maximize the contrast and dynamic range, pre-determined from our previous work.¹⁶ The images were split into red (R), green (G), and blue (B) channels, and the rectangular crops were made for each detection zone (where the particles were loaded) using ImageJ (U.S. National Institutes of Health, Bethesda, MD, USA). In this manner, the scatter intensities were evaluated for each channel. For each channel, the scatter intensity from a signal image was divided by that from a background image to provide the normalized intensity ($I = I_s / I_b$), to compensate for the variations in chip fabrication, wetting and lighting conditions, etc. The normalized scatter intensity from a positive channel (i.e. with anti-*E. coli* particles) was compared with that from a negative channel (i.e. with BSA particles) and % scatter increase from a negative channel was evaluated, this time to compensate for the differences in the scattering characteristics and amount of the loaded particles. The whole experiment was repeated three times, each time using different samples and different paper microfluidic chips. Identical

experiments were performed using the *E. coli* samples spiked into 10% (v/v) diluted human whole blood (Interstate Blood Blank Inc., Memphis, TN, USA).

3. Results and Discussion

3.1 Smartphone Camera's Response to UV LED Irradiation

Six different UV LEDs (275, 340, 365, 375, 385, and 395 nm) were used to evaluate the response characteristics of smartphone's CMOS camera to UV irradiation. These UV LEDs were directly irradiated to the smartphone's camera (iPhone 4; Apple Inc., Cupertino, CA, USA) at a distance of 16 cm without using any optical filters. The average pixel intensities in red, green, and blue (RGB) channels were analyzed using ImageJ software. Figure 2 shows the average pixel intensities in red (R), green (G), and blue (B) channels upon UV LED irradiation. All RGB intensities with 275 and 340 nm UV LEDs were very low, while those with 365 nm UV LED were substantial. The red and blue intensities with longer wavelength UV LEDs (375, 385, and 395 nm) showed saturated values (i.e. close to 255), while the green intensities remained unsaturated, under normal camera operation with auto-exposure. The blue saturation can easily be explained with the UV LED wavelength's (375, 385, and 395 nm) proximity to the blue color (400-500 nm). The red saturation can also be explained with the response characteristics of human eye and subsequently most CMOS cameras to violet color (380-450 nm), to which both blue and red cone cells (and subsequently blue and red pixels) respond. Therefore, it can be concluded that all three color channels respond to UVA, specifically to the wavelengths longer than 365 nm.¹⁹ Green intensities can be particularly useful since red and blue pixel intensities are saturated under normal camera operation while green intensities are not. Among three choices (375, 385, and 395 nm), the 385 nm UV LED was selected for the remainder of this study.

3.2 Mie Scatter Simulation

Mie scatter simulation was conducted to estimate the increase in scatter intensity of the immunoagglutinated PS particles from the non-agglutinated, under UV light, in comparison with those under ambient light, i.e., previous work,^{5,13,16} where the green pixel intensities were proven to be the most sensitive. Simulation was conducted using the following parameters: (1) light source = 530 nm (green detection under ambient light) vs. 385 nm (UV LED); both unpolarized, (2) particle diameter = 920 nm for the non-agglutinated PS particles vs. 1840 nm for the immunoagglutinated particles, (3) particle size distribution = normal distribution with 5% standard deviation, (4) refractive indices = 1.60 for PS (polystyrene) and 1.33 for water (medium), and (5) scattering angle = 125° (refer to Fig. 1). As shown in Fig. 3, the scatter intensity (arbitrary unit) increased from 1.2 to 2.3 under 530 nm green light for the simulated immunoagglutination. A similar increase from 9.6 to 22.1 (arbitrary unit) was observed with 385 nm UV light, showing a marked enhancement over that with green light. Obviously, this signal enhancement is due to the higher energy inherent in shorter wavelength UV light than longer wavelength ambient light.

3.3 *E. coli* Assay

Using the 385 nm UV LED as a light source, particle immunoagglutination *E. coli* assays were conducted on the paper microfluidic chips, pre-loaded with anti-*E. coli* conjugated PS particles. Smartphone acquired the digital images of the paper microfluidic chips before and after the assays. Similar to the results shown in Fig. 2, both blue and red intensities from the detection zone of each microchannel were always saturated under the normal auto-exposure condition,

since the other parts of the paper microfluidic chips and the background (laboratory desk) were substantially dimmer than the particle-loaded area. A special smartphone application may be used to reduce the exposure time, in order to attenuate both blue and red intensities. However, such application is not necessary, since the green intensities from the detection zone provided unsaturated and detectable signal intensities.

Using this approach, a standard curve for *E. coli* detection was obtained, as shown in Fig. 4. Since each data point was normalized to that of the negative channel (loaded with BSA-conjugated particles) with the same *E. coli* sample, it was possible to evaluate the data for 0 CFU/mL with an error bar, which is not necessarily at 0%.¹⁶ The double-normalized intensities increased almost up to 50% for the 10^3 CFU/mL sample, followed by a decrease. This result indicates that the linear range of assay is three orders of magnitude for the given amount of antibody-conjugated particles, consistent with the previous work.^{13,16} While it is possible to shift this linear range to the higher range of concentration, for example, 10^3 - 10^5 CFU/mL or 10^5 - 10^7 CFU/mL, through increasing the amount of antibody-conjugated particles loaded to the paper channel, as previously demonstrated,¹⁶ it has already been demonstrated and is out of scope of this work. All data points from 10 to 10^4 CFU/mL were significantly different from that of 0 CFU/mL ($p < 0.05$), indicating the detection limit of 10 CFU/mL. This signal increase is approximately 10 times bigger than the previous work (4-7%), which used ambient light as a light source.^{5,13,16}

3.4 *E. coli* Assay with 10% human whole blood

The same experiments were repeated with the *E. coli* samples dissolved in 10% diluted human whole blood, which is a typical dilution used for many other immunoassays, including the

conventional microfluidic assay.²⁰ The paper microfluidic assays for the whole blood sample are known to be challenging due to the significant colorimetric disturbance from the blood components. This effect can particularly be worse for the particle immunoagglutination assay under ambient light, due to its inherently weak signals. Figure 5 shows the results, indicating successful assays. The double-normalized intensities increased up to 50% for the 10^2 CFU/mL sample, followed by a decrease. The reductions in the linear range (up to 10^2 CFU/mL vs. up to 10^3 CFU/mL), as well as the overall larger error bars, can be attributed to the presence of the blood components.

3.5 Macroscopic and SEM images of particle immunoagglutination on paper

Figure 6A shows the macroscopic, green channel images of the detection zone of each paper microfluidic channel with 0, 10, and 10^3 CFU/mL *E. coli* in DI water or 10% whole blood. The overall green pixel intensities increased with increasing *E. coli* concentration, which were used as input parameters for evaluating normalized intensities. In addition, the SEM images of anti-*E. coli* conjugated polystyrene particles on the central detection zone of each paper microfluidic channel were also shown in Fig. 6B, showing a substantial difference in the extent of agglutination between 0 and 10^3 CFU/mL *E. coli*. Small extent of aggregation with 0 CFU/mL *E. coli* can be attributed to the gold sputter coating and the vacuum conditions required for SEM imaging.

4. Conclusion

In this work, we demonstrated the significant enhancement of Mie scatter signals of particle immunoagglutination assays on paper microfluidic chips by use of UV LED, and that a

smartphone can recognize it efficiently in the green channel. Normalized signal intensities increased up to 50% for the *E. coli* assay, a 10-fold improvement from the same assay with ambient light. We were able to achieve a detection limit of 10 CFU/mL. The same experiments can be repeated for the *E. coli* assay in 10% human whole blood, which can be attributed to the stronger energy generated by the UV light source.

5. Acknowledgements

Mr. K. Serge Dogbevi and Ms. Jessica M. Mergener at the University of Arizona assisted the fabrication of paper microfluidic chips and preparation of reagents. Scanning electron microscopy was performed at the W. M. Keck Center in the University of Arizona. The authors also thank Dr. Daewoong “Dave” Suh and Dr. Kyujin Choi at Seoul VioSys for helpful discussion.

6. Declaration of Conflicting Interests

The authors declared no potential conflicts of interest with respect to the research, authorship, and/or publication of this article.

7. Funding

The authors disclosed receipt of the following financial support for the research, authorship, and/or publication of this article: This research was supported by Seoul VioSys, Ansan, Gyeonggi, Republic of Korea, and Richard A. Harvill graduate fellowship (awarded to Soohye Cho).

8. References

1. Cate, D. M.; Adkins, J. A.; Mettakoonpitak, J.; Henry, C. S. Recent developments in paper-based microfluidic devices. *Anal. Chem.* 2014, 87, 19-41.
2. Lisowski, P.; Zarzycki, P. K. Microfluidic paper-based analytical devices (μ PADs) and micro total analysis systems (μ TAS): Development, applications and future trends. *Chromatographia.* 2013, 76, 1201-1214.
3. Martinez, A. W.; Phillips, S. T.; Wiley, B. J.; Gupta, M.; Whitesides, G. M. FLASH: A rapid method for prototyping paper-based microfluidic devices. *Lab Chip* 2008, 8, 2146-2150.
4. Carrilho, E.; Martinez, A. W.; Whitesides, G. M. Understanding wax printing: A simple micropatterning process for paper-based microfluidics. *Anal. Chem.* 2009, 81, 7091-7095.
5. Park, T. S.; Yoon, J.-Y. Smartphone detection of *Escherichia coli* from field water samples on paper microfluidics. *IEEE Sens. J.* 2015, 15, 1902-1907.
6. Chun, H. J.; Park, Y. M.; Han, Y. D.; Jang, Y. H.; Yoon, H. C. Paper-based glucose biosensing system utilizing a smartphone as a signal reader. *BioChip J.* 2014, 8, 218-226.
7. Martinez, A. W.; Phillips, S. T.; Carrilho, E.; Thomas III, S. W.; Sindi, H.; Whitesides, G. M. Simple telemedicine for developing regions: Camera phones and paper-based microfluidic devices for real-time, off-site diagnosis. *Anal. Chem.* 2008, 80, 3699-3707.
8. Barbosa, A. I.; Gehlot, P.; Sidapra, K.; Edwards, A. D.; Reis, N. M. Portable smartphone quantitation of prostate specific antigen (PSA) in a fluoropolymer microfluidic device. *Biosens. Bioelectron.* 2015, 70, 5-14.
9. Nie, Z.; Deiss, F.; Liu, X.; Akbulut, O.; Whitesides, G. M. Integration of paper-based microfluidic devices with commercial electrochemical readers. *Lab Chip* 2010, 10, 3163-3169.

10. Pollock, N. R.; Rollan, J. P.; Kumar, S.; Beattie, P. D.; Jain, S.; Noubary, F.; Wong, V. L.; Pohlmann, R. A.; Ryan, U. S.; Whitesides, G. M. A paper-based multiplexed transaminase test for low-cost, point-of-care liver function testing. *Sci. Transl. Med.* 2012, 4, 152ra129.
11. Cheng, C.-M.; Martinez, A. W.; Gong, J.; Mace, C. R.; Phillips, S. T.; Carrilho, E.; Mirica, K. A.; Whitesides, G. M. Paper-based ELISA. *Angew. Chem., Int. Ed.* 2010, 122, 4881-4884.
12. Hsu, C.-K.; Huang, H.-Y.; Chen, W.-R.; Nishie, W.; Ujie, H.; Natsuga, K.; Fan, S.-T.; Wang, H.-K.; Lee, J. Y.-Y.; Tsai, W.-L.; Shimizu, H.; Cheng, C.-M. Paper-based ELISA for the detection of autoimmune antibodies in body fluid – The case of bullous pemphigoid. *Anal. Chem.* 2014, 86, 4605-4610.
13. Park, T. S.; Li, W.; McCracken, K. E.; Yoon, J.-Y. Smartphone quantifies Salmonella from paper microfluidics. *Lab Chip* 2013, 13, 4832-4840.
14. Park, T. S.; Baynes, C.; Cho, S.-I.; Yoon, J.-Y. Paper microfluidics for red wine tasting. *RSC Adv.*, 2014, 4, 24356-24362.
15. Fronczek, C. F.; Park, T. S.; Harshman, D. K.; Nicolini, A. M.; Yoon, J.-Y. Paper microfluidic extraction and direct smartphone-based identification of pathogenic nucleic acid from field and clinical samples. *RSC Adv.* 2014, 4, 11103-11110.
16. Cho, S.; Park, T. S.; Nahapetian, T. G.; Yoon, J.-Y. Smartphone-based μ PAD detection of urinary tract infection and gonorrhea. *Biosens. Bioelectron.* 2015, 74, 601-611.
17. van de Hulst, H. C. *Light Scattering by Small Particles*. Dover: Mineola, NY, 1981.
18. Laven, P. MiePlot v.4.2.11. 2013. <http://philiplaven.com>
19. Igoe, D.; Parisi, A. V. Evaluation of a smartphone sensor to broadband and narrowband ultraviolet A radiation. *Instrum. Sci. Technol.* 2014, 43, 283-289.

20. Stemple, C. C.; Angus, S. V.; Park, T. S.; Yoon, J.-Y. Smartphone-based optofluidic lab-on-a-chip for detecting pathogens from blood. *J. Lab. Automat.* 2014, *19*, 35-41.

9. Figures

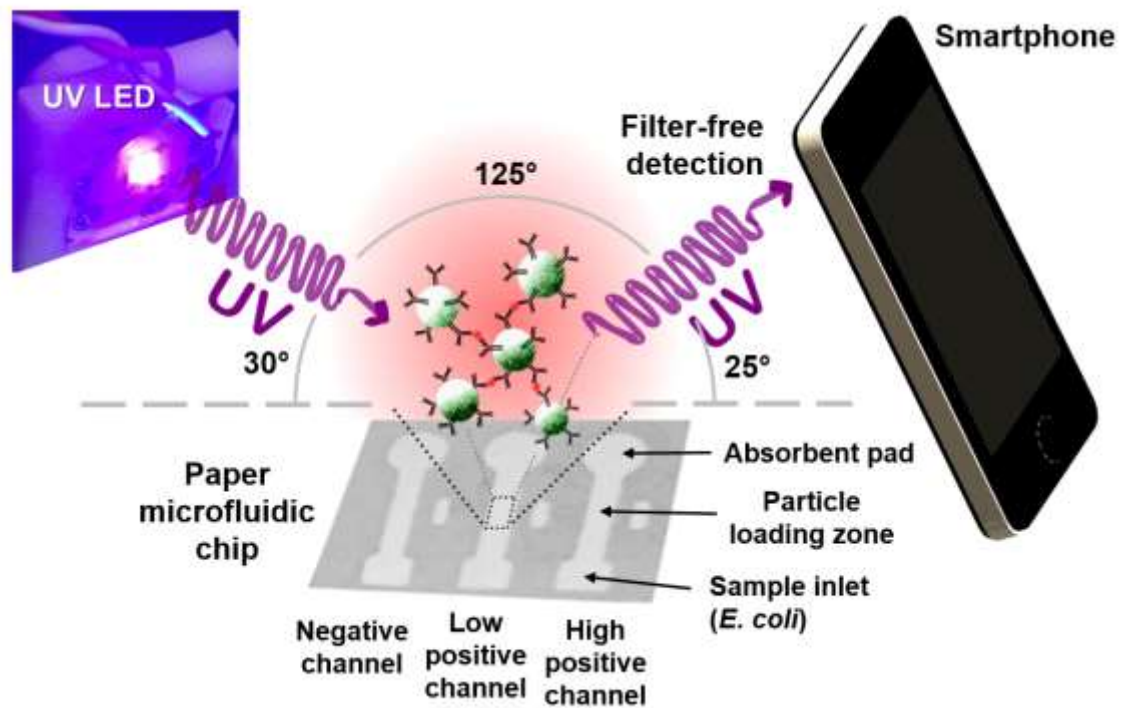


Figure D - 1

Schematic illustration of the UV LED enhanced particle immunoagglutination assay on paper microfluidics and subsequent smartphone detection. Antibodies (Y-shaped) are conjugated to the green fluorescent polystyrene particles (green spheres). The presence of *E. coli* antigens (red dots) triggers antibody-antigen binding and subsequently immunoagglutination of particles.

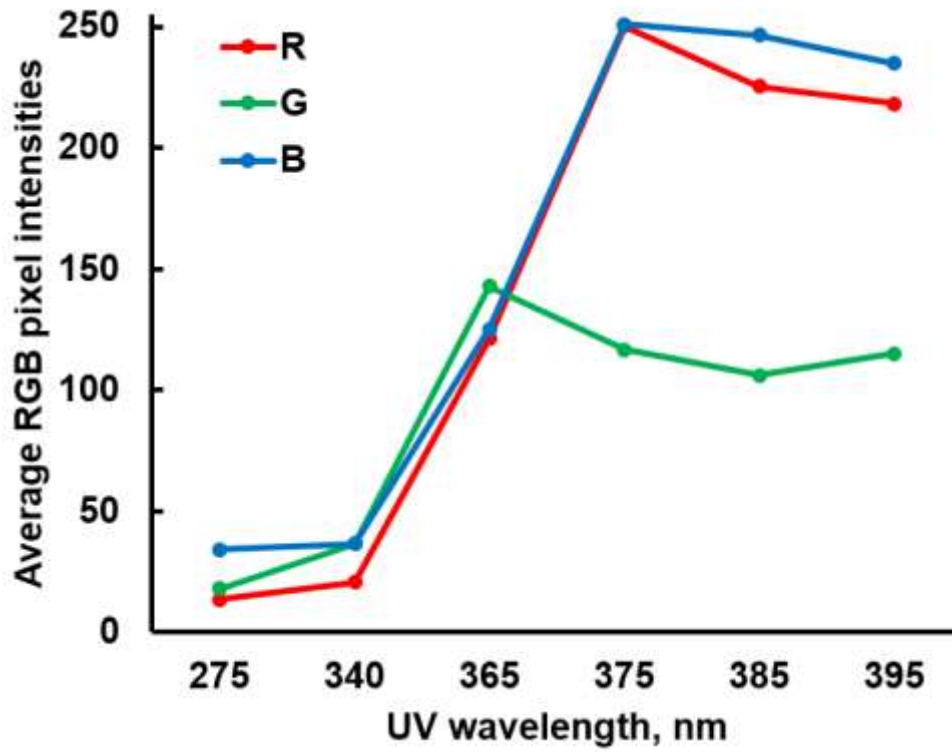


Figure D - 2

Average red, green, and blue (RGB) pixel intensities of a smartphone upon UV LED irradiation.

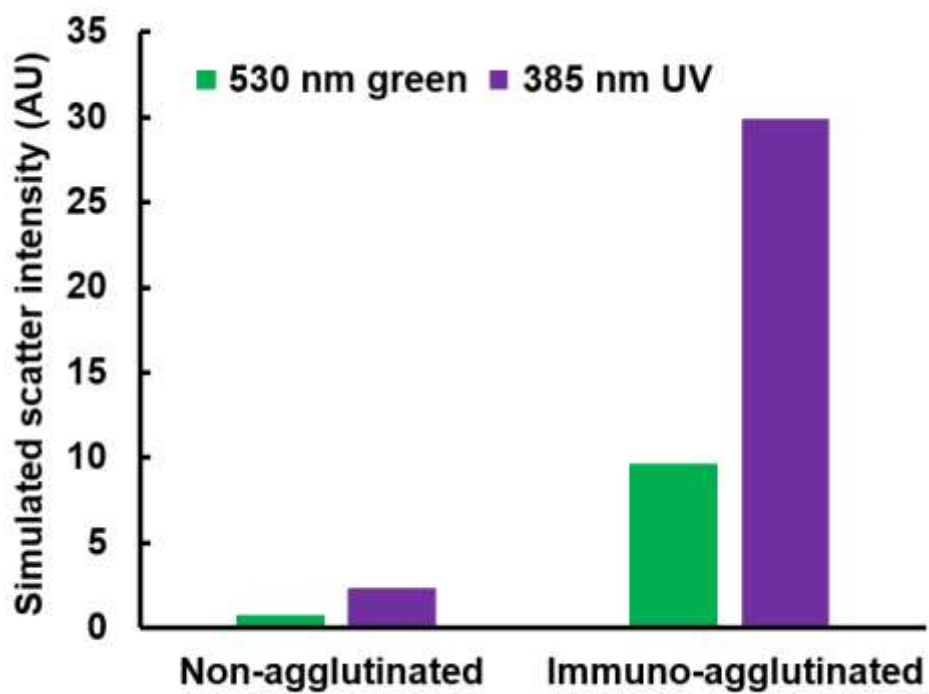


Figure D - 3

Simulated Mie scatter intensities (arbitrary unit) for the non-agglutinated PS particle (920 nm) and the immunoagglutinated particle (with twice the diameter, 1840 nm) under green (530 nm) and UV (385 nm) irradiation.

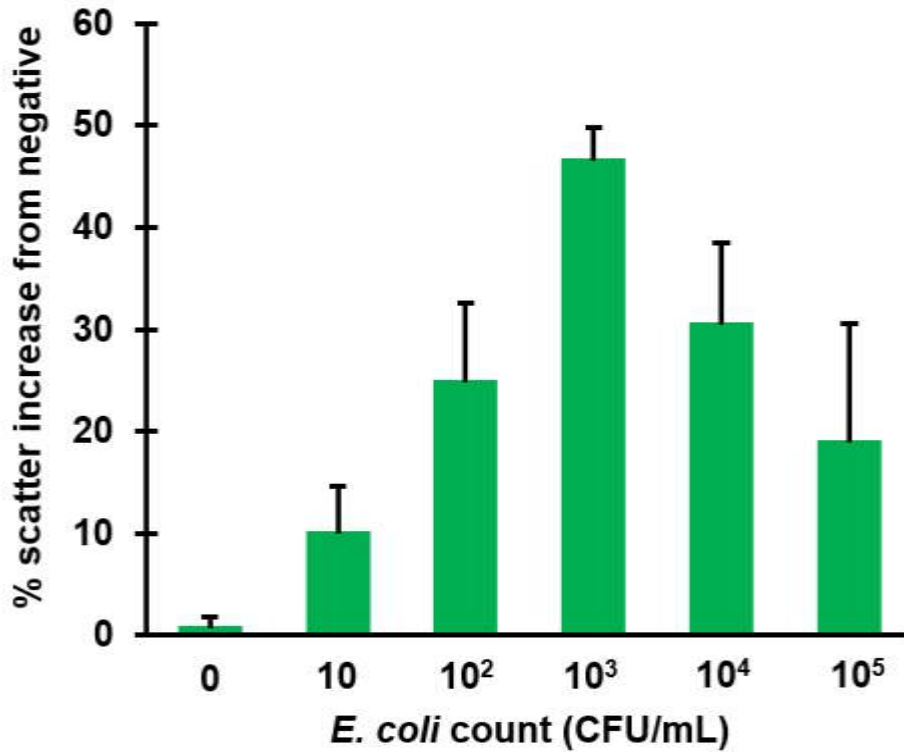


Figure D - 4

The result of paper microfluidic assay for the *E. coli* in deionized water using the 385 nm UV LED. Green pixel intensities were evaluated and double-normalized as described in Materials and Method. 920 nm anti-*E. coli* conjugated PS particles were pre-loaded to the center of each paper microfluidic channel prior to the assays. Average of three different experiments, each time using different samples and different paper microfluidic chips. Error bars are standard errors.

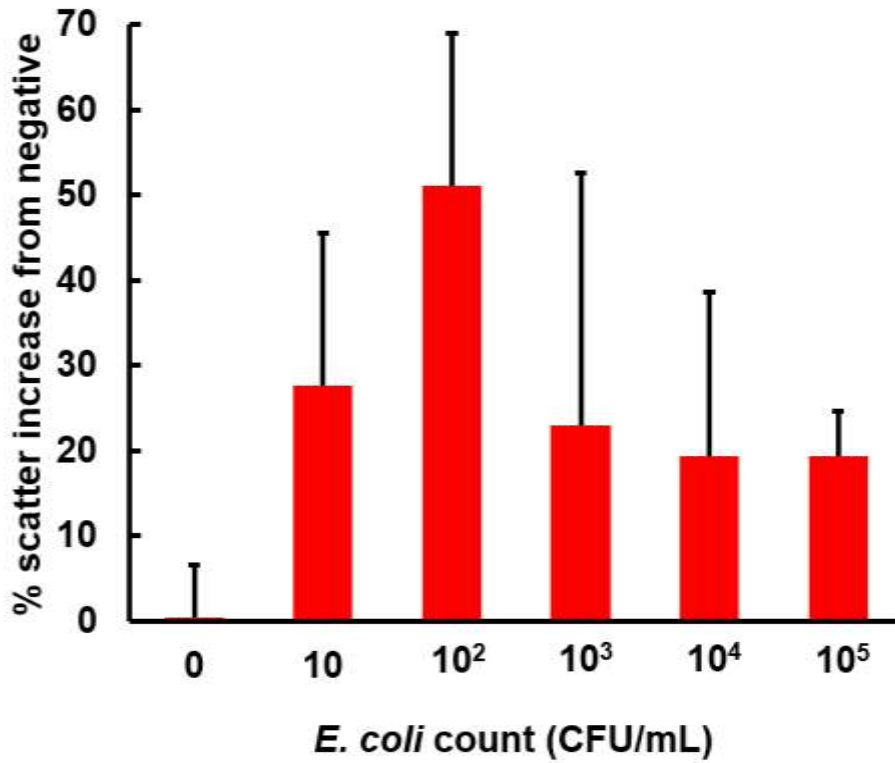


Figure D - 5

The result of paper microfluidic assay for the *E. coli* in 10% human whole blood. All other conditions are identical to those shown in Figure 4. Average of three different experiments, each time with different samples and paper microfluidic chips. Error bars are standard errors.

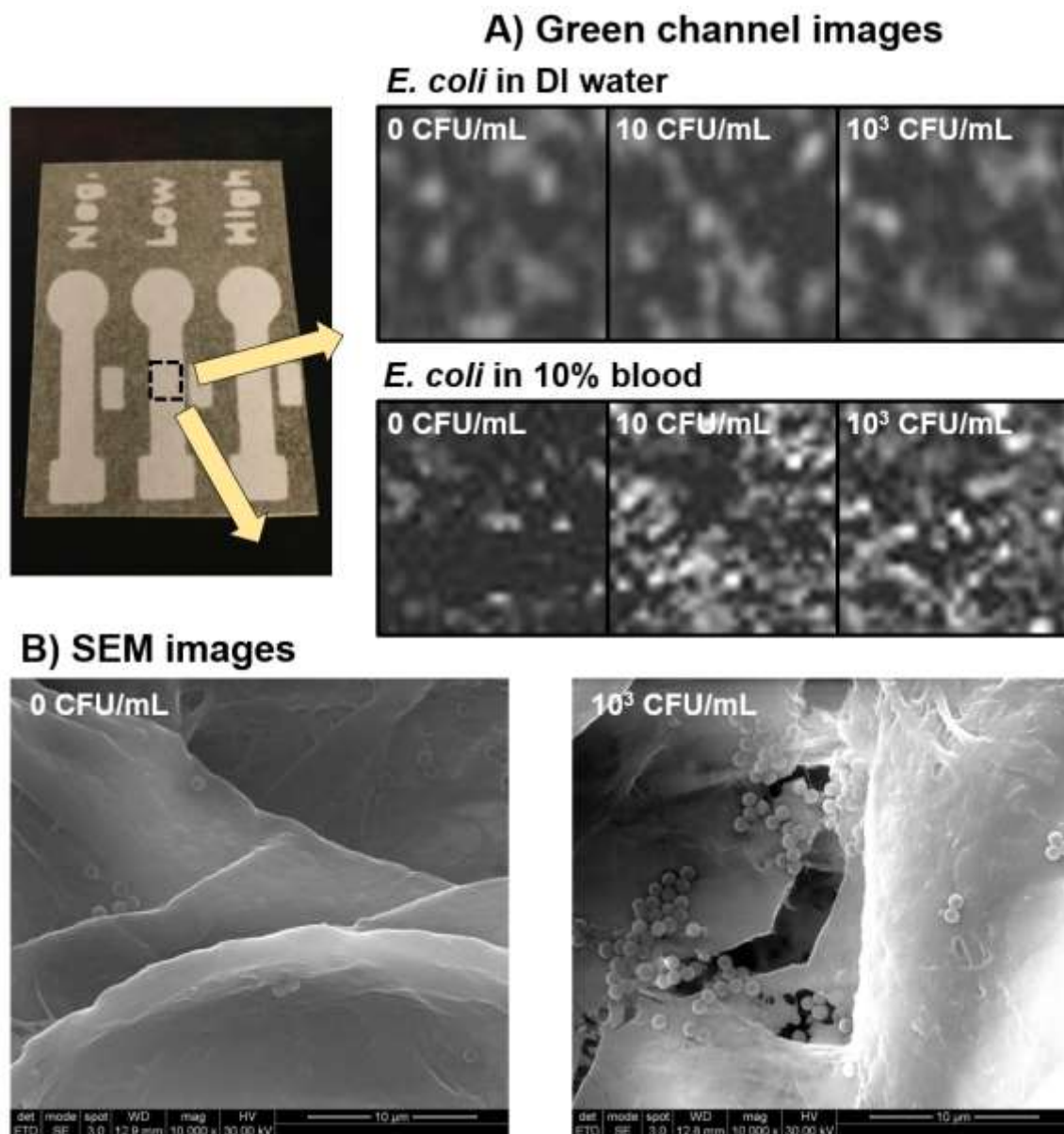


Figure D - 6

(A) A series of macroscopic, green channel images of the central detection zone of each paper microfluidic channel with 0, 10, and 10^3 CFU/mL *E. coli* in DI water or 10% whole blood. (B) SEM images of the central detection zone of each paper microfluidic channel with 0 and 10^3 CFU/mL *E. coli* in DI water.

Appendix E

Multi-Normalization and Interpolation Protocol to Improve Norovirus Immunoagglutination Assay from Paper Microfluidics with Smartphone Detection

Soohee Cho¹, Tu San Park^{1†}, Kelly A. Reynolds² and Jeong-Yeol Yoon^{1,3}

¹Department of Agricultural and Biosystems Engineering, and ²Mel and Enid Zuckerman College of Public Health, ³Department of Biomedical Engineering, The University of Arizona, Tucson, Arizona 85721, USA

[†]Present address: Department of Bio-industrial Machinery Engineering, Kyungpook National University, Daegu 750-701, Republic of Korea.

Corresponding Author:

Jeong-Yeol Yoon, Department of Biomedical Engineering and Department of Agricultural and Biosystems Engineering, The University of Arizona, 1177 E. 4th St., Rm. 403, Tucson, AZ 85721-0038, USA. E-mail: jyoon@email.arizona.edu.

Manuscript accepted by SLAS Technology.

Abstract

Norovirus (NoV) is one of the leading causes of acute gastroenteritis, affecting 685 million people per year around the world. The best preventive measure is to screen water for possible NoV contamination, not from infected humans, preferably utilizing rapid and field-deployable diagnostic methods. While enzyme immunoassays (EIAs) can be used for such detection, the low infectious dose as well as the generally inferior sensitivity and low titer of available NoV antibodies render critical challenges in using EIAs towards NoV assays. In this work, we demonstrated smartphone-based Mie scatter detection of NoV with immunoagglutinated latex particles on paper microfluidic chips. Using only three different concentrations of anti-NoV conjugated particles, we were able to construct a single standard curve that covered seven orders of magnitude of NoV antigen concentrations. Multiple normalization steps and interpolation procedures were developed to estimate the optimum amount of antibody-conjugated particles that matched to the target NoV concentration. We also demonstrated a very low detection limit of 10 pg/mL without using any concentration or enrichment steps. This method can also be adapted to any other virus pathogens whose antibodies possess low sensitivity and low antibody titer.

Keywords: Paper microfluidic analytic device; μ PAD; smartphone; biosensor; water safety

1. Introduction

Norovirus (NoV) is the leading cause of illness and outbreaks from contaminated food and water around the world. According to the U.S. Centers for Disease Control and Prevention (CDC), NoV causes 19-21 million cases of acute gastroenteritis annually in the United States, and 685 million cases globally. NoV is extremely contagious with an infectious dose as few as 18 viral particles¹ or 1×10^2 copies/mL.²

The standard diagnostic methods are: 1) detection of viral RNA by reverse transcription-polymerase chain reaction (RT-PCR) or 2) detection of viral antigens by enzyme immunoassays (EIAs), including enzyme-linked immunosorbent assay (ELISA). While RT-PCR provides excellent sensitivity with a detection limit of $<10^2$ copies/mL,³ this technique is time-consuming, laborious, and requires expensive equipment and reagents that may not be readily available. Although EIAs are inferior to RT-PCR in their sensitivity and detection limits, they provide rapid results and serve as a preliminary detection method to meet acute gastroenteritis outbreak analysis demands. Thus, many commercial EIA kits are available. For example, RIDASCREEN® Norovirus 3rd Generation EIA has been cleared by the U.S. Food and Drug Administration (FDA). However, its intended use is limited to NoV detection in human stool from ill patients (thus not requiring low detection limit) and RT-PCR validation is still recommended. To be used as a preventive measure especially for water samples, high sensitivity and very low detection limit are necessary. Unfortunately, most antibodies to NoV show low reactivity with specific NoV strains, leading to a very high detection limit (i.e. $> 10^6$ virus particles per gram of feces).⁴ In addition, most currently available NoV antibodies have a significantly low antibody titer (or ELISA titer). This leads to an extremely narrow linear range

of detection, thus rendering the assay less useful for NoV quantification. All of these complications are more or less associated with the uncultivable nature of NoV.⁵

Due to these limitations, NoV has been detected from stool samples from progressively ill human subjects, where NoV concentrations are very high. To develop preventive diagnostic tool for acute gastroenteritis outbreaks, potentially contaminated water sources must be tested. Towards this end, there is a need to improve NoV EIAs towards: 1) very low detection limit and 2) a much wider concentration range, enabling rapid, sensitive, and easily quantifiable assays. There have been several recent studies to improve NoV EIAs through alternative sensing modalities or sample enrichment (i.e. concentration methods). These recent studies are summarized in **Table 1**, where detection limits were indeed reduced by various means. However, these methods require additional steps that are complicated and time-consuming, including sample purification/enrichment,^{2,6,7} use of NoV virus-like particles (VLPs),⁷⁻¹¹ or the use of RT-PCR,¹¹ thus forgoing the true merits of EIAs over RT-PCR.

Our group has previously demonstrated particle immunoagglutination assay coupled with angle-specific Mie scatter detection on various microfluidic platforms for assaying various pathogens.¹²⁻¹⁷ In this assay, antibody-conjugated latex particles immunologically agglutinate in the presence of target antigens, thus increasing the effective particle diameter. Monitoring Mie scatter at an angle optimized for such agglutination allows the detection and quantification of target antigens. Additionally, particle immunoagglutination has been demonstrated on simple and low-cost paper microfluidic platforms.^{14,15} More importantly, paper platforms provide an additional advantage in providing intrinsic filtration capabilities with the fibrous pores, as previously demonstrated.¹⁸ Incorporating smartphone-based detection with paper microfluidics has allowed momentous strides towards field-deployable, affordable, and easy-to-use assays.¹⁷

Our previous studies demonstrated low detection limits using Mie scatter detection of immunoagglutinated latex particles on paper microfluidic platforms. This principle worked successfully with commercially available antibodies that have high ELISA titer, e.g., 1 : 17,000 of antibody to *Escherichia coli* (anti-*E. coli*). However, such methods are limited with low ELISA titer antibodies, such as anti-NoV (1 : 2,000). In fact, preliminary studies performed in our laboratory showed a mere one order of magnitude linear range for a Mie scatter immunoagglutination NoV assay.

In this work, we demonstrated a particle immunoagglutination assay of the capsid proteins from NoV using smartphone-based Mie scatter detection. Wax printing was used as a simpler means for fabricating paper microfluidic channels, which has recently gained wide popularity in the microfluidics area.¹⁹⁻²¹ Capsid proteins from the viral coat of NoV were used as a realistic surrogate without risking use of actual infectious samples. Positive signals were normalized following previously performed methods.¹⁵ Three different concentrations of anti-NoV conjugated latex particles were introduced to three different channels of a single paper microfluidic chip. Through interpolation analysis, we demonstrated the linear range of assay over seven orders of magnitude, which has not been demonstrated previously. In addition, we also demonstrated extremely low detection limits, down to 10 pg/mL, which has not yet been demonstrated for NoV EIAs in a rapid assay platform. Such enhancements in sensitivity and broad assay range will provide a strong promise for the EIAs with weak antibodies, towards efficiently determining the contamination source and preventing epidemics.

2. Materials and Method

2.1 Fabrication of Paper Microfluidic Chips

Fabrication of paper microfluidic chips using a wax printer is demonstrated in **Fig. 1**. Paper microfluidic chips with multiple parallel channels were loaded with different amounts of antibody conjugated or bovine serum albumin (BSA) conjugated latex particles. Chips were designed using SolidWorks (Dassault Systemes, SolidWorks Corporation; Waltham, MA, USA) with inlet and absorbent pad dimensions of 4-mm wide and 2-mm long, and channel dimensions of 2-mm wide and 14.5-mm long. Chip designs were printed with solid ink on cellulose chromatography paper (GE Healthcare, Maidstone, Kent, UK) using a wax printer (ColorQube 8580, Xerox, Wilsonville, OR, USA). Individual chips were cut out and placed on a hot plate at 100°C for < 100 seconds to melt the wax through the entire paper. Chips were stored in sealed, dry, and dark conditions if not used immediately.

2.2 Conjugation of Anti-NoV to Latex Particles

Polystyrene (PS) latex particles (Magsphere, Pasadena, CA, USA) of 920-nm diameter were covalently conjugated with polyclonal antibodies to norovirus capsid protein (anti-NoV; Abcam, Cambridge, MA, USA) or bovine serum albumin (BSA; Sigma-Aldrich) following the protocol described in Cho et al.¹⁵ The concentrations of conjugated particle suspensions were calibrated by the method detailed in Park et al.¹⁷ and You et al.¹² to yield varying particle concentrations (w/v %) from 0.01%, 0.022%, and 0.045%, for both anti-NoV conjugated particles and BSA conjugated particles. These particles were stored in deionized (DI) water at 4°C.

2.3 Sample Preparation

Positive samples consisted of recombinant NoV capsid protein antigens (MyBioSource, San Diego, CA, USA) diluted in sterilized DI water. Dilutions were made to the following concentrations: 10 pg/mL, 100 pg/mL, 1 ng/mL, 10 ng/mL, 100 ng/mL, 1 µg/mL, and 10 µg/mL. DI water without the presence of NoV antigens was used as a blank sample.

2.4 Smartphone-based Immunoassay Procedure

A smartphone (iPhone 5, Apple, Cupertino, CA, USA) was positioned in a 3D-printed angled holder described in Cho et al.¹⁵ The smartphone was angled 25° and 9 cm vertically from the paper microfluidic chip (**Fig. 1c**), where the Mie scatter simulation showed the greatest change in scattering intensity as the particle size increased. The smartphone app VSCO (Visual Supply Company, Oakland, CA, USA) was used to lock white balance and focus to the channel center, and images were taken with a shutter speed of 1/600 s on average (**Fig. 1c**). All experiments were performed under a normal ambient lighting condition (fluorescent lamps).

A volume of 1.7 µL of anti-NoV conjugated particles or BSA conjugated particles was pre-loaded on the center of each positive channel or negative channel, respectively. Paper chips were subsequently dried at room temperature. 7 µL of sample (with varying NoV concentration) was added to the positive channel (with anti-NoV conjugated particles pre-loaded), as well as the negative channel (with BSA conjugated particles pre-loaded). Identical particle concentrations (anti-NoV or BSA conjugated) were used when comparing the positive to the negative channel results.

Two image acquisitions were performed for normalization purposes. The first image was taken after the pre-loaded particles were dried (**Fig. 1c**). The second image was taken after the

loaded samples entered the absorbent pad (**Fig. 1d**). Triplicate sets of experiments were performed for each particle concentration (a total of 3 concentrations) and each target NoV concentration (a total of 8 concentrations including a blank) - each time using a new microfluidic chip with different samples.

The extent of particle immunoagglutination was measured at the channel center. RGB images were split into their green channel components using ImageJ software (National Institute of Health; Bethesda, MD, USA). Scatter intensities were recorded from the microfluidic channel centers in these green channel images, which have previously enabled maximum change in scatter intensity under ambient lighting.¹⁸ Upon immunoagglutination, the effective size of particles is expected to increase, causing an increase in scatter intensity at the optimized detection angle. This increase can be quantified from the (green) pixel intensities taken from the central area of each channel. A sample intensity plot is shown in **Fig. 1d**, where the channel pre-loaded with 0.01 w/v% anti-NoV particles shows the maximum pixel intensities with 1 ng/mL NoV sample.

2.5 Data Normalization

After obtaining signal intensities, double-normalization was done similar to the previously detailed method in Cho et al.¹⁵ The first step is “background-normalization” by dividing the green scatter intensity from the central channel region with that from the background. This step accounts for the channel-to-channel variation and the effects of different ambient lighting conditions of individual channels. The second step is “blank-normalization” by dividing the background normalized value from the positive channel (pre-loaded with anti-NoV conjugated particles) with the same from the negative channel (pre-loaded with BSA conjugated

particles). All channels were loaded with the same amount of anti-NoV and BSA conjugated particles. This step accounts for any variations arising from the extent of non-specific aggregation of anti-NoV particles, in reference to the non-aggregated BSA conjugated particles, prior to performing immunoagglutination assays.

2.6 Construction of Standard Curve through Data Interpolation

After double normalization, three double-normalized intensities per particle concentration were available for each NoV concentration. An equivalent amount of antibody conjugated particles was obtained for each NoV concentration through interpolating these raw data, which is described in Results and Discussion. This equivalent amount of antibody conjugated particles was plotted against NoV concentration to construct a standard curve. Analysis of variance (ANOVA) of this standard curve was performed by Stata/IC 12.0.²²

3. Results and Discussion

Double-normalized intensities were obtained from the particle immunoagglutination assays on the paper microfluidic chips using a smartphone. **Fig. 2a** shows the results of NoV assays with varying concentrations of pre-loaded anti-NoV particles. While seven orders of magnitude of NoV concentrations were evaluated in this work, the linear range of assay appeared limited, covering just a few orders of magnitude followed by a decrease in double normalized scatter intensities, for the given amount of anti-NoV conjugated particles. This can be explained by the inferior sensitivity and very low ELISA titer of anti-NoV used in this study.

However, a noticeable trend can be observed from the entire data set. It is possible to find out the optimum anti-NoV particle concentration for detecting specific NoV concentration

through stacking the three individual plots (**Fig. 2b**). For 10^1 pg/mL, the double-normalized intensity was maximized with 0.01% anti-NoV particles. This maximum intensity seemed to gradually shift to the channel with 0.022% anti-NoV particles as NoV concentration increased up to 10 ng/mL ($= 10^4$ pg/mL). Further shift was observed with the 0.045% anti-NoV particles as NoV concentration increased to 1 μ g/mL ($= 10^6$ pg/mL) and 10 μ g/mL ($= 10^7$ pg/mL). Apparently, an optimum amount of anti-NoV conjugated particles, and thus an antibody amount, seemed to exist for the given concentration of NoV capsid proteins. Such antibody amounts were calculated through interpolating the raw data set shown in **Fig. 2**.

The interpolated value of anti-NoV conjugated particles for the given NoV concentration was calculated in the following manner (**Fig. 3**): First, three double-normalized intensities were divided by the lowest double-normalized intensities (i.e. normalization to the minimum intensity), then multiplied by 100. Second, these intensities were divided by the sum of all intensities obtained in the first step. For example, the 10 pg/mL data can be represented as 60% with the 0.01% anti-NoV particles, 40% with the 0.022% anti-NoV particles, and 0% with the 0.045% anti-NoV particles (the last is the minimum intensity). Therefore, the matching amount of anti-NoV particles should be in between 0.01% and 0.022%, with 60% close to 0.01% and 40% close to 0.022%. To obtain the interpolated amount of anti-NoV particles, the particle concentration was multiplied with the rendered percentage and added together, e.g. $0.01\% \times 0.6 + 0.022\% \times 0.4 = 0.015\%$ for the 10 pg/mL data set. This number indicates the estimated particle concentration that optimally matches to the given NoV concentration. Through repeating this calculation for individual trials, it is also possible to obtain standard errors for the estimated particle concentrations.

The interpolated anti-NoV particle concentrations were plotted against the NoV concentrations to construct a single standard curve, and the result is shown in **Fig. 4**. The curve yielded a generally increasing trend, with a linear equation of $y = 0.0052x + 0.0043$ and R^2 value of 0.94. This linear equation can be used to determine NoV concentration from three double normalized intensities from a single chip. A positive correlation between the anti-NoV particle concentration and the \log_{10} NoV concentration was observed and determined statistically significant by ANOVA ($p < 0.001$). In addition, all of the interpolated data points showed 99% confidence interval ($\text{mean} \pm 2.58 \times \text{standard error}$) higher than the reference point 0, indicating successful detection over all seven orders of magnitude of NoV concentrations. Overall, this original interpolation method supports that the optimum antibody amounts must be determined for NoV detection in future sensing applications.

4. Conclusion

Rapid, simple, and sensitive method of detecting NoV antigens from water samples is demonstrated in this work that can be used towards a precautionary measure to prevent acute gastroenteritis outbreaks. While EIAs are suitable methods as a rapid detection method for NoV, they suffer inherent limitations arising from inferior sensitivity and low ELISA titer of available antibodies to NoV. Due to these limitations, most NoV EIAs are for analyzing human stool samples from already infected subjects, whose NoV concentrations are sufficiently high (at least a few ng/mL). Other complementary methods have been attempted to overcome these limitations, but have typically made the assay substantially slower and laborious, for example, adding an additional step of PCR.¹¹ The innovative approach used in this work was able to demonstrate a very low detection limit (10 pg/mL) without adding additional steps. In addition,

this method achieved an extremely wide linear range of assay (seven orders of magnitude), through simply using three different concentrations of anti-NoV conjugated particles. This method can also be adapted to any other virus pathogen whose antibodies are less sensitive and have low ELISA titer. Ultimately, this novel method may enhance the preventive power of EIAs towards efficient determination of contaminated water sources in order to prevent epidemics.

5. Acknowledgements

Ms. Jamie L. Hernandez at the University of Arizona (currently at University of Washington) assisted with running the assays; Mr. Collin A. Gilchrist at the University of Arizona assisted the fabrication of paper microfluidic chips and preparation of reagents.

6. Declaration of Conflicting Interests

The authors declared no potential conflicts of interest with respect to the research, authorship, and/or publication of this article.

7. Funding

Funding for this research was provided by the Water and Environmental Technology (WET) Center and BIO5 Institute at the University of Arizona, as well as Tucson Water.

8. References

1. Teunis, P.F.M.; Moe, C.L.; Liu, P.; Miller, S.E.; Lindesmith, L.; Baric, R.S.; Le Pendu, J.; Calderon, R.L. Norwalk Virus: How Infectious is it? *J. Med. Virol.* **2008**, *80*: 1468-1476.

2. Yakes, B. J.; Papafragkou, E.; Conrad, S. M.; Neill, J.D.; Ridpath, J. F.; Burkhardt III, W.; Kulka, M.; DeGrasse, S. L. Surface Plasmon Resonance Biosensor for Detection of Feline Calicivirus, a Surrogate for Norovirus. *Int. J Food Microbiol.* **2013**, *162*, 152-158.
3. Hong, S.A.; Kwon, J.; Kim, D.; Yang, S. A Rapid, Sensitive and Selective Electrochemical Biosensor with Concanavalin A for the Preemptive Detection of Norovirus. *Biosens. Bioelectron.* **2015**, *64*: 338-344.
4. Costantini, V.; Grenz, L.; Fritzing, A.; Lewis, D.; Biggs, C.; Hale, A.; Vinjé, J. Diagnostic Accuracy and Analytical Sensitivity of IDEIA Norovirus Assay for Routine Screening of Human Norovirus. *J. Clin. Microbio.* **2010**, *48*, 2770-2778.
5. Jones, M.K.; Watanabe, M.; Zhu, S.; et al. Enteric Bacteria Promote Human and Mouse Norovirus Infection of B Cells. *Science.* **2014**, *346* (6210), 755-759.
6. Shigemoto, N.; Tanizawa, Y.; Matsuo, T.; Sakamaki, N.; Ohiro, Y.; Takayasu, S.; Fukuda, S. Clinical Evaluation of a Bioluminescent Enzyme Immunoassay for Detecting Norovirus in Fecal Specimens from Patients with Acute Gastroenteritis. *J. Med. Virol.* **2014**, *86*: 1219-1225.
7. Hurwitz, A. M.; Huang, W.; Kou, B.; Estes, M. K.; Atmar, R. L.; Palzkill, T. Identification and Characterization of Single-chain Antibodies that Specifically Bind GI Noroviruses. *PLOS ONE* **2017**, *12*, e0170162.
8. Yasuura, M.; Fujimaki, M. Detection of Extremely Low Concentrations of Biological Substances Using Near-Field Illumination. *Sci. Rep.* **2016**, *6*, 39241.
9. Ashiba, H.; Sugiyama, Y.; Wang, X.; Shirato, H.; Higo-Moriguchi, K.; Taniguchi, K.; Ohki, Y.; Fujimaki, M. Detection of Norovirus Virus-like Particles Using a Surface Plasmon

- Resonance-assisted Fluoroimmunosensor Optimized for Quantum Dot Fluorescent Labels. *Biosens. Bioelectron.* **2016**, doi: 10.1016/j.bios.2016.08.099.
10. Hagström, A.E.V.; Garvey, G.; Paterson, A.S.; Dhamane, S.; Adhikari, M.; Estes M.K.; Strych, U.; Kourentzi, K.; Atmar, R.L.; Wilson, R.C. Sensitive Detection of Norovirus Using Phage Nanoparticle Reporters in Lateral-Flow Assay. *PLoS ONE.* **2015**, 10(5): e0126571.
 11. Matsushita, T.; Shirasaki, N.; Tatsuki, Y.; Matsui, Y. Investigating Norovirus Removal by Microfiltration, Ultrafiltration, and Precoagulation-microfiltration Processes Using Recombinant Norovirus Virus-like Particles and Real-time Immuno-PCR. *Water Res.* **2013**, 47, 5819-5827.
 12. You, D.J.; Geshell, K.J.; Yoon, J.-Y. Direct and Sensitive Detection of Foodborne Pathogens within Fresh Produce Samples Using a Field-Deployable Handheld Device. *Biosens. Bioelectron.* **2011**, 28(1): 399-406.
 13. Fronczek, C.F.; You, D.J.; Yoon, J.-Y. Single-pipetting Microfluidic Assay Device for Rapid Detection of Salmonella from Poultry Package. *Biosens. Bioelectron.* **2013**, 40(1): 342-349.
 14. Park, T. S.; Li, W.; McCracken, K. E.; Yoon, J.-Y. Smartphone Quantifies *Salmonella* from Paper Microfluidics. *Lab Chip* **2013**, 13, 4832-4840.
 15. Cho, S.; Park, T.S.; Nahapetian, T. G.; Yoon, J.-Y. Smartphone-based, Sensitive μ PAD Detection of Urinary Tract Infection and Gonorrhea. *Biosens. Bioelectron.* **2015**, 74, 601-611.
 16. Nicolini, A. M.; Fronczek, C. F.; Yoon, J.-Y. Droplet-based Immunoassay on a 'Sticky' Nanofibrous Surface for Multiplexed and Dual Detection of Bacteria Using Smartphones. *Biosens. Bioelectron.* **2015**, 67, 560-569.

17. Park, T. S.; Cho, S.; Nahapetian, T. G.; Yoon, J.-Y. Smartphone Detection of UV LED-Enhanced Particle Immunoassay on Paper Microfluidics. *SLAS Technol.* **2017**, *22*, 7-12.
18. Park, T. S.; Yoon, J.-Y. Smartphone Detection of *Escherichia coli* from Field Water Samples on Paper Microfluidics. *IEEE Sens. J.* **2015**, *15*, 1902-1907.
19. Jang, I.; Song, S. Facile and Precise Flow Control for a Paper-based Microfluidic Device through Varying Paper Permeability. *Lab Chip.* **2015**, *15*: 3405-3412.
20. Torul, H.; Ciftci, H.; Cetin, D.; Suludere, Z.; Boyaci, I.H.; Tamer, U. Paper Membrane-based SERS Platform for the Determination of Glucose in Blood Samples. *Anal. Bioanal. Chem.* **2015**, *407*(27): 8243-8251.
21. Kim, J.-Y.; Yeo, M.-K. A Fabricated Microfluidic Paper-based Analytical Device (μ PAD) for *In Situ* Rapid Colorimetric Detection of Microorganisms in Environmental Water Samples. *Mol. Cell. Toxicol.* **2016**, *12*(1): 101-109.
22. StataCorp LP. *Stata/IC 12.0*. **2011**, <http://www.stata.com>.
23. Noel, J.S.; Frankhauser, R.L.; Ando, T.; Monroe, S.S.; Glass, R.I. Identification of a Distinct Common Strain of “Norwalk-like Viruses” Having a Global Distribution. *J. Infect. Dis.* **2000**, *179*(6): 1334-1344.

9. Figures and Table

Target	Ref.	Sample matrix	Detection limit	Method	Limitations
Calciavirus (NoV surrogate)	[2]	Purified cell culture lysates	10^4 TCID ₅₀ /mL	SPR	Not tested for NoV. Purification necessary. Requires SPR equipment.
NoV capsid proteins	[6]	Fecal supernatant	10^6 copies/g stool	Enzyme immunoassay	Enrichment necessary. Requires bioluminescence.
GI.1 VLPs GI.7 VLPs	[7]	Stool	0.1-0.2 ng 6.25-25 ng	Immunoassay	Require stool from infected patients, and pre-treatment.
GII NoV VLPs	[8]	Treated municipal wastewater	~400 VLPs/mL	Illumination biosensor	Can detect only low NoV conc. Dilution necessary for high conc.
GI.1 NoV VLPs GII.4 NoV VLPs	[9]	Buffer solution	4.3×10^5 VLPs/mL	SPR	Requires SPR equipment.
GI.1 NoV VLPs	[10]	Buffer solution	10^7 VLPs/mL	Lateral flow assay	High detection limit. Requires reagent prep.
Recombinant NoV VLPs	[11]	River water	10^5 VLPs/mL	ELISA + PCR	Requires PCR.

Note: Noroviruses are generally classified into five genogroups: GI, GII, GIII, GIV and GV. Each genogroups possesses different genotypes, such as GI.1, GI.7, GII.4, etc. VLP = virus-like particles. SPR = surface plasmon resonance. ELISA = enzyme-linked immunosorbent assay. PCR = polymerase chain reaction.

Table E - 1

Summary of NoV assays reported in recent literature.

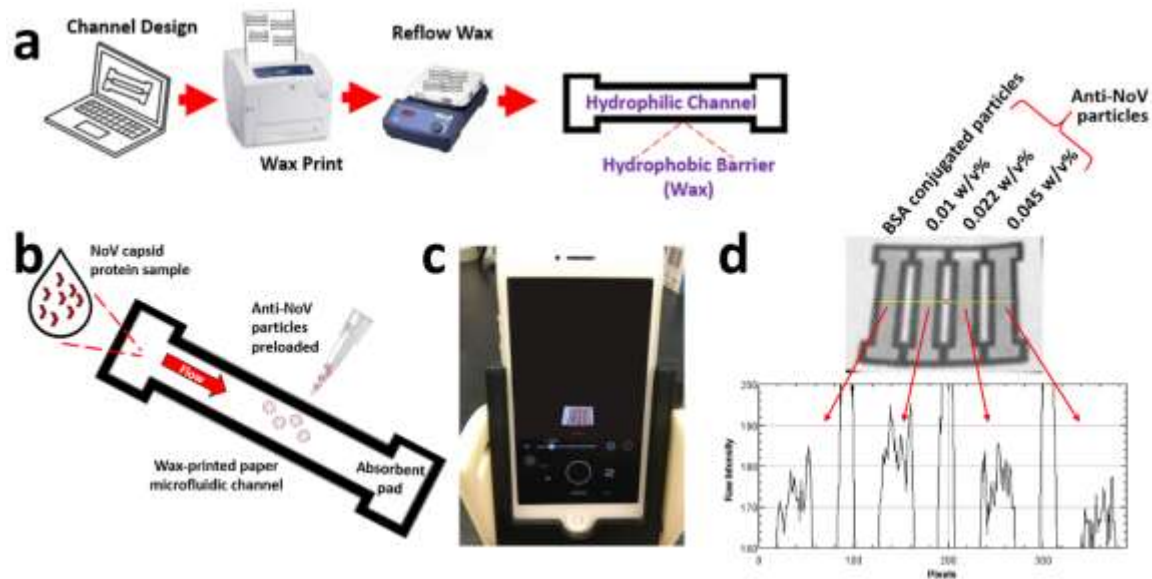


Figure E - 1

Assay procedure. a) Microchannel layouts were designed in SolidWorks and printed to chromatographic paper using a wax printer. The printed chips were placed on a hot plate to melt the wax, filling the entire depth of paper, creating hydrophobic wax barriers around the microfluidic channel. b) Anti-NoV conjugated particles were preloaded and dried at the center of each microfluidic channel. Sample solution containing NoV capsid proteins was loaded to the inlet of the microfluidic channel. c) Image of a paper microfluidic chip, acquired from smartphone app. d) Intensity profile across all four channels for immunoassaying 1 ng/mL NoV sample. An average raw intensity was evaluated for each channel. For this case, the intensity was maximum where 0.01 w/v% anti-NoV particles were loaded.

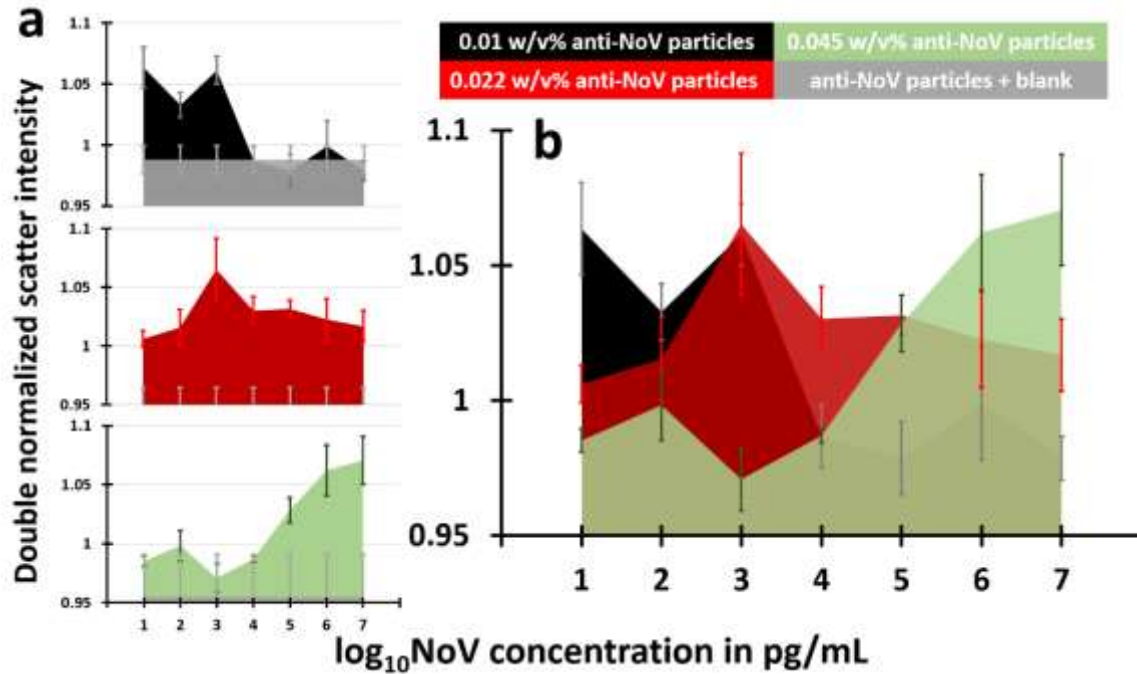


Figure E - 2

Results of particle immunoagglutination assay with smartphone-based Mie scatter detection from paper microfluidic chips. All data were normalized to those from a negative channel, where the same amount of BSA conjugated particles were pre-loaded. Data represents an average of three different experiments, each time using different paper microfluidic chip. Error bars represent standard errors. a) Double normalized scatter intensity plotted against log₁₀ NoV concentration in pg/mL, using 0.01 w/v% (black), 0.022 w/v% (red), and 0.045 w/v% (green) anti-NoV conjugated particles. Blank signals are represented in grey color. b) All three plots were stacked together.

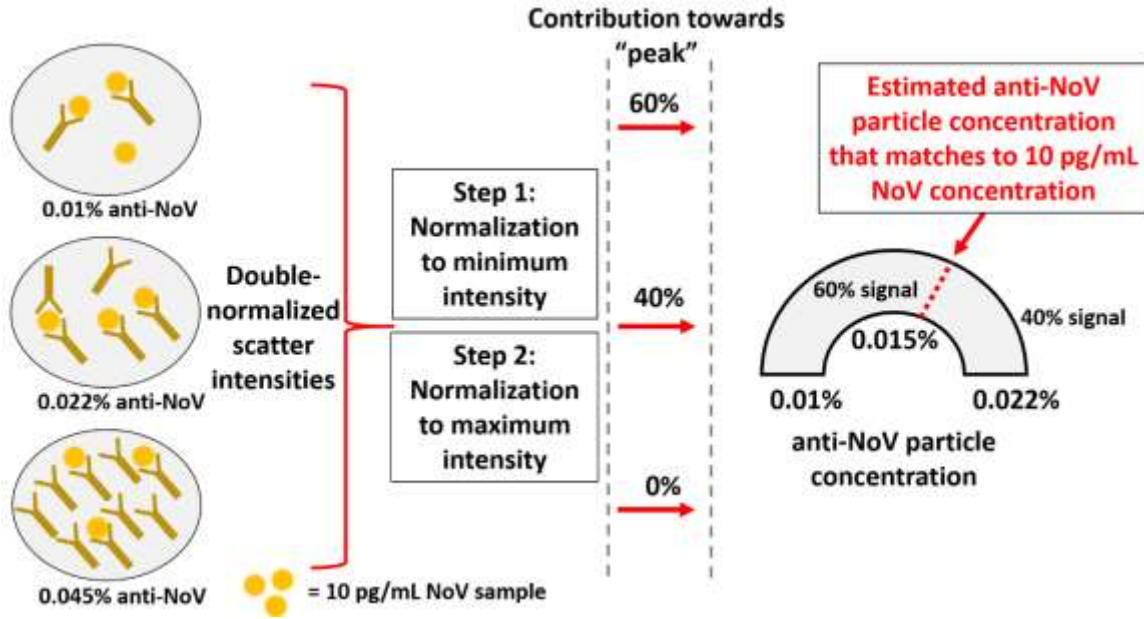


Figure E - 3

Graphical illustration for estimating the interpolated value of anti-NoV particle concentration for the given NoV concentration (in this case, 10 pg/mL).

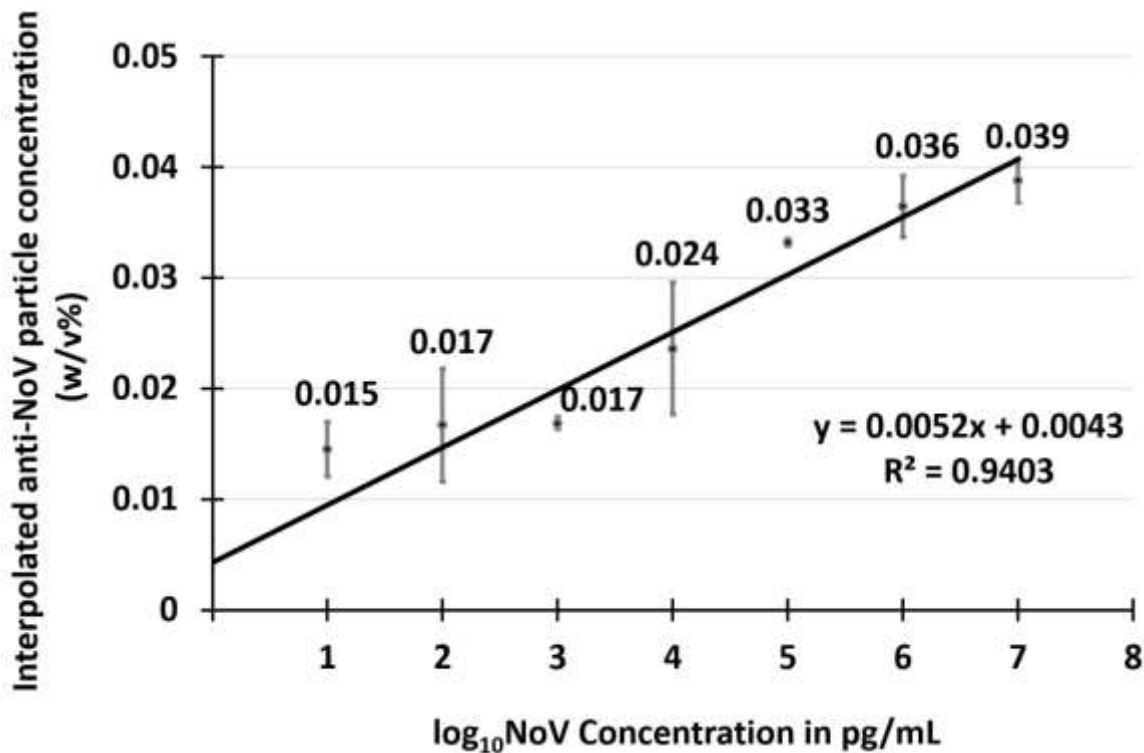


Figure E - 4

The interpolated anti-NoV particle concentrations were plotted against \log_{10} NoV concentration in pg/mL. Each data point was obtained from 9 different experiments (three different anti-NoV particle concentration, each replicated three times). Error bars represent standard errors. The 99% confidence intervals ($\text{mean} \pm 2.58 \times \text{standard error}$) for all data points were higher than 0, indicating all data points are statistically different from the blank with 99% confidence.

Appendix F

Paper Angiogenesis-on-a-chip

Soohee Cho¹ and Jeong-Yeol Yoon^{1,2}

¹Department of Agricultural and Biosystems Engineering, and ²Department of Biomedical Engineering, The University of Arizona, Tucson, Arizona 85721, USA

Corresponding Author:

Jeong-Yeol Yoon, Department of Biomedical Engineering and Department of Agricultural and Biosystems Engineering, The University of Arizona, 1177 E. 4th St., Rm. 403, Tucson, AZ 85721-0038, USA. E-mail: jyyoon@email.arizona.edu.

Manuscript in preparation.

Abstract

The study of angiogenesis provides promise of therapeutic strategies for various disease development and inhibition. Conventional angiogenic models are unable to truly represent the dynamic process. Paper-based microfluidic cell culture systems may expedite development of angiogenic models, here referred to as angiogenesis-on-a-chip. Endothelial cells were cultured and optimized on collagen-coated nitrocellulose substrate. The endothelial cell response to biochemical cues, VEGF and S1P, was investigated on a paper-based angiogenesis-on-a-chip.

1. Introduction

Angiogenesis, the process of new vessel sprouting from existing vasculature, is a fundamental process involved in normal tissue development as well as disease progression. Its role ranges from embryonic development and wound healing, and its dysfunction can lead to ischemic and inflammatory diseases (Carmeliet, 2003; Folkman 1995). As a result, the inhibition, induction, or normalization of angiogenesis has been widely investigated as potential therapeutic strategies (Nguyen, et al., 2013).

There have been conventional models, employing polydimethyl siloxane (PDMS)-based and gel-based models, utilized to investigate the induction of angiogenesis, but remain inadequate due to the underwhelming *in vivo* representations. This failure is largely due to the dynamic nature and unpredictability of angiogenesis. Several studies demonstrated the growth of vascular endothelial cells on Matrigel (solubilized basement membrane matrix for improved cell attachment and differentiation) into multicellular cords that may partially resemble vascular networks. However, they lacked important features of native angiogenesis, such as directional invasion of cells into a 3D extracellular matrix (ECM) and fluid flow support (Stanton, et al., 2009, Donovan, et al., 2001). Moreover, the most well-investigated and approved chemical inducer of angiogenesis is vascular endothelial growth factor (VEGF), which modulates signaling pathways and control of angiogenesis (Nguyen, et al., 2013). In addition to the chemical growth factor, a mechanical induction by continuous flow similar to that *in vivo* is a crucial determining factor of endothelial cell behavior and sprouting (Stanton, et al., 2009, Kang, et al., 2008). Thus, researchers are seeking alternative approaches of 3D-based systems for angiogenic studies (Vickerman, et al., 2008).

Desirable 3D microenvironment and flow can be achieved with microfluidic systems, most notably organ-on-a-chip (OOC) technologies that can provide organ-mimic models. Key advantages of micro-scale cell culture systems include the use of low concentrations of cells and reagents, precise control of spatial and temporal environment, and potential cellular monitoring in real-time (Vickerman, et al., 2008). Unfortunately, conventional PDMS-based systems (the most common material used in fabricating microfluidic devices) are ill-suited as angiogenesis models, since the channel layout is pre-defined thus cannot provide necessary degree of freedom for random vessel sprouting. For example, PDMS-based models possess connecting microchannels that were pre-patterned network to make way for endothelial cell sprouting (Bischel, et al., 2013). However, this is an insufficient representation of the *in vivo* like environment, where vessels would sprout into uncontrollable directions. Fortunately, gel-based models do indeed better recapitulate the capillary network *in vivo* (Wang, et al., 2016). However, the production process is far too complex while requiring multiple steps, as well as, cannot easily be scaled-up for high-throughput screening applications (Wang, et al., 2016). Therefore, there is a crucial need for accessible fabrication of angiogenic models that can provide such an open layout enabling random sprouting of angiogenesis.

Recently, studies have demonstrated the use of paper-based microfluidic cell culture systems to investigate the cellular response to drugs (Tao, et al., 2015). Not only was the paper-based model non-cytotoxic, but the use of wax printing enabled fast and affordable fabrication (compared to PDMS-based soft lithography). Wax printing can provide hydrophilic regions for cell attachment and growth isolated by hydrophobic wax regions. Not to mention, the use of wax printing enables rapid prototyping of various interesting designs that is arduous to do so via

conventional lithography, which requires expertise, extensive time, costs, and access to capital equipment.

In this work, we investigated the validity of paper-based microfluidic culture for the study of angiogenesis. To the best of our knowledge, currently there are no published studies demonstrating angiogenesis on paper-based systems. Therefore, two simple objectives are explored herein: 1) can endothelial cells be cultured on paper-based systems; then 2) can angiogenesis be induced on paper-based systems? Various combinations of paper types and the coatings on paper were evaluated for optimum adhesion and growth of endothelial cells. Using the optimum combination, the channel layout was wax-printed on the paper substrate. To explore angiogenesis induction, endothelial cell response to biochemical cues, VEGF and sphingosine-1-phosphate (S1P), were explored. Although VEGF is generally a well-studied and accepted biochemical driver of angiogenesis, S1P is a signaling lipid that is also documented as a pro-angiogenic growth factor (Farahat, et al., 2012). The findings of this insightful study may inspire innovative strategies of paper-based angiogenesis-on-a-chip studies as a simple and straightforward method of studying angiogenesis.

2. Materials and Method

2.1 Papers and Coatings Tested

Multiple paper types and coatings were tested in this work. Paper types include cellulose chromatography paper (GE Healthcare, Maidstone, Kent, UK) and nitrocellulose (NC; EMD Millipore, Hayward, CA, USA). The coatings investigated include GRGDSPK (50 $\mu\text{g}/\text{mL}$; AnaSpec Inc., Fremont, CA, USA) and liquid type I rat tail collagen (50 $\mu\text{g}/\text{mL}$; BD, Franklin Lakes, NJ, USA). Positive substrates tested include both paper types coated with each coating

type: i.e. GRGDSPK-coated cellulose, collagen-coated cellulose, GRGDSPK-coated NC, and collagen-coated NC. Control substrate included paper types without coating, and standard tissue culture plate. Paper substrates were hole-punched into 0.5 cm² circles, individualized into a 96-well plate, and UV sterilized prior to proceeding.

Each paper substrate was incubated with each coating type for 1 h, then washed twice with phosphate buffer saline (PBS). Plate was sealed and stored in 4°C if not used immediately. For paper microfluidic chips, collagen-coated NC substrates were used to investigate angiogenic induction assays.

2.2 Paper Microfluidic Chip Fabrication

Paper microfluidic chips were fabricated using wax printer, illustrated in Figure F-1. Chips were designed using SolidWorks (Dassault Systemes, SolidWorks Corporation; Waltham, MA, USA) with each chip consisting of three parallel channels. The 30 mm x 11 mm chip included three channels (Figure F-1). The top channel and bottom channel are identical with a channel width of 3.5 mm. The center channel was 2 mm wide with two 0.5 mm wide breaks running along both its side, connecting to top and bottom channel.

Paper-based chip fabrication is illustrated in Figure F-1. Chip designs were printed with solid ink on NC paper (EMD Millipore) using a wax printer (ColorQube 8580, Xerox, Wilsonville, OR, USA). Individual chips were cut out and placed on a hot plate at 100°C for 2 minutes to melt the wax through the depth of the paper, while coating fibers evenly. Chips were sterilized with UV prior to storing in a sealed and dry conditions if not used immediately.

Type I rat tail collagen (50 µg/mL; BD) was deposited into all three channels to saturate the surface for 1 h. Channels were washed twice with PBS. Chips were sealed and stored at 4°C.

2.3 Cell Culture

Rat vascular endothelial cells (RVECs) were grown in Dulbecco's Modified Eagle Medium (DMEM) supplemented with 10% (v/v) fetal bovine serum (FBS; Fisher Scientific, Hampton, NH, USA), 50 $\mu\text{g}/\text{mL}$ gentamycin (Fisher Scientific), 100 $\mu\text{g}/\text{mL}$ kanamycin (Fisher Scientific), and 0.5 $\mu\text{g}/\text{mL}$ amphotericin B. Cells were cultured under static conditions at 37°C (HERAcell 150i; Cambridge Scientific; Watertown, MA, USA) in 5% CO₂. At 90% confluency, RVECs were resuspended in 10⁶ cells/mL concentration and seeded in the top and bottom channel of paper microfluidic chips (Figure F-2) for 10 min, prior to adding media and culturing for 24 h in static conditions. For paper and coating testing, 3.5 x 10⁴ cells/mL suspension of RVECs were cultured on each paper-coated substrate for 24 h in static conditions.

2.4 Induction of Biochemical Cues

After cell culture for 24 h under static conditions, chips were washed twice with DPBS. After DPBS was removed, cultures were treated with control (media alone), 100 ng/mL VEGF, or 500 ng/mL S1P for 24 h in static conditions.

2.5 Immunofluorescence Microscopy

Cells were washed twice with DPBS and fixed with 4% paraformaldehyde (Fisher Scientific) for 15 min. Cells were permeabilized with Triton X-100 (Fisher Scientific), then blocked with 1% bovine serum albumin (BSA) in PBS solution. Cells' nuclei were stained with DAPI, and actin filaments with TRITC-conjugated phalloidin (FAK100; EMD Millipore)

following their provided protocol (Millipore Inc. 2009). Samples were washed between steps with washing buffer (PBS containing 0.05% Tween 20).

3. Results and Discussion

Although paper is generally considered biocompatible, the objective at hand must be considered, and thus requires optimization. The use of paper-based systems undoubtedly have advantages in cell culture within the fibers to emulate a 3D microenvironment. However, for this case of angiogenesis, we are interested in culturing an endothelium monolayer on the surface of paper. Therefore, in regards to paper types, cellulose and nitrocellulose were considered due to their variances in pore size and molecular structure. With the objective of having smaller pore size to prevent cells from falling through the depths, nearly 10 μm (cellulose) versus less than 1 μm (NC) was investigated to optimize cell adhesion and proliferation. Surface treatment was also considered to enhance endothelial cell growth. The hydrophilic culture areas were treated with GRGDSPK peptide sequence, an attachment site proven to promote cell adhesion. Due to the affinity between positive charge of lysine (K) and negative charge (NC) or hydroxyl groups (cellulose), the resultant insolubilized peptide can promote efficient growth of an endothelial cell monolayer. As an alternative, collagen coating was considered to provide a ubiquitous layer over the hydrophilic paper fibers.

According to the results of paper type and coating type static assays (Supplementary Figure F-1), collagen-coated NC enabled significantly considerable cell growth as depicted by nuclei count. Consequently, paper angiogenesis-on-a-chip studies were proceeded with collagen-coated NC substrates. Interestingly, the autofluorescence of cellulose challenged the fluorescence

imaging of cells (Supplementary Figure F-1b), to the extent where greater magnification was recommended.

The endothelial cell culture on collagen-coated NC substrate did exhibit healthy and adherent behavior (Figure F-2). With lack of biochemical inducers, cells created a barrier in parallel with the wax break (Figure F-2). Therefore, cells were primarily contained within the top and bottom channels.

VEGF or S1P was later added to saturate the central channel that was originally lacking cells. With VEGF induction, endothelial cell sprouting was observed towards the center channel (Figure F-3) and in agreement with expected behavior from previous studies (Bischel, et al., 2013; Farahat, et al., 2012; Nguyen, et al., 2013). Although clear endothelial cell sprouting was not obvious with S1P induction, an arching of the cell front towards the center channel was visible (Figure F-3). In regards to S1P induction, the incubation time should be extended up to 3 days, similar to previously conducted studies (Farahat, et al., 2012; Nguyen, et al., 2013). Although cells were additionally stained with TRITC-conjugated phalloidin, the nonspecific binding of TRITC dye by wax severely limited the fluorescence imaging of actin filaments. Other colored fluorescent dyes should be explored as alternatives.

4. Conclusion

The study of angiogenesis has a broad impact due to its physiological and pathological importance. Unfortunately, the challenge of establishing a model system for the desirable study of angiogenesis has proven to be difficult. Although 3D cell culture systems show promise in capturing the dynamic growth of new blood vessels, the task itself requires great expertise, skills, and resources to execute, which is especially the case for high-quality microfabrication

techniques. The use of paper-based microfluidic angiogenesis model provides numerous benefits, such as cytocompatibility, direct contact with cells, and mechanical malleability. Future work of paper-based *in vitro* models, such as the one illustrated here, should concern establishing microfluidic flow control, which angiogenesis is generally considered a function of physiological mechanical stress (i.e. blood flow). Aside from the innate capillary action of the paper, one such promising concept of establishing self-driven flow exploits the siphon principle, where liquid travels from an upper to a lower level through the fibrous medium (Ozaki, et al., 2016). It is intended that the findings of this study provide preliminary evidence that supports the use of paper-based microfluidic systems for the study of not only angiogenesis, but any cell-based or organ-mimic modeling. The simple and rapid development of paper-based models may expedite the fabrication process towards actual meaningful and innovative discoveries.

5. References

- Bischel, L.L., Young, E.W.K., Mader, B.R., Beebe, D.J., “Tubeless microfluidic angiogenesis assay with three-dimensional endothelial-lined microvessels,” *Biomaterials*, 2013, 34(5): 1471-1477.
- Carmeliet, P., “Angiogenesis in health and disease,” *Nat Med*, 2003, 9(6): 653-660.
- Donovan, D., Brown, N.J., Bishop, E.T., Lewis, C.E., “Comparison of three in vitro human ‘angiogenesis’ assays with capillaries formed in vivo,” *Angiogenesis*, 2001, 4(2): 113-121.
- Farahat, W.A., Wood, L.B., Zervantonakis, I.K., Schor, A., Ong, S., Neal, D., Kamm, R.D., Asada, H.H., “Ensemble analysis of angiogenic growth in three-dimensional microfluidic cell cultures,” *PLoS ONE*, 2012, 7(5):e37333.
- Folkman, J., “Angiogenesis in cancer, vascular, rheumatoid and other disease,” *Nat Med*, 1995, 1(1): 27-31.
- Kang, H., Bayless, J.J., Kaunas, R., “Fluid shear stress modulates endothelial cell invasion into three-dimensional collagen matrices,” *Am J Physiol Heart Circ Physiol*, 2008, 295(5): H2087-H2097.
- Millipore Inc., “Actin cytoskeleton and focal adhesion staining kit,” 2009.
- Nguyen, D.-H.T., Stapleton, S.C., Yang, M.T., Cha, S.S., Choi, C.K., Galie, P.A., Chen, C.S., “Biomimetic model to reconstitute angiogenic sprouting morphogenesis in vitro,” *PNAS*, 2013, 110: 6712-6717.
- Ozaki, A., Arisaka, Y., Takeda, N., “Self-driven perfusion culture system using a paper-based double-layered scaffold,” *Biofabrication*, 2016, 8: 035010.

- Stanton, C.A., Reed, M.W., Brown, N.J., “A critical analysis of current in vitro and in vivo angiogenesis assays,” *Int J Exp Pathol*, 2009, 90(3): 195-221.
- Tao, F.F., Xiao, X., Lei, K.F., Lee, I.-C., “Paper-based cell culture microfluidic system,” *BioChip J*, 2015, 9(2): 97-104.
- Wang, X., Phan, D.T.T., Sobrino, A., George, S.C., Hughes, C.C.W., Lee, A.P., “Engineering anastomosis between living capillary networks and endothelial cell-lined microfluidic channels,” *Lab Chip*, 2016, 16: 282-290.
- Vickerman, V., Blundo, J., Chung, S., Kamm, R., “Design, fabrication and implementation of a novel multi-parameter control microfluidic platform for three-dimensional cell culture and real-time imaging,” *Lab Chip*, 2008, 8: 14681477.

6. Figures

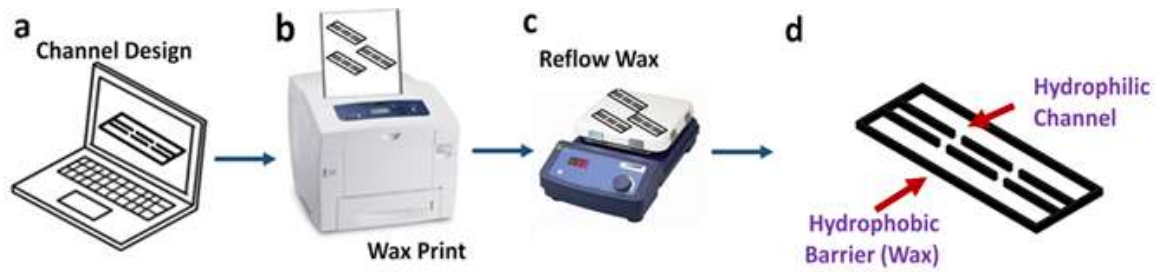


Figure F - 1

Paper microfluidic chip fabrication. (a) CAD model design of microfluidic chip is created. Multiple chips were wax printed (b), and placed on a hot plate (c) to enable wax to reflow and evenly coat fibers. (d) Hydrophilic channels are bound by hydrophobic wax.

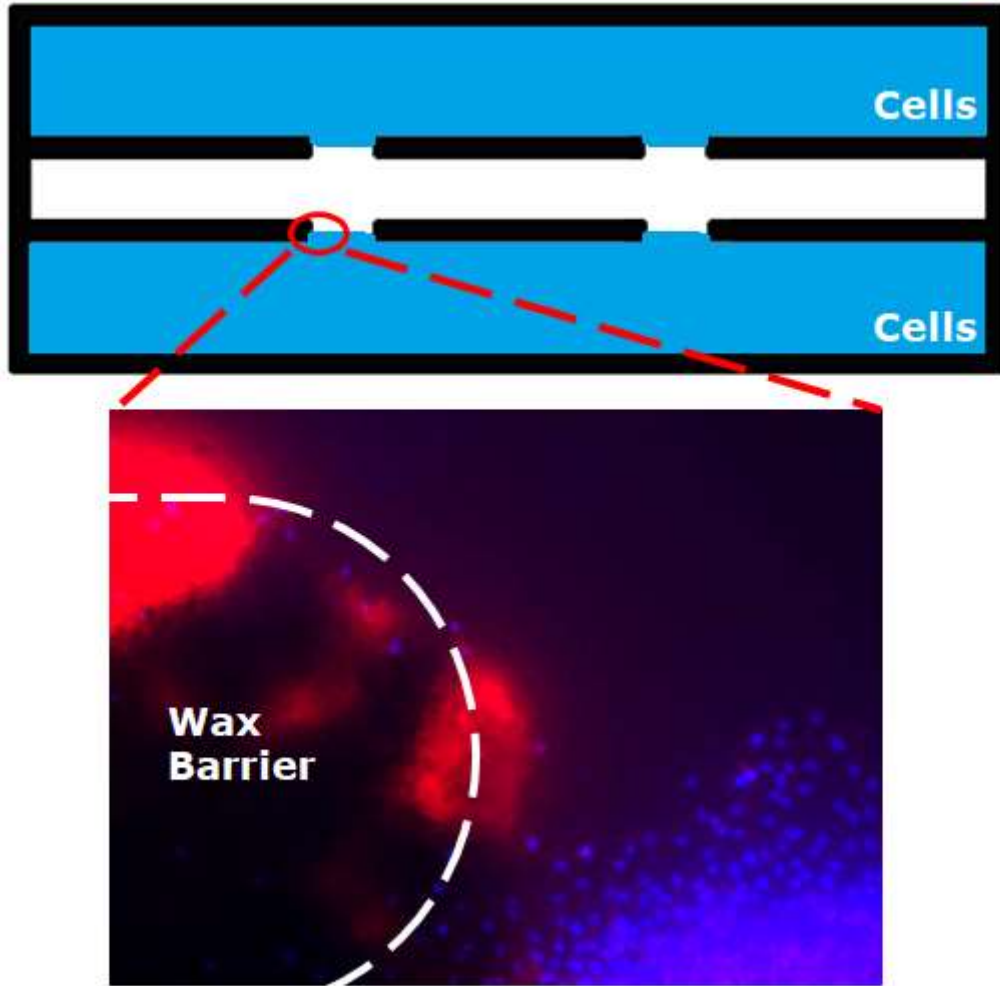


Figure F - 2

Endothelial cells after 24 h incubation on paper chip. Inset image shows 4X magnification of circled area, where wax barrier breaks thus connecting central and bottom channel. Blue depicts DAPI for nuclei of cells. Red illustrates the non-specific binding of wax to TRITC-conjugated phalloidin.

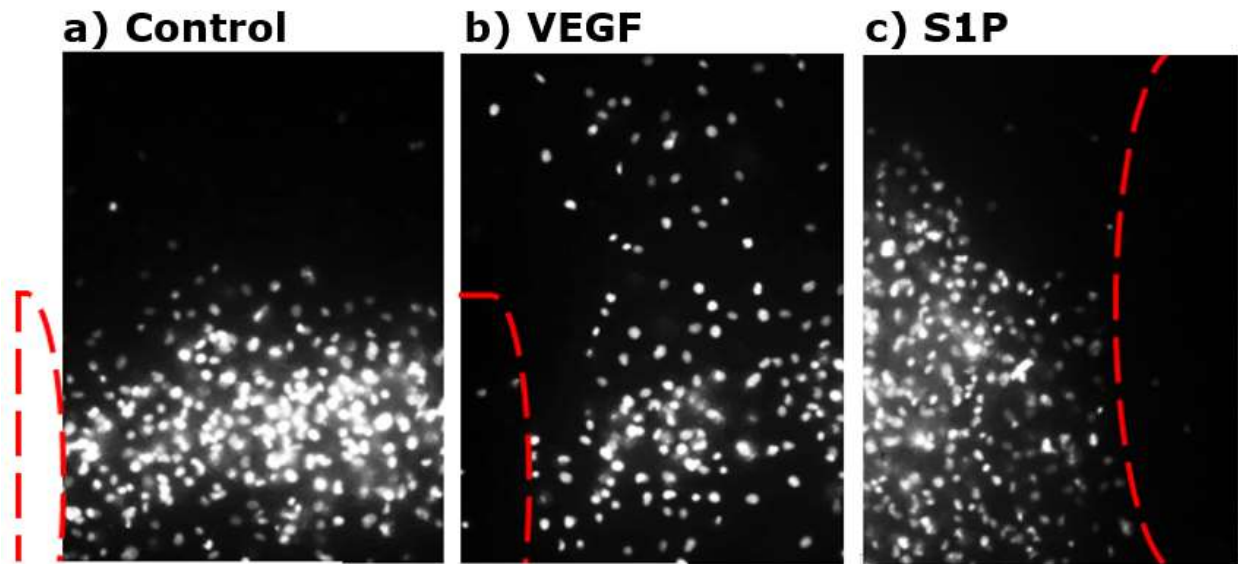
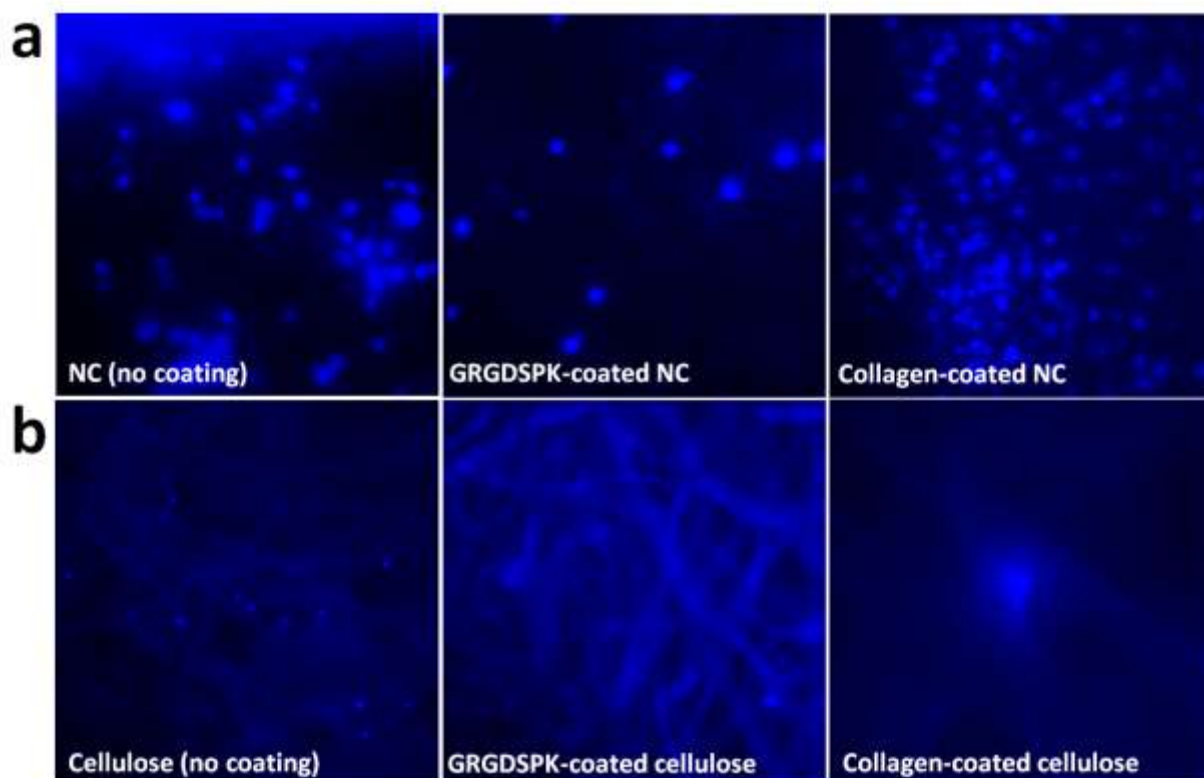


Figure F - 3

10X fluorescent images of DAPI-stained cells on paper microfluidic chip after 24 h static incubation with control (a), VEGF (b), and S1P (c) at breaks between wax barriers. Red dashed lines depict borders of wax barrier of channel design.



Supplementary Figure F - 1

Investigation of cell culture on paper and coating type combinations post-24 h culture. 10X fluorescent images of DAPI-stained cells on NC (a) with no coating, GRGDSPK-coating, and collagen-coating; and on cellulose (b) with no coating and GRGDSPK-coating. Cellulose substrates exhibited obvious autofluorescence, which called for greater magnification to observe cells, as shown in collagen-coated cellulose image at 40X magnification.